NUREG/CR-3900
Vol. 2

Long-Term Performance of Materials Used for High-Level Waste Packaging

Second Quarterly Report, Year Three
July - September 1984

Compiled by D. Stahl, N. E. Miller

Battelle's Columbus Laboratories

Prepared for
U.S. Nuclear Regulatory
Commission

NOTICE

This report was prepared as an account of work sponsored by an agency of the United States Government. Neither the United States Government nor any agency thereof, or any of their employees, makes any warranty, expressed or implied, or assumes any legal liability or responsibility for any third party's use, or the results of such use, of any information, apparatus, product or process disclosed in this report, or represents that its use by such third party would not infringe privately owned rights.

NOTICE

Availability of Reference Materials Cited in NRC Publications

Most documents cited in NRC publications will be available from one of the following sources:

1. The NRC Public Document Room, 1717 H Street, N.W.
   Washington, DC 20555
2. The NRC/GPO Sales Program, U.S. Nuclear Regulatory Commission,
   Washington, DC 20555
3. The National Technical Information Service, Springfield, VA 22161

Although the listing that follows represents the majority of documents cited in NRC publications, it is not intended to be exhaustive.

Referenced documents available for inspection and copying for a fee from the NRC Public Document Room include NRC correspondence and internal NRC memoranda; NRC Office of Inspection and Enforcement bulletins, circulars, information notices, inspection and investigation notices; Licensee Event Reports; vendor reports and correspondence; Commission papers; and applicant and licensee documents and correspondence.

The following documents in the NUREG series are available for purchase from the NRC/GPO Sales Program: formal NRC staff and contractor reports, NRC-sponsored conference proceedings, and NRC booklets and brochures. Also available are Regulatory Guides, NRC regulations in the *Code of Federal Regulations*, and *Nuclear Regulatory Commission Issuances.*

Documents available from the National Technical Information Service include NUREG series reports and technical reports prepared by other federal agencies and reports prepared by the Atomic Energy Commission, forerunner agency to the Nuclear Regulatory Commission.

Documents available from public and special technical libraries include all open literature items, such as books, journal and periodical articles, and transactions. *Federal Register* notices, federal and state legislation, and congressional reports can usually be obtained from these libraries.

Documents such as theses, dissertations, foreign reports and translations, and non-NRC conference proceedings are available for purchase from the organization sponsoring the publication cited.

Single copies of NRC draft reports are available free, to the extent of supply, upon written request to the Division of Technical Information and Document Control, U.S. Nuclear Regulatory Commission, Washington, DC 20555.

Copies of industry codes and standards used in a substantive manner in the NRC regulatory process are maintained at the NRC Library, 7920 Norfolk Avenue, Bethesda, Maryland, and are available there for reference use by the public. Codes and standards are usually copyrighted and may be purchased from the originating organization or, if they are American National Standards, from the American National Standards Institute, 1430 Broadway, New York, NY 10018.

GPO Printed copy price: $5.00

NUREG/CR-3900
Vol. 2

Long-Term Performance of Materials Used for High-Level Waste Packaging

Second Quarterly Report, Year Three
July - September 1984

Manuscript Completed: November 1984
Date Published: January 1985

Compiled by
D. Stahl, N. E. Miller

Battelle's Columbus Laboratories
505 King Avenue
Columbus, OH 43201-2693

Prepared for
Division of Radiation Programs and Earth Sciences
Office of Nuclear Regulatory Research
U.S. Nuclear Regulatory Commission
Washington, D.C. 20555
NRC FIN B6764
Under Contract No. NRC 04-82-015

CONTRIBUTORS

J. A. Beavers
H. J. Cialone
M. P. Failey
J. H. Holbrook
A. J. Markworth
J. K. McCoy
S. L. Nicolosi
M. R. Pascucci
E. D. Spinosa
N. G. Thompson

ABSTRACT

As part of the Nuclear Regulatory Commission's requirement to assess the Department of Energy's application to construct geologic repositories for storing high-level radioactive waste, Battelle's Columbus Laboratories is investigating the long-term performance of materials used for high-level waste packaging. During this reporting period, it was found that glass-water contact during the nonisothermal periods of leach testing may influence the test results. Modeling of waste-form degradation focused on dissolution/reprecipitation kinetics. An experiment is planned to verify this model. A procedure was developed to disperse RuO_2 in MCC 76-68 glass. Potentiodynamic polarization tests were performed to determine the effects of single chemical species in groundwater on the cracking and pitting susceptibility of carbon steel. Slow strain rate tests show that carbon steel is especially susceptible to stress-corrosion cracking in aqueous $FeCl_3$ at low strain rates. The strength of commercial high-purity iron was found not to be affected by hydrogen; however, ductility was somewhat reduced. The description of groundwater radiolysis was further refined during this quarter. Integral experiments are being prepared to provide information on combined-effects processes that may influence the long-term performance of the waste package.

This report documents investigations performed during the period July-September 1984.

TABLE OF CONTENTS

TABLE OF CONTENTS
(Continued)

LIST OF FIGURES

LIST OF FIGURES

(Continued)

LIST OF FIGURES

(Continued)

LIST OF FIGURES

(Continued)

LIST OF TABLES

LIST OF TABLES

(Continued)

PREVIOUS REPORTS IN SERIES

NUREG/CR-3405, Volume 1: "Long-Term Performance of Materials Used for High-Level Waste Packaging: Annual Report, March 1982-April 1983."

NUREG/CR-3427, Volume 1: "Long-Term Performance of Materials Used for High-Level Waste Packaging: Quarterly Report, April-June 1983."

NUREG/CR-3427, Volume 2: "Long-Term Performance of Materials Used for High-Level Waste Packaging: Quarterly Report, July-September 1983."

NUREG/CR-3427, Volume 3: "Long-Term Performance of Materials Used for High-Level Waste Packaging: Quarterly Report, October-December 1983."

NUREG/CR-3427, Volume 4: "Long-Term Performance of Materials Used for High-Level Waste Packaging: Annual Report, April 1983-April 1984."

NUREG/CR-3900, Volume 1: "Long-Term Performance of Materials Used for High-Level Waste Packaging: Quarterly Report, April-June 1984".

1. INTRODUCTION: PROJECT OBJECTIVES AND APPROACH

The Waste Policy Act of 1982 delegates to the Department of Energy (DOE) the authority for siting, construction, and operation of deep-mined geologic repositories for the disposal of high-level waste and spent fuel. The Nuclear Regulatory Commission (NRC) has the responsibility to regulate the activities of DOE to assure that the health and safety of the repository workers and of the public are adequately protected. Prior to construction, the DOE will submit a license application to the NRC describing in detail the proposed repository. The DOE has been directed to take a multiple barrier approach to the isolation of radioactive wastes with the waste package, the engineered facility, and the natural geohydrologic features of the site being the major barriers. Since NRC's compliance assessment requires the technical capability to understand relevant phenomena and processes relating to the long-term performance of the multiple barriers, the NRC's Office of Nuclear Regulatory Research (RES) has established this waste-package performance program at Battelle's Columbus Laboratories to provide that part of the input to the assessment. As an important aid to this understanding, Battelle is evaluating total system performance which will integrate separate effects and improve the understanding of the long-term performance of waste-package materials. This will also assist in identifying and evaluating research needs.

It is generally accepted that after repository closure the dominant mechanism to cause the release of radionuclides from the repository is groundwater transport. The generally accepted approach to minimizing the release is to provide a number of different barriers to the dissolution and transport of radionuclides by the groundwater. For a deep-mined repository, the geohydrologic features of the earth itself are expected to be a major barrier to the release of radionuclides. The repository site will be selected so that radionuclides will be isolated for very long times. In addition, engineered features of the repository will act as a barrier to the release of radionuclides. The repository will be constructed so as to minimize disturbing the adjacent rock and to accommodate the thermomechanical effects of the emplaced wastes with a minimum of degradation to its geohydrologic properties. Upon closure, the underground openings and shafts to the surface will be backfilled and sealed to minimize groundwater flow paths.

The waste package--which is the center of this study--will be constructed to provide essentially complete containment of the radionuclides through the period of time in which the repository is heated significantly by decaying fission products. After the container is eventually breached by some process, the waste form must remain sufficiently resistant to groundwater attack to provide high retention of the radionuclides and, together with the repository, to control the release of radionuclides for thousands of years. The objective of our research is to provide an improved understanding of the long-term performance of the materials used for the high-level waste package. More specifically, we are identifying those processes that tend to degrade the performance of the waste-package materials, performing experiments to produce data where data are otherwise lacking on material performance, and analytically modeling the processes to utilize the data to better understand how the processes will affect the material's future performance. In addition, we are identifying areas of work that should be performed by DOE to provide missing data which are beyond the resources of the NRC.

1.1 Individual Program Tasks

The program is being conducted in three parallel efforts: waste-form studies, container studies, and integrated system performance studies. A more detailed summary of achievements can be found in the second annual report for this program (NUREG/CR-3427, Volume 4, June 1984, Section 1).

1.1.1 Waste Forms

The waste-form studies are aimed at first describing and modeling those mechanisms that will alter or "age" the waste form during the containment period, and second, identifying and describing those processes that will influence waste-form dissolution after it is exposed to groundwater. The waste-form studies have been largely centered on borosilicate glasses for both defense and commercial high-level wastes; some effort has also been directed toward evaluating spent fuel as a waste form.

In borosilicate glasses, the glass-forming agents can be expected to be tailored to optimize the waste-form properties for each type of high-level waste. After the waste forms are produced, particularly during the very long period of time after disposal while sealed in their containers, they will experience processes that will cause changes. One detrimental effect is devitrification of the glass, which can lead both to new phases with increased solubility and to cracking of the glass (which is detrimental because it allows a greater surface area of the glass to be contacted by the groundwater). A model has been developed to predict the degree of devitrification that will occur from subsequent reheating in the repository after disposal. Another detrimental effect is cracking, which could be induced by the effects of radiation on glass. A study of the radiation effects on glass has revealed no new approach to evaluating this phenomenon experimentally, so we are largely dependent on the existing literature which indicates that radiation produces only a small effect on glass performance.

1.1.2 Container Materials

The container studies focus on processes that can degrade the metallic waste-package container. The objective is to collect data on the parameters that influence the degradation processes, to identify the controlling parameters, and ultimately to model the degradation processes that determine the long-term performance of the container. The material under study is cast low-carbon steel for use in a basalt repository, which is the material currently favored by DOE.

The dominant degradation processes that affect the outside of the container are general corrosion, stress-corrosion cracking, pitting, crevice corrosion, hydrogen attack, and mechanical stress. These processes may occur individually or in combination. The parameters that affect these processes include chemical composition and physical state of the steel, groundwater composition and flow rate, temperature, radiation intensity, availability of air, lithostatic forces, redox state, alkalinity/acidity, and availability of hydrogen. These can produce general corrosion, in which the rate of general corrosion will determine the necessary wall thickness, or localized corrosion (such as pitting or crevice corrosion), in which the rate of the localized attack and the container life must be used to establish the wall thickness.

If the steel is susceptible to cracking in the expected environment, the rate of cracking is so rapid relative to required container life that the corrosion-allowance approach cannot be used to achieve acceptable performance. What is important is the susceptibility of the metal to crack initiation. Cracking may result from stress-corrosion cracking or from reduction in fracture toughness from hydrogen attack. Both of these processes are under investigation.

In addition, a comprehensive mathematical model is under development for use in understanding the corrosion processes associated with the waste-container materials in a repository environment. The model computes the fluxes of corrosive species to the container surface, taking into account the fact that certain corrosive species may be generated by radiolysis, and also accounts for diffusion and convective flow to transport the species. The modeling effort is also being applied to pitting attack and considers three different aspects of the overall pitting process: pit-initiation kinetics, pit-growth kinetics, and the evolution of the pit-depth distribution. These analytical efforts are well integrated with the experimental efforts and are being directed to providing an understanding of the long-term performance of the container materials, with emphasis on those processes that can lead to poor performance.

1.1.3 Integrated System Performance

The waste-package system studies interact with the waste-form studies and the container-material studies to provide an improved understanding of the performance of the total waste-package system. The current emphasis is on providing information for a better understanding of the processes involved in waste-package system degradation. One aspect of the total system under study is the production of radiolysis products in the groundwater by gamma radiation from the waste. This is of major importance in modeling the corrosion of the container and in planning experiments to determine the effects of radiolysis. Our radiolysis model is based on existing codes and sets of chemical reactions combined to provide the best description of experimental data found in the literature. The output of the radiolysis model calculations provides input to the water-chemistry model, which is a fundamental part of the glass-dissolution model and the general-corrosion model.

The water-chemistry model which we initially developed for our use with our glass-dissolution and corrosion models has intentionally been kept simple. Simplifying assumptions were made and only a limited set of chemical species was used. This set included the basic water species, the species which dominate most natural groundwaters, and certain species which are assumed to result from the corrosion of iron-based metallic containers and from the dissolution of borosilicate glass. Additional species are being incorporated as the model matures. Inputs to the model include temperature, oxidation potential, volume of water, and amounts of each of the elements in solution (including those species from the radiolysis code). The water-chemistry model calculates the concentration and activity of each of the water species.

1.2 Overall Program Objectives

In all the program tasks, the ultimate objective is to develop a base of information to assist the NRC in evaluating the performance of the waste package proposed in DOE's license application. A near-term objective is to provide information to allow the NRC to prepare position papers on the information required of DOE for evaluation of DOE's proposed waste package. Of significance here is identifying sensitive parameters affecting the performance of materials and identifying data requirements.

To achieve the above objectives, the waste-form task is providing information to give a better understanding of the release of radionuclides from the waste form, beginning at the time it is first contacted by groundwater through the 10,000-year period defined in the draft EPA Standard. This includes an understanding of the probable physiochemical condition of the waste form when it is contacted by groundwater, as well as the parameters of waste-form composition and environmental conditions which will cause changes from its state at the time of disposal. In addition, we are producing experimental data on the parameters that affect dissolution of the waste form, including composition of the groundwater and environmental conditions. The waste-form dissolution process is also being mathematically modeled to allow analysis of the performance of the waste form under specific input conditions.

The information on the performance of the container materials relates to the required containment period of up to 300 to 1000 years. The container performance is expected to be most affected by corrosion and hydrogen-attack processes. We are providing information on the parameters of container-material composition, groundwater composition, and environmental conditions that are most significant in these processes. Our studies of cast low-carbon steel in a basalt environment (the container material currently favored by DOE) focus on the susceptibility of the metal to stress-corrosion cracking under repository conditions, because steel is known to fail by this process in some environments. We are studying the chemical species and environmental conditions that cause cracking to determine whether this mode of failure is expected under credible repository conditions. Our experimental studies on general and localized corrosion, together with our comprehensive general-corrosion model, will assist in evaluating the corrosion-allowance approach for the use of steel as a long-life container.

Modeling efforts in the integrated system performance task are contributing significant information to studies of general corrosion and glass dissolution. These studies require knowledge of the amount and kind of chemical species that may be produced by radiolysis of the groundwater near the waste package as a result of gamma radiation from the enclosed waste. To obtain this information, energy deposition and radiolysis codes are used. The ANISN code is used to calculate the gamma fluxes and energy-deposition rates in and near the waste package over the time after disposal; these have been calculated for commercial high-level waste and for spent-fuel waste forms. The gamma fluxes and energy-deposition rates as a function of time are then used in the water-radiolysis model to calculate the amount and kind of radiolysis products in the groundwater near the waste package. To determine how these radiolysis products may affect the performance of the canister and waste form, it is necessary to determine their chemical activities. These are calculated by the water-chemistry model. The output from the water-chemistry model is the concentration and activity of each chemical species in the groundwater near the waste package. This information is used not only as input to the general-corrosion and glass-dissolution models, but also as a point of reference in directing the experimental efforts in corrosion and dissolution.

2. WASTE FORMS

A leaching experiment was completed to evaluate glass-water contact and separation during nonisothermal periods. Efforts in modeling waste-form degradation continued, focusing on the kinetics of glass dissolution/reprecipitation. An experimental plan to verify the dissolution/reprecipitation model was developed during this quarter. Experiments aimed at dispersing a melt-insoluble nucleating agent, RuO_2, in MCC 76-68 glass were conducted during the quarter. A plan was developed to relate the large data base that exists for MCC 76-68 and similar glasses to some effects potentially present in the integral experiments described in Section 4.3.

2.1 Glass-Water Contact Experiment

The objective of this experiment is to assess the uncertainty associated with glass-leaching data that results from an analytical difficulty inherent to static waste-form leaching experiments. The potential problem is reprecipitation of chemical constituents upon the glass specimen during cooling at the end of the experiment. The MCC-1P and MCC-2P procedures used by most experimenters in this field require that the reaction vessels be cooled to room temperature prior to withdrawing solution and glass specimens for analysis. With these and similar procedures, waste-form constituents whose solubilities are temperature-dependent and that are in solution at elevated temperature may nucleate and precipitate upon the glass specimen during cooling, thereby changing the solution composition and the glass-surface properties from those at the test condition.

2.1.1 Procedure

The experiments were carried out for 28 days at 90 and 190 C in 125-ml digestion bombs with TEFLON* liners. The experimental matrix includes tests with slow cooling with leachate and glass in continuous contact, and cooling with leachate and glass separated, as illustrated in Figure 2.1. Except for the separation of the glass specimen and simulated Grande Ronde basalt water during heating and cooling, MCC-1P and MCC-2P procedures were followed. Experiments were run in triplicate or quadruplicate, with blanks run at each temperature. Two separate ovens were used so that the entire matrix of experiments, shown in Table 2.1, could be conducted simultaneously.

---

*TEFLON is a registered trademark of the E.I. DuPont de Nemours Company.

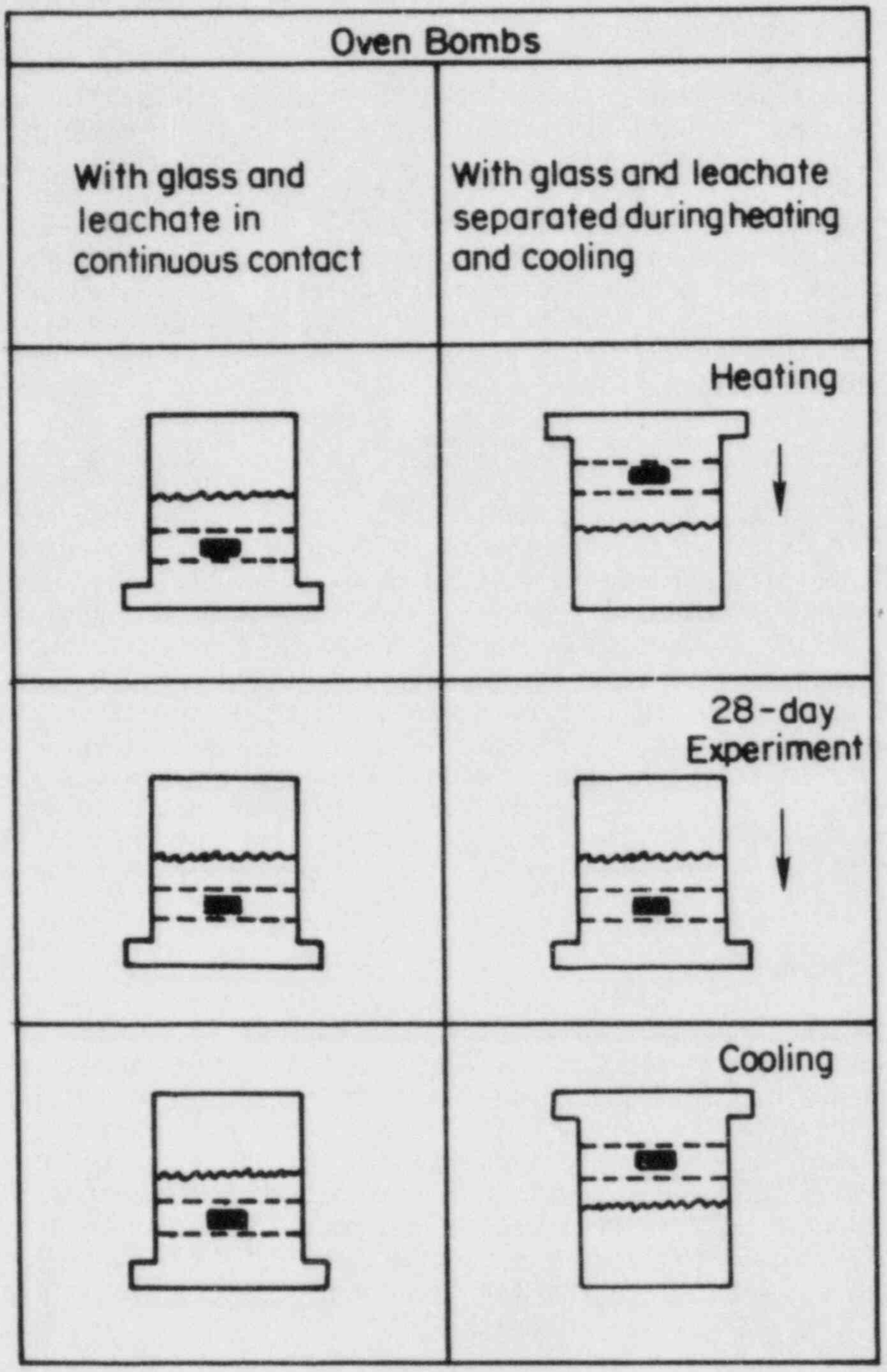

Figure 2.1. Schematic representation of method used to isolate glass sample from leachate.

Table 2.1. Glass-water-contact experimental matrix.

Sampling Method	Temperature, C 90	 190
Leachate and glass isolated during heating and cooling	XXX	XXXX
Leachate and glass in continuous contact during cooling	XXX	XXXX
Blank (no glass specimen)	XXX	XXX

X represents a single digestion bomb.

Leachate: synthetic basalt groundwater(2.1)

Glass: MCC 76-68

Ratio of surface-area to volume: 0.1/mm

Pressure: autogenous

Low Eh maintained by argon atmosphere.

The experimental responses measured at the conclusion of the experiments included: (a) leachate-solution compositions, measured by inductively-coupled argon plasma (ICAP) analysis for selected glass constituents after leachate digestion; (b) the mass of the leached glass specimens; (c) the final solution pH; (d) the surface characteristics of the leached glass specimens, determined by analytical procedures such as scanning electron microscopy-energy dispersive x-ray analysis (SEM-EDAX) and electron spectroscopy for chemical analysis (ESCA). The data from the leachate compositions and glass-specimen masses will demonstrate whether precipitation upon glass samples is important in determining quantitative leach rates. The information obtained from the detailed surface analyses indicates the nature and extent of the precipitates and allows us to distinguish clearly between the alteration layer that forms during exposure and the precipitates that form during cooling. Results of these experiments may indicate that some data from the commonly-used tests require special interpretation.

2.1.2 Results

Data on the percent change in weight and the change in pH taken as the difference between initial and final values are shown in Table 2.2. To evaluate the presence of statistically significant differences between continuous-contact samples and samples exposed to leaching only at the experimental temperature, standard analyses of variance (ANOVAs) were performed on these data. The 90 C and 190 C data were analyzed separately because different variances were expected to be induced by more aggressive attack at 190 C. A summary of these ANOVAs is presented in Table 2.3.

The ANOVA for the weight-change data at 90 C indicates that no effect is present. However, a very definite pH-change effect occurs at that temperature. At 190 C, both the weight loss and the pH change show statistically significant influence of continuous and noncontinuous contact. In this case, the weight loss is slightly more significant than the pH change.

Selected scanning electron micrographs of glass-specimen surfaces are shown in Figures 2.2 and 2.3. Figure 2.2a illustrates an unleached glass sample at 500X, showing the 600 grit grinding striations on the surface. Surfaces of glass samples leached at 90 C are illustrated in Figures 2.2b and 2.2c The "honeycomb" structure apparent in both apparently results from leaching of more soluble glass constituents, leaving the less soluble constituents behind. The glass sample in continuous contact with the leachate during cooling (Figure 2.2c) is morphologically very similar to the glass sample isolated from the leachate during cooling (Figure 2.2b), suggesting no precipitation of solutes during cooling from 90 C.

The surfaces of glass samples leached at 190 C, illustrated in Figure 2.3, show very different morphological characteristics. The glass cooled in isolation from the leachate (Figure 2.3a) exhibits a

Table 2.2. Summary of results of glass-water contact experiments.

		Temperature, C	
		90	190
Continuous Contact	Percent weight change	-0.083	-1.182
		-0.054	-1.135
		-0.073	-1.139
			-1.108
	average	-0.070	-1.141
			0.105
	ΔpH	0.160	0.251
		0.135	0.115
		0.115	0.160
	average	0.137	0.158
Contact only at experimental temperature	Percent weight change	-0.083	-1.167
		-0.079	-1.199
		-0.079	-1.334
			-1.204
	average	-0.080	-1.226
		0.260	0.235
	ΔpH	0.180	0.210
		0.335	0.360
			0.205
	average	0.258	0.252

Table 2.3. Analysis of variance (ANOVA) summaries for glass-water contact experiment.

	Temperature, C	Calculated F-Statistic	Probability of No Effect
Percent weight change	90	1.441	29.7%
	190	4.552	7.6%
ΔpH	90	6.815	5.9%
	190	3.685	10.2%

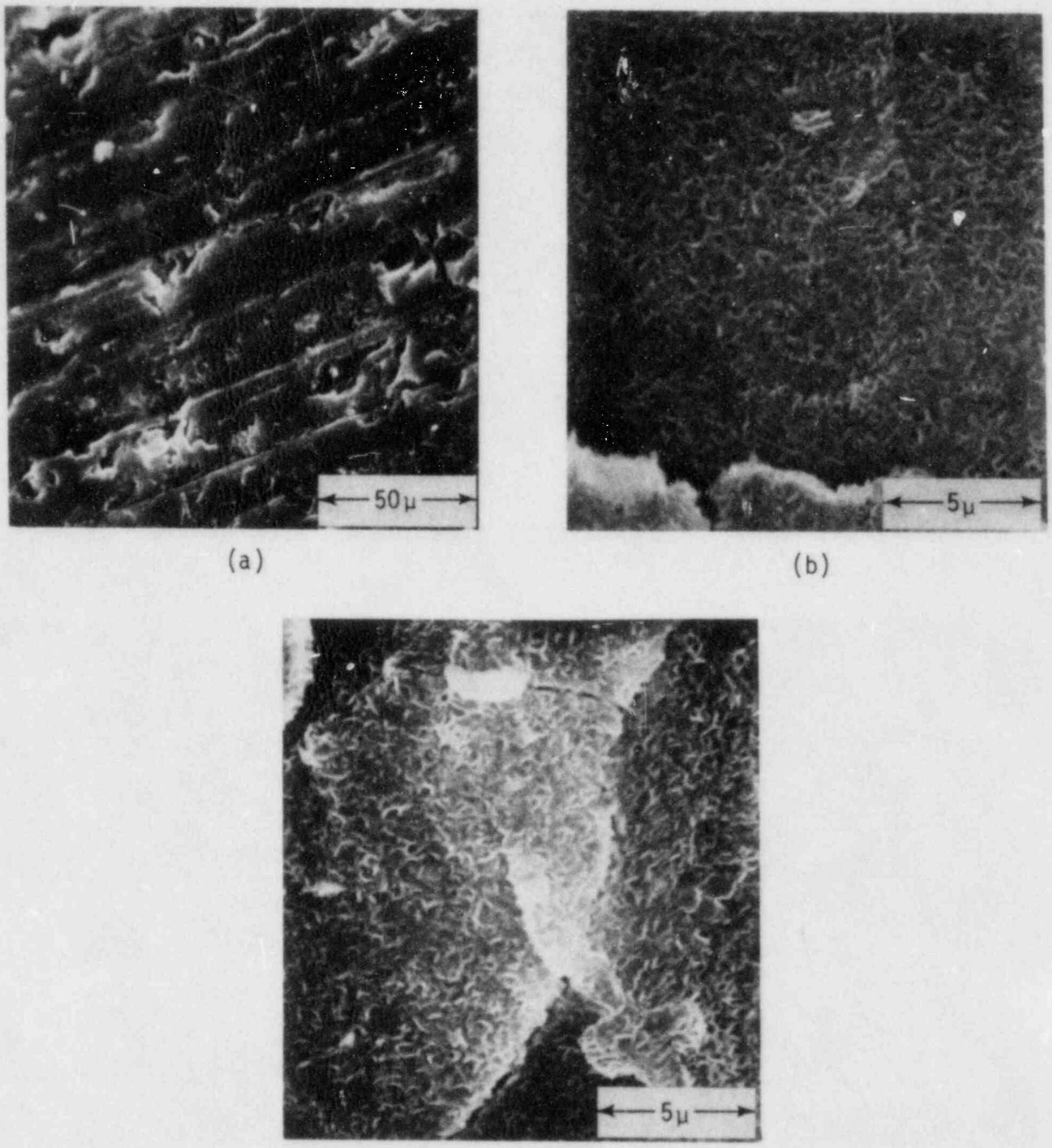

(a)

(b)

(c)

Figure 2.2. Scanning electron micrograph of: (a) unleached glass; (b) glass leached at 90 C and isolated from leachate during cooling; and, (c) glass leached at 90 C and cooled in continuous contact with leachate.

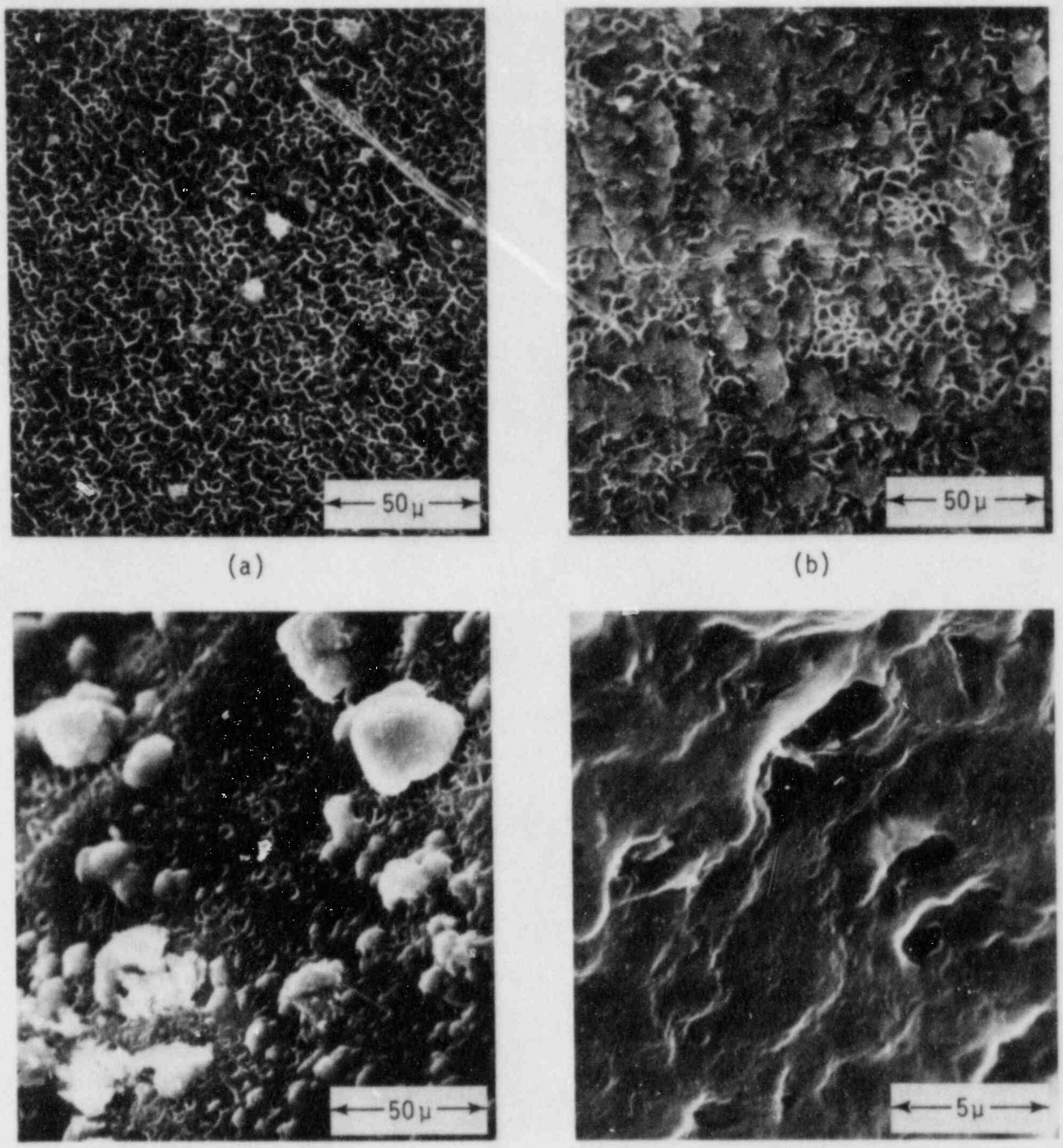

(a) (b)

(c) (d)

Figure 2.3. Scanning electron micrographs of: (a) glass leached at 190 C and isolated from leachate during cooling; and (b), (c), and (d) glass leached at 190 C and cooled in continuous contact with leachate.

"honeycomb" structure similar to those in Figures 2.2b and 2.2c, except that the leached layer appears to be deeper, a result consistent with greater dissolution at the higher temperature. However, glass samples allowed to remain in contact with the leachate during cooling from 190 C (Figure 2.3b-d) show distinct precipitates on the outer surface of the honeycomb structures. These precipitates apparently formed predominantly during cooling from 190 C to room temperature by the deposition of chemical constituents which were soluble at 190 C but, being insoluble at lower temperature, nucleated onto the glass surface. Figure 2.3b shows nodule-like precipitates covering about 50 percent of the glass surface-area. In Figure 2.3c, the honeycomb layer is almost completely covered by a thin film, and large nodules were deposited onto the film. Figure 2.3d shows the film in greater magnification, with traces of the honeycomb structure showing through.

Leached glass samples were analyzed by energy-dispersive x-ray analysis (EDAX) and electron spectroscopy for chemical analysis (ESCA). Selected EDAX analyses are reported in Table 2.4. The values are normalized to 100 percent for the five elements listed. Their actual concentrations are lower because other elements are present but are either not detected by EDAX (e.g., oxygen) or were detected in trace or irregular concentrations (e.g., titanium and magnesium). The data discussed in the text are underlined.

Consistent with the SEM data, the EDAX analyses show no significant compositional differences between glasses in continuous contact or isolated from leachates during cooling in the 90 C experiments. Areal scan data on specimens at 190 C show that glasses in continuous contact with leachates are enriched in iron and zinc. Data taken on selected nodules indicate calcium and phosphorus enrichment of glasses in continuous contact with the leachate. All four elements are MCC 76-68 glass constituents, and calcium is also present in the synthetic groundwater. This enrichment is interpreted to be indicative of precipitation of these elements onto the alteration layers during cooling. The zinc and iron are likely to be precipitating as oxides, and the calcium and phosphorus appear to be forming a $Ca \cdot PO_4$ species. Note, however, that the 190 C glasses isolated from the leachate are somewhat enriched in zinc (scan acquisition) and calcium and phosphorus (spot acquisition) relative to unleached controls and glasses leached at 90 C. One interpretation of these observations is that zinc, calcium, and phosphorus concentrate in the alteration layer during the 28-day experiment, and then iron, zinc, calcium, and phosphorus further nucleate and precipitate upon the glass sample during cooling.

ESCA data show similar compositional trends and are reported in Table 2.5. These data include oxygen and do not necessarily add up to 100 percent because several trace elements of little importance, such as nickel and titanium, are not reported. Again, the more significant compositional differences are between samples isolated and in continuous contact with leachates at 190 C. Calcium, phosphorus, and zinc appear

Table 2.4. Chemical compositions of glass surface layers determined by energy-dispersive x-ray analysis.

	Weight Percent(a)				
Glass Sample	Si	P	Ca	Fe	Zn
Scan Acquisition Unexposed MCC 76-68	54.6	5.4	6.5	19.6	13.9
Scan Acquisition 90 C Isolated	36.3	5.0	9.5	27.5	21.7
Scan Acquisition 90 C Continuous Contact	35.4	--	9.3	30.8	24.6
Scan Acquisition 190 C Isolated	47.7	--	7.8	18.0	27.2
Scan Acquisition 190 C Continuous Contact	23.6	--	5.3	29.3	41.7
Spot Acquisition 190 C Isolated	38.6	9.4(b)	12.7	12.3	27.0
Spot Acquisition 190 C Continuous Contact	25.3	22.0	27.2	9.4	16.1

(a) Normalized to 100 percent.

(b) Underlined data are discussed in the text.

to precipitate in the alteration layer during the cooling phase at the conclusion of the experiment. However, these elements are already slightly enriched on glass surfaces that were isolated from leachate during cooling. Binding-energy data from ESCA analysis indicate that iron and zinc are present as oxides and calcium and phosphorus are present as a $Ca \cdot PO_4$ species.

Table 2.5. Chemical compositions of glass surface layers (0-30 Å) determined by electron spectroscopy for chemical analysis.

	Weight Percent					
Glass Sample	Si	P	Ca	Fe	Zn	O
Unleached Control	20.4	--	2.3	2.9	1.5	67.7
90 C, Isolated	13.0	--	--	3.6	0.2	82.0
90 C, Continuous Contact	17.5	--	2.0	2.6	2.2	75.5
190 C, Isolated	17.1	1.7*	2.7	2.7	4.5	67.8
190 C, Continuous Contact	14.9	2.7	3.7	2.1	6.5	69.1

*Underlined data are discussed in the text.

In summary, the films and nodules, shown in Figures 2.3b-d, that coat the leached honeycomb structure shown in Figure 2.3a are composed primarily of iron and zinc oxides and a $Ca \cdot PO_4$ species. They appear to be an artifact produced when the leachate is in contact with the glass specimens during cooling from 190 C. These elements are also enriched in the alteration layer during the 28-day 190 C experiments, and their presence facilitates further nucleation and precipitation during cooling.

2.1.3 Conclusions

SEM analyses (Figures 2.2 and 2.3) show definite reprecipitation during cooling in the 190 C experiments when the glass specimen and the leachate are cooled in continuous contact. Such reprecipitates are experimental artifacts that form during cooling to room temperature after the experiment has been concluded. Statistical analyses of weight loss and pH change indicate that these effects are real, but small. They are of interest only in that they may be incorrectly interpreted as constituents of the alteration layer that forms during glass leaching. Use of the simple experimental approach outlined in Figure 2.1 will eliminate the opportunity for such reprecipitates to form.

EDAX and ESCA data suggest that the precipitates are composed primarily of oxides of zinc and iron and a $Ca\cdot PO_4$ species. The presence of these species may pose a difficulty in interpreting data on actinides which are known to be absorbed and coprecipitated by $Ca\cdot PO_4$ and iron oxide species. The chemical interactions between actinides in doped glasses and such precipitates would appear to be an interesting subject for future experimentation.

2.2 Dissolution/Reprecipitation

Results of calculations with the dissolution/reprecipitation model indicate that appreciable amounts of glass can dissolve due to reprecipitation effects and that reprecipitation can be enhanced with certain combinations of groundwater volume, exposed surface area of glass, and concentration of glass in solution. Experimental verification of the dissolution/reprecipitation model is under way.

2.2.1 Dissolution/Reprecipitation Kinetics

During the last quarter, the analysis of waste-form degradation has been devoted to continued studies of dissolution/reprecipitation kinetics. Initial efforts in this area have been summarized in previous reports(2.2, 2.3). As discussed therein, the simultaneous occurrence of glass dissolution and its subsequent reprecipitation as a more stable mineral (e.g., quartz) takes place when $C_0' < C < C_0$. Here, C is the instantaneous, time-dependent concentration, within a closed volume V of groundwater, of the glass component that controls dissolution. C_0' and C_0 are the saturation concentrations of this particular species relative to the precipitate and the glass, respectively. Within this regime, the rate at which C changes with time t was taken as

$$\frac{dC}{dt} = \frac{KS}{V} (C_o - C) + K' (C_o' - C) \quad , \qquad (2.1)$$

where K is a rate constant for glass dissolution, S is the surface area of glass exposed to the groundwater, and K' is an effective rate constant for growth of the precipitate.

In the original calculations(2.2), K' was chosen to be time-independent, and the predicted variation of C with t that resulted did indeed exhibit behavior that has been observed experimentally (e.g., nepheline dissolution with gibbsite precipitation, as reviewed by Lasaga(2.4)), i.e.,

- $C\ (t \rightarrow \infty) = \text{constant}$
- $C_0' < C\ (t \rightarrow \infty) < C_0$.

The original analysis was then generalized(2.3) to the case for which K' was treated as an increasing function of time. Such behavior might be expected, for example, for the growth of colloidal particles from solution, which, as they grow, present an increasing amount of surface area to the surrounding groundwater and thus are able to transport the dissolved species from solution at faster net rates. On the other hand, treatment of K' as a constant may be more characteristic of growth of the precipitate as layers on adjacent surfaces, for which the amount of exposed area remains approximately constant.

The simplest possible time-dependence was assumed for K', namely, a linear increase with time. However, even for this case the resultant variation of C with time was found to be relatively complex; the solution of Equation 2.1 would involve Dawson's integral, which is not an elementary function.

In order to apply Equation 2.1 to some specific illustrative cases, two alternative approaches could be employed: use the closed-form solution developed previously(2.3), employing a numerical approach to calculating the Dawson's integral that appears therein; or simply integrate Equation 2.1 directly, using some appropriate numerical method. For present purposes, the latter approach was followed.

Before carrying out the integration procedure, it is convenient to simplify Equation 2.1 by making appropriate combinations of variables and parameters to obtain a resultant form for this expression in which all quantities that appear are dimensionless. Toward this end, we repeat some quantities that were presented earlier(2.2,2.3). First, the time-dependent form assumed for K' is(2.3)

$$K'(t) = a + b\ (t - t_p), \qquad (2.2)$$

where a and b are time-independent parameters (but possibly temperature-dependent, although temperature variations are not being considered here), and the time t_p is defined such that

$$C(t_p) = C_0' \quad . \qquad (2.3)$$

Thus, times within the range $t > t_p$ are of interest in solving Equation 2.1. Clearly, the special case for which $b = 0$ corresponds to that which had originally been treated(2.2). Second, the following dimensionless quantities were defined:

$$s \equiv C/C_o \tag{2.4}$$

$$r \equiv C_o'/C_o \tag{2.5}$$

$$\beta \equiv \frac{aV}{KS} \tag{2.6}$$

$$\gamma \equiv b\left(\frac{V}{KS}\right)^2 \tag{2.7}$$

$$\tau \equiv KSt/V \tag{2.8}$$

$$\tau_p \equiv KSt_p/V \quad . \tag{2.9}$$

Also, as shown in Reference 2.2,

$$\tau_p = \ln\left(\frac{1}{1-r}\right) \quad . \tag{2.10}$$

Combining Equations 2.1 and 2.2 and 2.4 to 2.9, we obtain

$$\frac{ds}{d\tau} = 1 - r - [1 + \beta + \gamma\,(\tau - \tau_p)]\,(s - r) \quad . \tag{2.11}$$

A different dimensionless variable for time had been used previously to obtain the closed-form solution of Equation 2.1 (see Equations 2.4c-2.4g in Reference 2.3), but Equation 2.11 is convenient for present purposes.

For times within the interval $0 \leq t < t_p$, both β and γ are zero, and taking $s(\tau = 0) = 0$, the solution of Equation 2.11 becomes

$$s = 1 - \exp(-\tau). \tag{2.12}$$

Equation 2.10 is seen to follow directly by setting $s = r$ and $\tau = \tau_p$ in Equation 2.12. In addition, the solution of Equation 2.11, for the special case $\gamma = 0$, i.e., for which K' is time-independent, can be expressed in terms of elementary functions (Equation 2.24 of Reference 2.2).

We are now able to calculate the total amount, Q, of the species controlling glass dissolution that has actually gone into solution. In general,

$$\frac{dQ}{dt} = KS\,(C_o - C) \quad . \tag{2.13}$$

Equation 2.13 can be expressed in terms of dimensionless quantities using Equations 2.4 and 2.8, i.e.,

$$\frac{dq}{d\tau} = 1 - s \quad , \tag{2.14}$$

where

$$q \equiv \frac{Q}{C_o V} \quad . \tag{2.15}$$

Equations 2.13 and 2.15 are consistent with the terminology used in Reference 2.3 (Equations 2.5 and 2.28, respectively).

Closed-form expressions for $q(\tau)$ were developed in Reference 2.3 for two cases: $K' = 0$, and K' being time-independent (Equations 2.27 and 2.29, respectively). During the past reporting period, a numerical approach was used to obtain $q(\tau)$ for cases in which $\gamma > 0$; in this case, a fourth-order Runge-Kutta procedure was used to integrate Equations 2.11 and 2.14 simultaneously.

The results of some specific numerical examples are illustrated in Figures 2.4 to 2.7. Some general observations, based on these figures, are the following:

- Reprecipitation results in a decrease of the instantaneous concentration of glass in solution and an increase of the net amount of dissolved glass, as compared to the case for which no reprecipitation occurs. Indeed, the added amount of glass that has dissolved due to reprecipitation effects can be appreciable.
- An increase of γ (i.e., b) at constant β and r (i.e., a and C_o', respectively) results in an enhancement of the overall reprecipitation effect.
- Likewise, an increase of β at constant γ and r also enhances the overall reprecipitation effect, although the relative enhancement becomes less pronounced for the larger γ and τ values, for which the time-dependent term in K' dominates the time-independent term.
- A decrease of r at constant β and γ causes the reprecipitation effect to be enhanced.

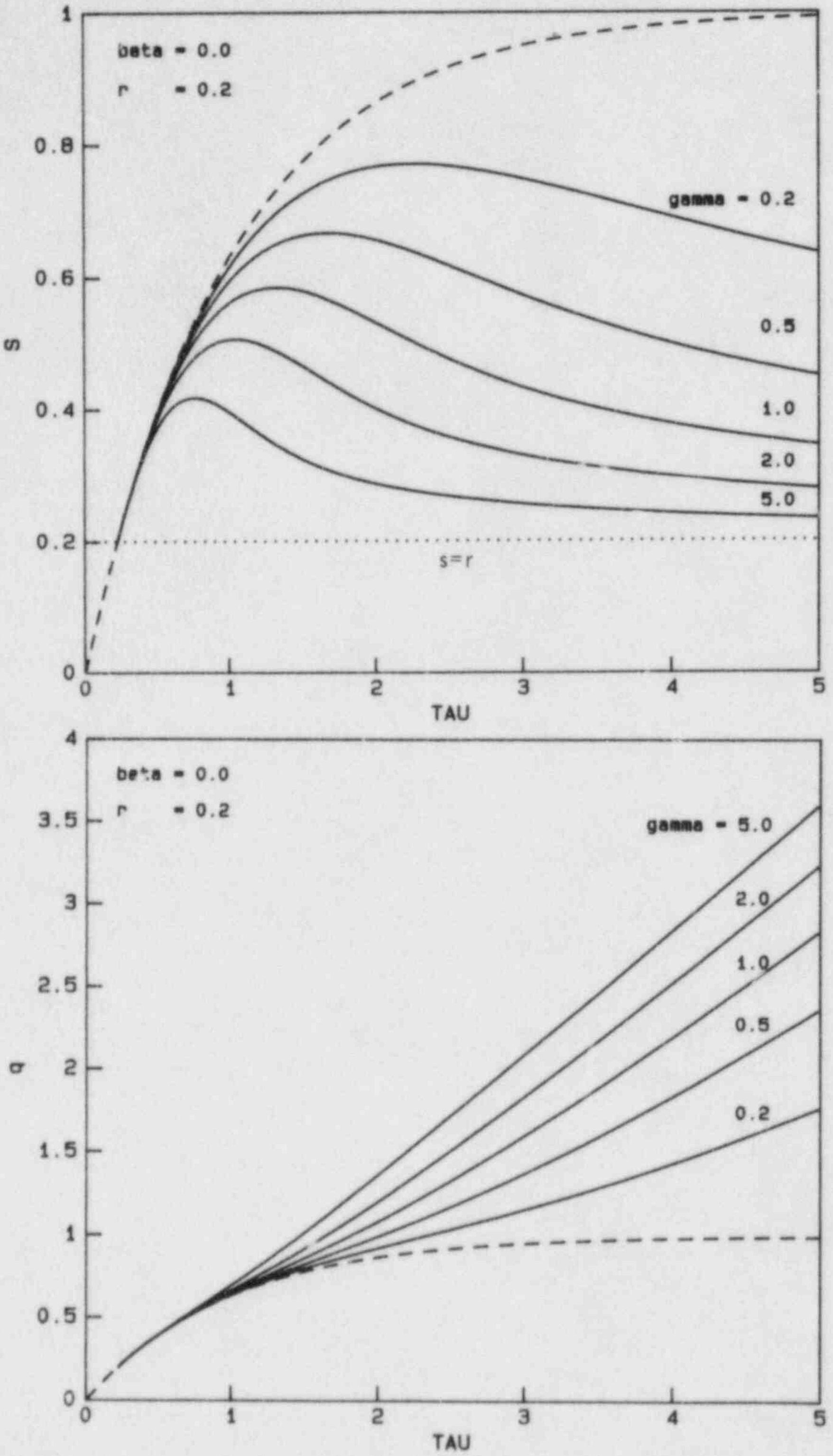

Figure 2.4. Variation of s and q with τ for β = 0.0, r = 0.2, and for selected values of γ.

The dashed curves correspond to β = γ = 0, i.e., no reprecipitation.

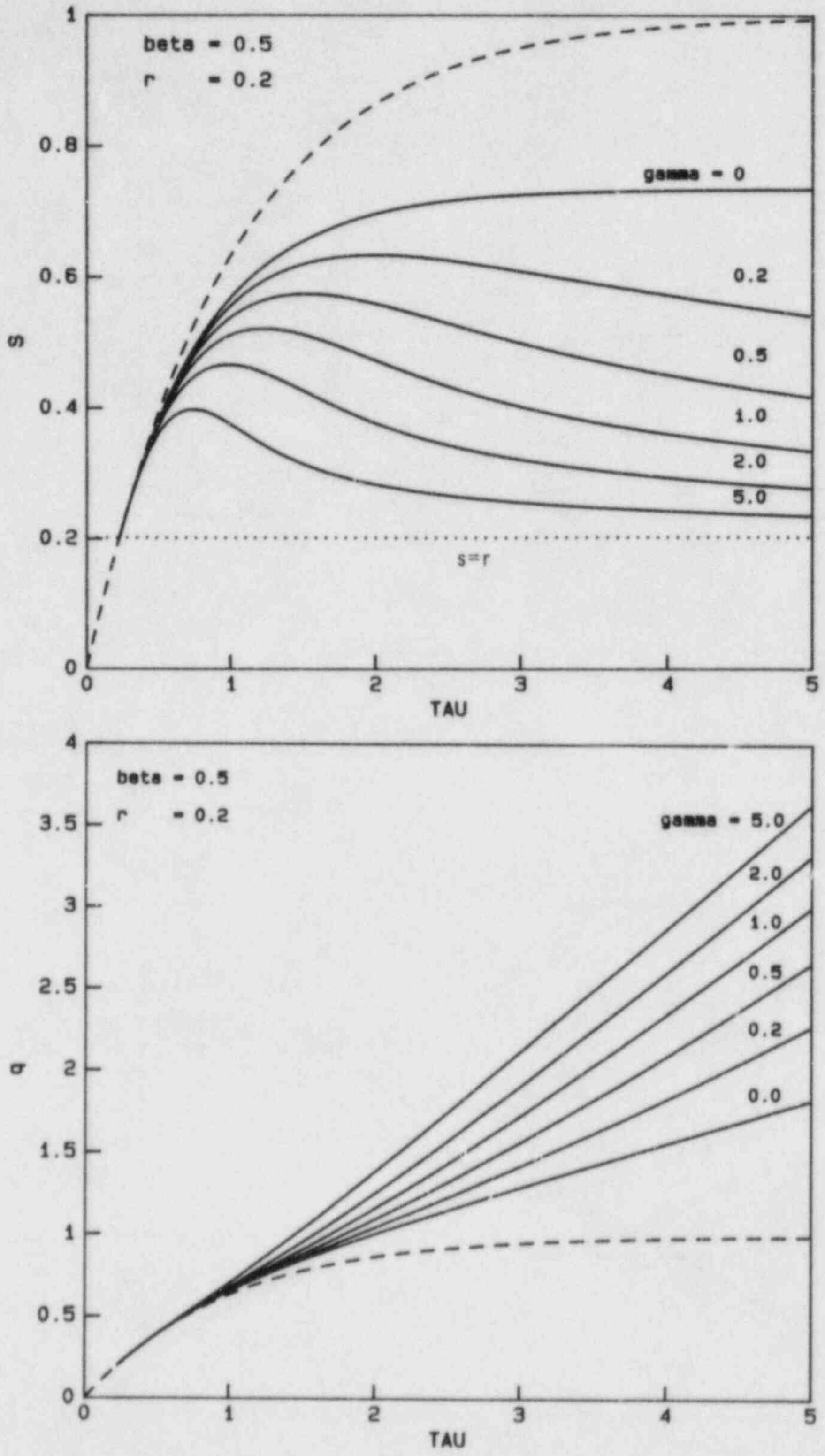

Figure 2.5. Variation of s and q with τ for $\beta = 0.5$, $r = 0.2$, and for selected values of γ.

The dashed curves correspond to $\beta = \gamma = 0$, i.e., no reprecipitation.

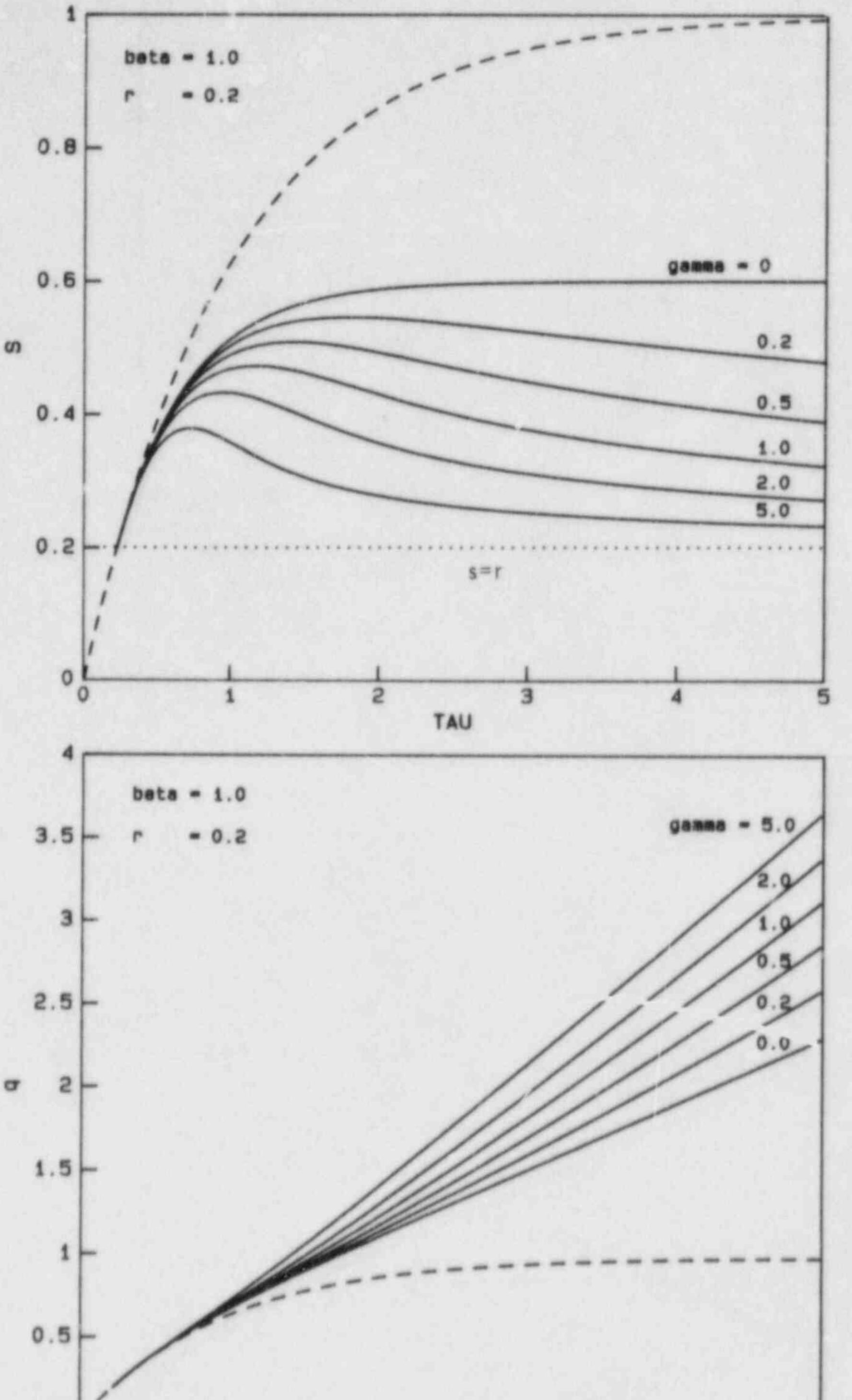

Figure 2.6. Variation of s and q with τ for $\beta = 1.0$, $r = 0.2$, and for selected values of γ.

The dashed curves correspond to $\beta = \gamma = 0$, i.e., no reprecipitation.

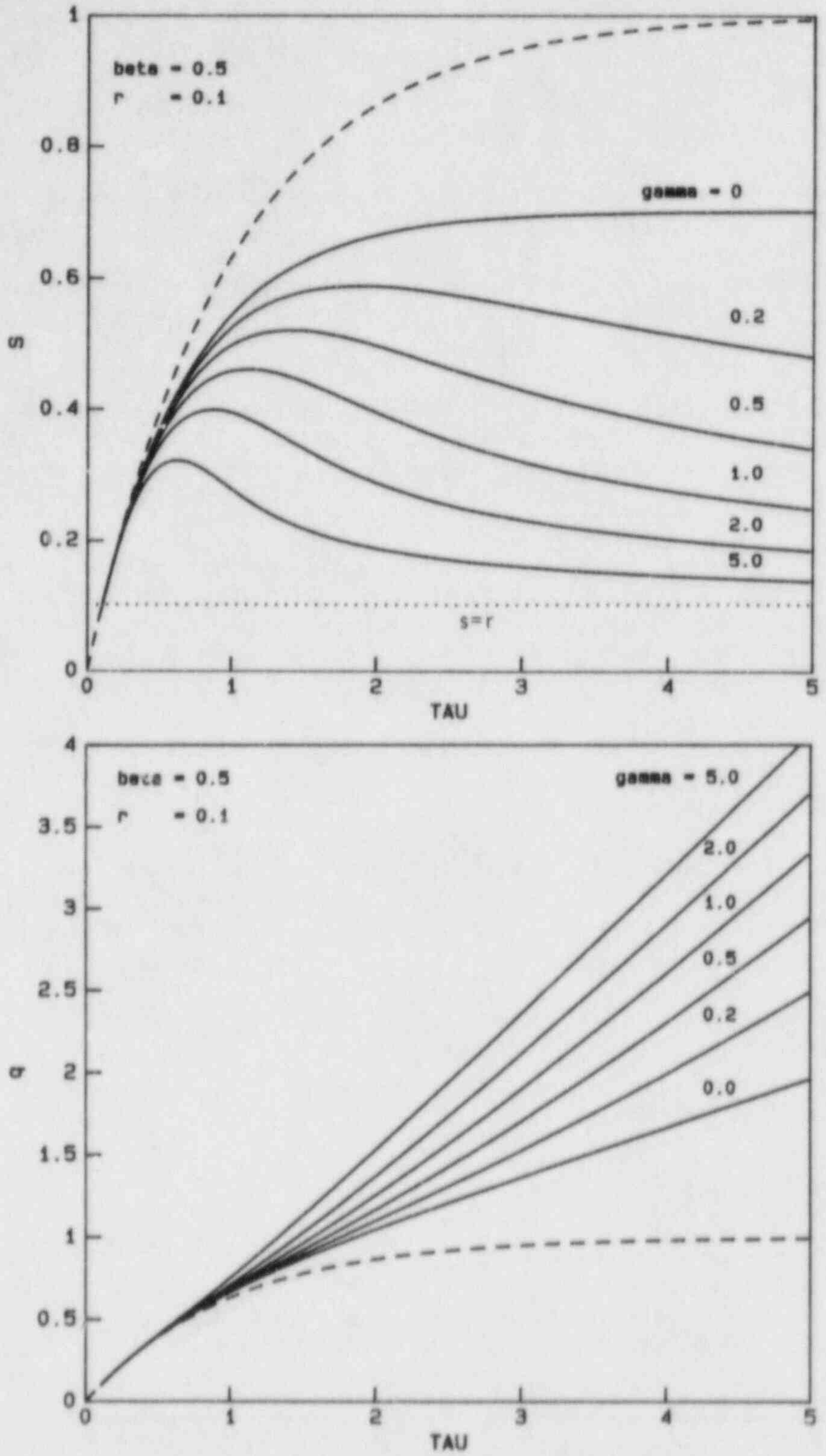

Figure 2.7. Variation of s and q with τ for $\beta = 0.5$, $r = 0.1$, and for selected values of γ.

The dashed curves correspond to $\beta = \gamma = 0$, i.e., no reprecipitation.

- For $\beta \neq 0$, $\gamma = 0$, the value of s asymptotically approaches a constant value that is greater than r but less than 1.
- For $\beta \neq 0$, $\gamma > 0$, the value of s attains a maximum and then asymptotically approaches the constant value $s = r$.

The last two observations are, in general, consistent with analogous experimental studies(2.4) and modeling studies(2.5,2.6) pertaining to various geological processes.

It must be emphasized that the mathematical form for K' used in this analysis was selected on a largely empirical basis. It should, however, present a reasonable description of gross features of the reprecipitation process.

Further studies in this area will be concentrated upon continued correlation of these modeling studies with analogous studies reported in the literature for geological systems. In addition, experiments of this general nature are to be conducted at Battelle and should lend further insight into both the kinetics of the process and the associated physical mechanisms.

2.2.2 Experimental Verification of the Dissolution/Reprecipitation

The dissolution/reprecipitation model interprets glass-waste-form dissolution as being controlled by the rate of glass dissolution into the groundwater. Equation 2.1 showed the proposed description of how the concentration of the glass component that controls dissolution changes over time.

In the experimental verification of this model, the temperature, volume of liquid, and exposed surface area of glass will be kept constant. Equation 2.1 is thus expressed

$$\frac{dC}{dt} = k(C_o - C) + K'(C_o' - C) \quad ,$$

where k is a constant proportional to the rate of glass dissolution. Figure 2.8 shows the relationship between time and concentration calculated by the model for the three cases of interest:

1. $K' = 0$ (i.e., no precipitation)
2. $K' =$ constant (i.e., a constant rate of precipitation)
3. $K' = f(t)$, where $f(t_1) < f(t_2)$ for $t_1 < t_2$ (i.e., the rate of precipitation increases over time).

To ensure the best possible accuracy in measurement of SiO_2 concentration, the experiment will be conducted at 90 C in bombs containing

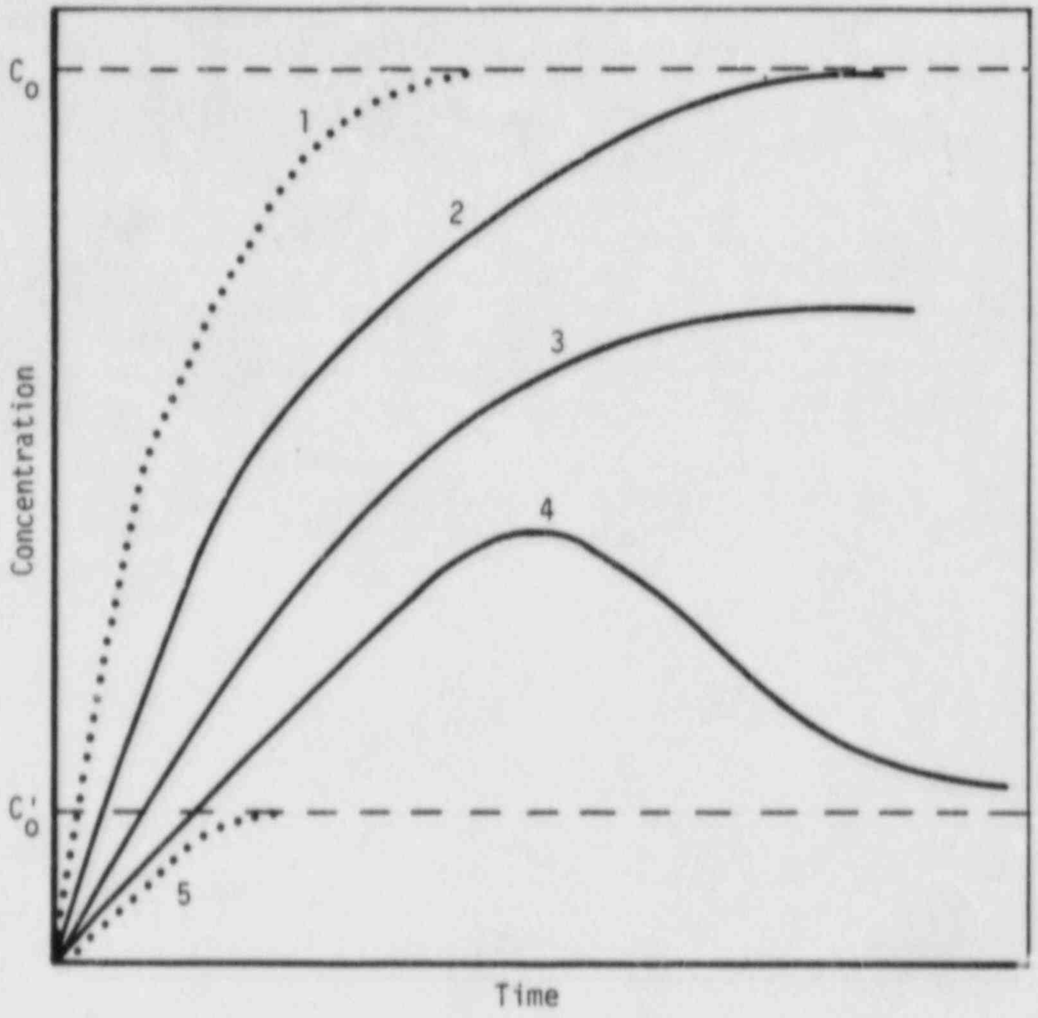

1. Dissolution of fused silica
2. K' = 0
3. K' = constant
4. K' increases over time
5. Dissolution of α-quartz

Figure 2.8. Relationship between time and concentration of the precipitating species for three cases of interest in the dissolution/reprecipitation model.

reagent-grade water with cubic specimens 1 cm on a side so as to maintain a surface-to-volume ratio of 0.01/mm, the MCC-1P condition. Because continuous glass-water contact is undesirable (as indicated in Section 2.1), all bombs will be inverted to prevent such contact during heating and cooling. To reach thermal equilibrium, the bombs will be placed in the oven for 24 hours before inversion to obtain glass/water contact. To prevent contact on cooling, they will be reinverted on removal from the oven.

The experimental matrix is shown in Table 2.6. The numbers in that table refer to the bombs, numbered 1-21. At the end of the 35th day, Bombs 1-9 will be cleaned and returned to the oven to provide additional samples. In this way, reasonably accurate measures of the dissolution/precipitation curves for MCC 76-68 glass, amorphous silica, and α-quartz can be obtained. This matrix will require 12 MCC 76-68 samples and 6 samples each of fused quartz and α-quartz. It will also include six blanks.

This experiment is under way, and some results should be available in time for the next quarterly report.

Table 2.6. Silica-dissolution-model experimental matrix.(a)

Sample	Exposure Time, Days											
	1	3	5	8(b)	11	14(b)	21	28(b)	35	42	56	70
MCC 76-68	1	2	3	4	5	6	7	8	9	10	11	12
Fused silica				1		4		7		13	16	19
α-quartz				2		5		8		14	17	20
Blank				3		6		9		15	18	21

(a) Numerals in table are bomb identification numbers.

(b) Bombs 1-9 will be subjected to digestion and cleaning procedures before being returned to the oven on the 49th day. After their return to the oven, Bombs 1-3 will be removed on Day 57, Bombs 4-6 on Day 63, and Bombs 7-9 on Day 77, counting from the beginning of the experiment.

2.3 Crystallinity Influences

The previous quarterly report[(2.7)] described an experiment for assessing the influence of volume fraction of crystallization at two different crystal sizes on removal of material from MCC 76-68 glass. The generation of these crystals requires doping MCC 76-68 glass with RuO_2, a melt insoluble expected to be present in the waste stream. These uniformly dispersed particles of RuO_2 will act as nucleating sites for growing crystals of specific size. A procedure for uniformly dispersing commercial RuO_2 powder in a melt of MCC 76-68 glass was developed during the quarter, and melts were prepared.

2.3.1 Procedure Development

Glass powder was crushed using a Wooly Beuhler crushing apparatus. Crushing surfaces are composed of carbon steel. The glass was crushed and sieved at 325 mesh. The coarse fraction was recycled through the Wooly Beuhler until all of the powder passed through the 325 mesh screen. Stock suspensions containing 5 g/liter each of the glass and RuO_2 powder were prepared using deionized water (specific conductivity less than 1.0 micromho/cm). After equilibration for 168 hours, 100-ml aliquots of the stock suspensions were used to prepare suspensions at different pH values. Reagent-grade nitric acid (HNO_3) or potassium hydroxide (KOH) were used to adjust the suspension pH values. The pH-adjusted suspensions were allowed to equilibrate for 168 hours prior to determination of their electrophoretic mobilities.

The electrophoretic mobility (EM) and the zeta potential (ZP) of the suspended particles are needed to determine the condition that leads to maximum dispersion and mixing of the MCC 76-68 glass powder and the RuO_2 powder.

The EMs of the suspensions as a function of solution pH were determined using the horizontal cell of a Rank Brothers Mark II Particle Electrophoresis Apparatus (Rank Brothers, Cambridge, U.K.). At least 5 particles were tracked at each electrode polarization on the EM measurements. The ZP was calculated from the EM using the Smoluchowski equation,

$$ZP = \frac{4\pi\eta}{e} EM \quad ,$$

where η is absolute viscosity and e is absolute permittivity of the solvent. For water at 23.5 C, the temperature at which the measurements were made, the Smoluchowski equation reduces to

$$ZP(23.5\ C) = 12.57 \times EM \quad ,$$

with ZP in millivolts and EM in units of microns per second per Volt per centimeter. Values for viscosity and absolute permittivity are obtained from the CRC Handbook of Chemistry and Physics.(2.8) The absolute permittivity is calculated by multiplying the relative permittivity (i.e., dielectric constant) by the permittivity of vacuum.

The pHs of the suspensions were determined using an Orion Model 811 pH meter connected to a research-grade pH electrode and a single-junction reference electrode. Standard buffer solutions supplied by Orion were used to calibrate the pH measurements.

Particle sizes were determined using a Horiba CAPA 500 centrifugal particle-size analyzer (Horiba, Inc., Irvine, California). Its method of operation combines centrifugation with light-turbidity to measure particle-size distributions from 0.02 microns to tens of microns. Particle-size distributions of the suspensions at various solution pHs were measured in aqueous solution. The 5 g/liter powder-concentration suspensions were too concentrated to measure the turbidity with the Horiba particle-size analyzer. Therefore, the suspensions were centrifuged to decrease the particle concentration and then sonicated with a Heat Systems 1/2-inch-diameter ultrasonic horn to redisperse the particles to measurable turbidity ranges (i.e., light-absorbance values of 1.0 to 0.75).

2.3.1.1 Observations

The median size of the particles in suspension varied very little as a function of pH, EM, or ZP. This finding may indicate either that the sonication prior to particle size analysis breaks up weak coagules or that ZP has little effect at the particle concentrations used in these measurements. The second possibility implies that in the highly concentrated suspensions used to prepare batch mixes of glass and RuO_2, solution-pH conditions that give the maximum ZP should be used. This will ensure optimum dispersion of the suspensions to minimize homocoagulation prior to mixing of the glass and RuO_2 suspensions.

The EM and ZP data give isoelectric points equal to pH = 6.9 and pH = 5.1 for the glass and RuO_2 suspensions, respectively. This result gives a range from pH = 5.1 to pH = 6.9 where heterocoagulation between the glass and RuO_2 particles may take place. Thus, mixing procedures may be designed to optimize or minimize this process.

2.3.1.2 Recommendations for Mixing Glass and RuO_2 Powders

The general approach to optimizing the homogeneity of the glass and RuO_2 mixture should:

1. Minimize homocoagulation by avoiding the isoelectric points of the two powders.

2. Maximize mixing of the two powders via heterocoagulation or complete dispersion of the mixture. The latter requires that the glass and RuO_2 particles remain in suspension or settle at the same rate.

Based on these features, two different approaches are recommended. The first is based on the concept of optimum dispersion of both suspensions It requires minimum coagulation in the suspension mixture and is achieved by mixing solutions of nearly equal pH. A RuO_2 suspension can be prepared at pH 9.0 by ammonium hydroxide (NH_4OH) additions. This suspension in the proper stoichiometry should be mixed with an equilibrium suspension of the glass at pH 9.70. The final pH of the mixture will be between pH 9.0 and pH 9.7, where both the glass and RuO_2 are negatively charged. The RuO_2 powder should be added to a solution already buffered to pH 9 to avoid the RuO_2 suspension passing through its isoelectric point.

The second mixing procedure takes advantage of the heterocoagulation that will take place between the RuO_2 and glass over the range from pH 5.1 to pH 6.9. The actual pH range that may be employed is more restricted, because of the criterion that the suspensions be well dispersed. To achieve such dispersion by this method, the suspension pH values should be adjusted to pH 6.2. This pH gives the maximum ZP for the two suspensions over the pH range where heterocoagulation may occur. The pH of the solvent prior to addition of RuO_2 powder can be adjusted with NH_4OH. The solvent pH for the glass suspension should be adjusted using HNO_3. Use of these reagents should minimize any deleterious effects from the salt ions.

2.3.2 Glass/RuO_2 Melts

For ease of experimental procedure, melts were made from powdered glass and RuO_2 mixed according to the maximum dispersion method. Two dispersions, one intended to provide 10^6 particles/cm^3 and the other 10^9 particles/cm^3, were prepared. These were melted at 1150 C and cast into bars. Evaluations of the final RuO_2 particle counts are under way.

2.4 References

(2.1) T. E. Jones, "Reference Material Chemistry--Synthetic Groundwater Formulation", RHO-BW-ST-37P (1982).

(2.2) "Long-Term Performance of Materials Used for High-Level Waste Packaging", D. Stahl and N. E. Miller (Compilers), NUREG/CR-3427, Vol. 4, BMI-2113 (June 1984), pp. 2-60 ff.

(2.3) "Long-Term Performance of Materials Used for High-Level Waste Packaging", D. Stahl and N. E. Miller (Compilers), NUREG/CR-3900, Vol. 1 (September 1984), pp. 2-8 ff.

(2.4) A. C. Lasaga, in Kinetics of Geochemical Processes (Rev. in Mineralogy, Vol. 8), A. C. Lasaga and R. J. Kirkpatrick (Editors), Mineralogical Soc. of America (Washington, D.C., 1981), p. 1 (see especially Figure 1 on p. 10).

(2.5) R. Wollast, Geochim. et Cosmochim. Acta, 31 (1967) 635.

(2.6) R. Wollast, in The Sea, E. W. Goldberg (Editor), Vol. 5, John Wiley & Sons, Inc. (New York, 1974), p. 359.

(2.7) "Long-Term Performance of Materials Used for High-Level Waste Packaging", D. Stahl and N. E. Miller (Compilers), NUREG/CR-3900, Vol. 1 (September 1984), pp. 2-3 ff.

(2.8) R. C. Weast, Handbook of Chemistry and Physics, 58th Edition, Chemical Rubber Company (1977-78).

3. CONTAINER MATERIALS

Potentiodynamic polarization tests were performed to determine the effects of single chemical species in the simulated basalt groundwater(3.1) on the cracking and pitting susceptibility of the carbon-steel overpack. (All future uses of "basalt groundwater" in this section refer to the synthetic groundwater formulation described in Reference 3.1). A matrix of additional tests is planned to investigate the relative importance of individual variables, such as chemical species and pH, in overpack corrosion. In studies of pitting kinetics, shallow pits were found to propagate in a simulated groundwater at 90 C, whereas deeper ones showed evidence of attack only at the pit mouth. Preliminary experiments with the electrochemical pit-propagation monitor were completed. Slow strain rate studies show that carbon steel is particularly susceptible to stress-corrosion cracking in aqueous $FeCl_3$ solutions at low strain rates.

In hydrogen-embrittlement studies, commercial-purity iron was characterized chemically and metallurgically and then subjected to tensile tests in hydrogen and in nitrogen. The results of these tests indicate that hydrogen has no effect on the strength of commercial high-purity iron; however, ductility was somewhat reduced.

Efforts in corrosion modeling included work on film-growth kinetics, the effects of oxidation-reduction reactions, and the mathematical description of pitting-induction time.

3.1 Overpack Corrosion

Studies of overpack corrosion have focused this quarter on three areas: potentiodynamic polarization studies, slow strain rate studies, and pitting-kinetics studies. All of the studies have been focused on the steel--basalt system. The objective of the potentiodynamic polarization studies is to evaluate the influence of groundwater chemistry on the potential for stress-corrosion cracking (SCC) and pitting. The objective of the slow strain rate studies is to confirm the results of the potentiodynamic polarization studies with regard to SCC and to investigate the effects of electrochemical potential, temperature, and composition in detail for the identified cracking agents. The objective of the pitting-kinetics studies is to investigate the effects of geometrical and environmental variables on pit propagation.

3.1.1 Potentiodynamic Polarization Studies

Potentiodynamic polarization curves were obtained using slow (0.6 V/hr) and fast (18 V/hr) scan rates on hot-rolled 1020 carbon steel. The studies were conducted at 90 C in groundwater alone and in groundwater to which selected chemical species had been added. Comparison of the curves obtained at the slow scan rate with and without each species present indicates the effects of that species on the cracking and pitting susceptibility of the steel. The curve obtained for each species at the fast scan rate was compared with the slow-scan-rate curve for that species to produce additional information on whether the species was likely to promote stress-corrosion cracking.

A matrix of potentiodynamic polarization tests is being designed to determine which of the selected variables have a statistically significant effect on polarization behavior (and thus on cracking and pitting susceptibility). These variables include solution pH, the presence of dissolved gases, and the presence of chemical species in the groundwater.

3.1.1.1 Effects of Single Species on Polarization Behavior

Potentiodynamic polarization experiments were performed on hot-rolled 1020 carbon steel at 90 C in argon-purged groundwater alone and in groundwater with various chemical species added.

As explained in the most recent annual report,(3.2) in this test procedure the polarity and magnitude of the current density flowing between a specimen of the material of interest and an inert counter electrode are measured as a function of electrochemical potential. For the anodic portions of the curve, the current measured is equal to the corrosion rate of the specimen if two conditions are met: (1) the electrochemical potential is sufficiently far away from the open-circuit potential that the rate of the cathodic reaction is negligible; and (2) the rates of parasitic oxidation reactions are negligible.

Schematics of anodic polarization curves showing several types of behavior are given in Figure 3.1. For the active-corrosion case, the anodic curve is linear on an E-log i plot, and the forward and reverse scans are coincident. The presence of a nose in the anodic portion of the curve is generally indicative of the onset of passivation. The value decreases with decreasing potential scan rate and may be negligibly small for a highly corrosion-resistant material. The occurrence of hysteresis between the forward and reverse scans is indicative of pitting. Where the hysteresis loop is very large, the protection potential may be very close to the open-circuit potential, indicating a high probability of pitting in service.

The potentiodynamic polarization technique also has been found to be useful in identifying potential stress-corrosion cracking (SCC) environments. It has been shown that SCC of carbon steel is associated with environments that promote active-passive behavior and that the electrochemical potential range for SCC is near to and more noble than E_{peak}. Moreover, it has been observed that severe cracking occurs in environments when i_{max} on the fast scan is greater than about 1×10^{-3} A/cm^2 and when the fast scan exhibits at least an order of magnitude higher currents than the slow scan.

The chemical composition of the steel is given in Table 3.1, and the species examined are given in Table 3.2, along with their concentrations. As discussed in the previous quarterly report, the species were selected based on results of analyses of basalt groundwaters and species that are possible due to radiolysis. The purpose of these experiments was to examine the effects of single chemical species on the polarization behavior of 1020 carbon steel.

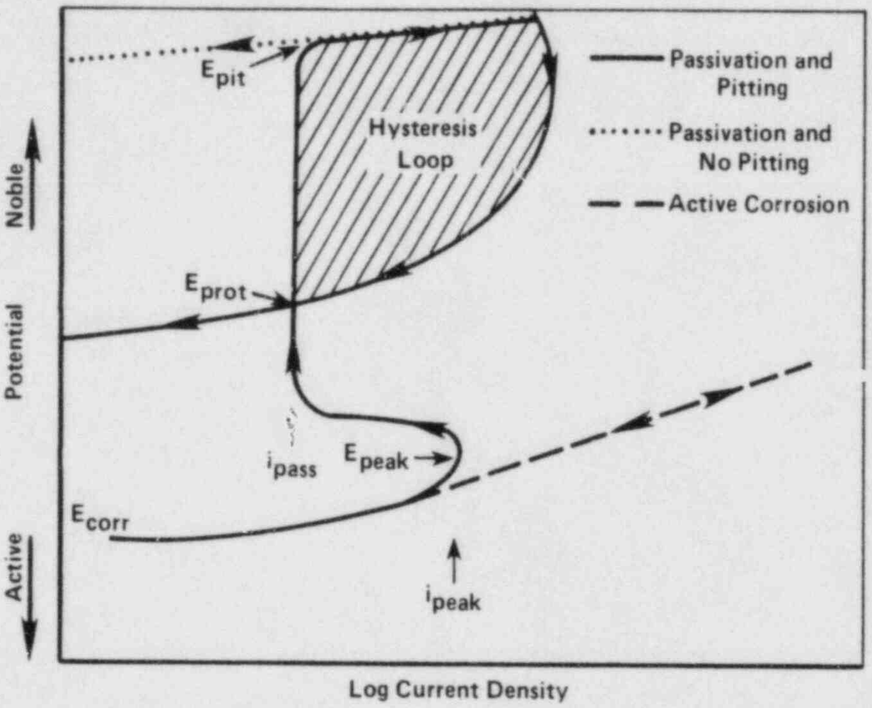

Figure 3.1. Schematic of typical anodic potentiodynamic polariation curves.

E_{corr} = corrosion potential; E_{pitt} = potential at which pits initiate on forward scan; E_{prot} = potential at which pits repassivate on reverse scan; i_{peak} = current density at active peak; i_{pass} = current density in passive range.

Table 3.1. Chemical compositions and other data on steels used in the corrosion studies.

SAE Number	Heat Treatment	Tests Used In	Dimensions	Composition, weight percent									
				C	Mn	P	S	Si	Cu	Sn	Ni	Cr	Mo
1018	Hot-Rolled	Pitting Exposures	7.6 cm x 15.2 cm strip	0.18	0.77	0.017	0.019	0.22	--	--	--	--	--
1020[(a)]	Hot-Rolled	Electrochemical Pitting Monitor, Potentiodynamic Polarization	1.27 cm rod	0.20	0.46	0.011	0.032	0.17	0.38	0.027	0.014	0.018	0.024
1020[(a)]	Hot-Rolled	Slow Strain Rate	0.635 cm dia. rod	0.22	0.55	0.01	0.037	--	--	--	--	--	--

[(a)] Hot-rolled 1018 carbon steel is not available in rod form.

Figure 3.2a shows the polarization curve for 1020 steel in groundwater alone. The curve exhibits active-passive pitting behavior. In the following discussion, all the curves are compared with this behavior to determine the effects of the addition of the various chemical species. Figure 3.2b compares the polarization behavior of 1020 steel in groundwater alone and in groundwater with 100,000 g/m^3 Cl^- added. The addition of Cl^- resulted in a decrease in the pitting potential, E_{pit}, which was expected.

Figure 3.2c shows that the addition of 10,000 g/m^3 F^- expanded the passive region for the steel in basalt groundwater by increasing E_{pit}. This effect was somewhat unexpected, but it is known that some species that promote passivation can act to promote SCC.

Figure 3.2d shows that the addition of 100 g/m^3 each of Fe^{+2} and Fe^{+3} increased the passive current density and decreased the protection potential, E_{prot}. The decrease in E_{prot} indicates an increase in susceptibility to pitting and/or crevice corrosion.

Figure 3.3a shows that the addition of 1000 g/m^3 Al^{+3} had a significant effect on the polarization behavior of 1020 steel. The passive current density was reduced. The pitting potential and E_{prot} were both greatly decreased; in fact, E_{prot} was more negative than the free-corrosion potential, E_{cor}, indicating that pitting and/or crevice corrosion could occur at E_{cor}. Crevice attack of the test coupon could account for the erratic i_{pas} observed.

Table 3.2. Concentrations of the chemical species added to the simulated basalt groundwater in the single species experiments.

Chemical Species	Concentrations, g/m^3
Cl^-	100,000
F^-	10,000
Fe^{+2}/Fe^{+3}	100/100
Al^{+3}	1,000
CO_3^{-2}/HCO_3^-	60,000/61,000 (1M/1M)
NO_3^-/NO_2^-	1,000/1,000
PO_4^{-3}	1,000
$BO_3^{-3}/B_4O_7^{-2}$	1,000/1,000
SiO_3^{-2}	1,000
H_2O_2	100
ClO_4^-	100

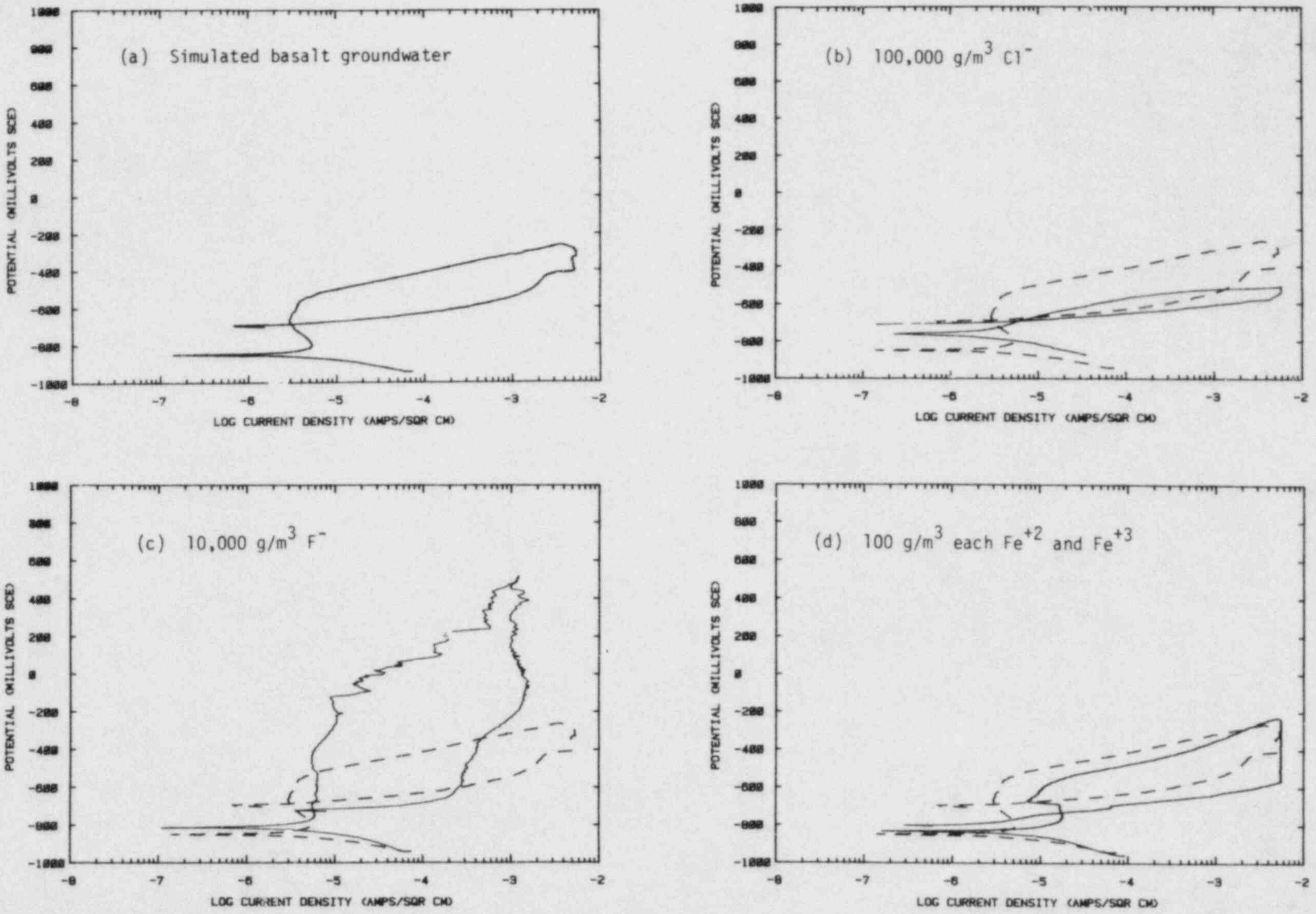

Figure 3.2. Potentiodynamic polarization curves for 1020 steel in argon-purged simulated basalt groundwater alone and with Cl^-, F^-, or Fe^{+2}/Fe^{+3} added.

The dashed curves indicate the baseline curve shown in Figure 3.2a.

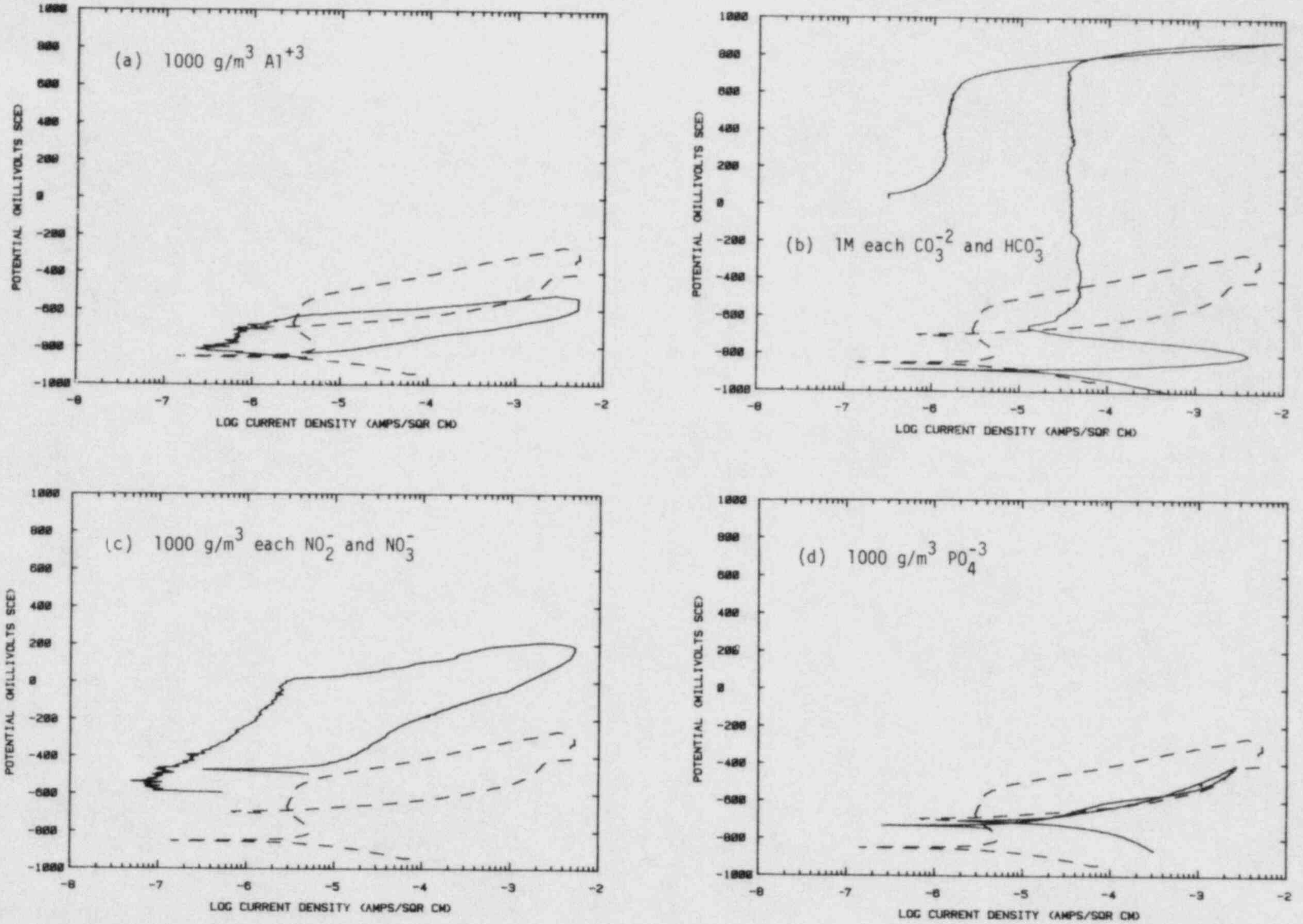

Figure 3.3. Potentiodynamic polarization curves for 1020 steel in argon-purged simulated basalt groundwater with Al^{+3}, CO$_3$$^{-2}$/HCO$_3$$^-$, NO$_2$$^-$/NO$_3$$^-$, or PO$_4$$^{-3}$ added.

The dashed curves indicate the baseline curve shown in Figure 3.2a.

Figure 3.3b shows the very large effect of adding 1M CO_3^{-2}/1M HCO_3^- to the simulated basalt groundwater. The current density of the active corrosion peak, i_{max}, was increased nearly three orders of magnitude. An active peak of this magnitude (> 10 mA/cm^2) has been associated with SCC, and CO_3^{-2}/HCO_3^- is a known cracking environment. The passive current density was also increased, and no pitting was observed.

Figure 3.3c shows that the addition of 1000 g/m^3 each of NO_2^- and NO_3^-, known SCC agents, greatly decreased i_{pas} and increased E_{cor}. The NO_2^-/NO_3^- additions also greatly increased E_{pit} and E_{prot}.

Figure 3.3d shows the effect of adding 1000 g/m^3 of PO_4^{-3}, a known SCC agent, on the polarization behavior of 1018 steel. The PO_4^{-3} addition produced active corrosion of the steel with no indication of a passive region. The promotion of active corrosion may be important in propagating stress-corrosion cracks, assuming an active dissolution model for the mechanism of SCC in carbon steels.

Figure 3.4a shows that the addition of 1000 g/m^3 each of BO_3^{-3} and $B_4O_7^{-2}$ promoted passivation of the 1018 steel. The pitting potential was increased, but no significant effect on active corrosion or the magnitude of i_{pas} was observed.

Figure 3.4b shows the effect of adding 1000 g/m^3 of SiO_3^{-2} on the polarization behavior of 1020 steel. The passive current density was greatly reduced, and E_{pit} greatly increased. Although E_{prot} was only slightly reduced, E_{cor} was increased to a value more positive than E_{prot}, indicating the possibility of pitting and/or crevice corrosion. The polarization behavior for SiO_3^{-2} additions is similar to that of NO_2^-/NO_3^- additions; these are known cracking agents.

Figure 3.4c shows the effect of adding 100 g/m^3 of H_2O_2 on the polarization behavior of 1020 steel. Hydrogen peroxide acts as an oxidizer, significantly increasing the total rate of the reduction reaction. This increase resulted in a large increase in E_{cor}. The polarization behavior indicates active behavior, but an E_{prot} was observed, indicating pitting attack. Because $E_{prot} < E_{cor}$, pitting and/or crevice corrosion could have initiated at crevice sites created by the holder-specimen interface during exposure at E_{cor}.

Figure 3.4d shows that the addition of 100 g/m^3 of ClO_4^- promoted passivation of the 1020 steel. The passive current density decreased, and E_{pit} increased. Although the magnitude of the effect is much less, it is similar to that for NO_2^-/NO_3^- and SiO_3^{-2} additions.

In summary, all the selected species affected the polarization behavior to some degree. The polarization experiments identified Al^{+3}, NO_2^-/NO_3^-, SiO_3^{-2}, and ClO_4^- as significantly decreasing i_{pas}; PO_4^{-3} and possibly Cl^- or H_2O_2 as promoting active corrosion; and CO_3^{-2}/HCO_3^- as producing a significant increase in i_{max} and still maintaining passive behavior.

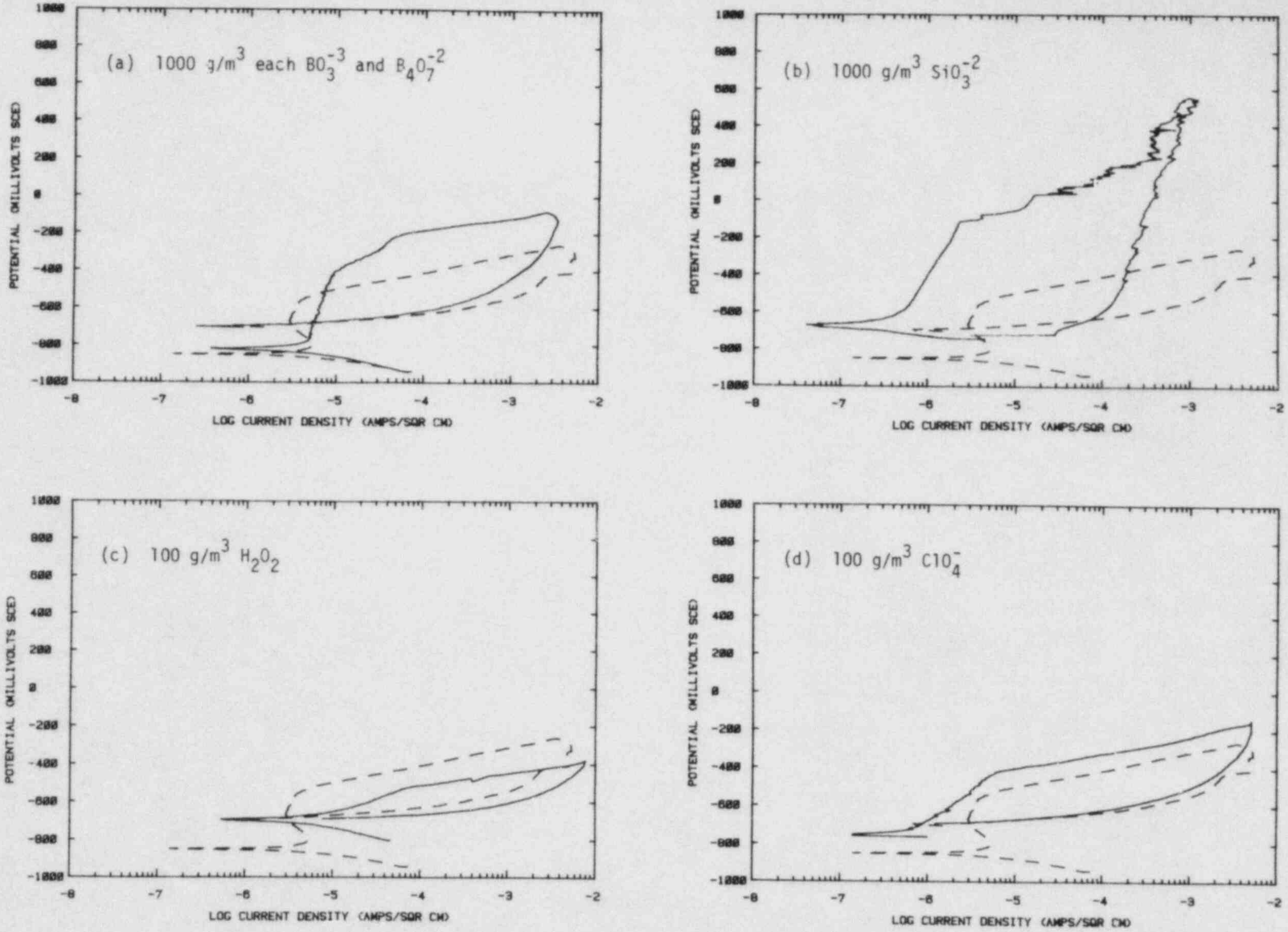

Figure 3.4. Potentiodynamic polarization curves for 1020 steel in argon-purged simulated basalt groundwater with $BO_3^{-3}/B_4O_7^{-2}$, SiO_3^{-2}, H_2O_2, or ClO_4^- added.

The dashed curves indicate the baseline curve shown in Figure 3.2a.

3.1.1.2 Effects of Single Species and Scan Rate on Polarization Behavior

The potential effects of these species on SCC susceptibility were examined further by performing fast scan rate (18 V/hr) polarization curves for comparison with the slow scan rate (0.6 V/hr) curves presented in Figures 3.2-3.4. These curves are shown in Figures 3.5-3.7. In most cases, the fast scan polarization curves are displaced to much higher current values than the slow scan polarization curves. For example, with Al^{+3} added (Figure 3.6a) there are over two orders of magnitude difference in the currents at approximately -0.70 V, SCE. However, the fast scan current is still only approximately 3×10^{-4} A/cm^2, which is low for cracking environments previously studied. The CO_3^{-2}/HCO_3^- solution (Figure 3.6b) exhibited the general behavior expected of cracking agents, but i_{max} for the fast scan was actually less than i_{max} for the slow scan. This behavior is not readily explained except that the Cl^- and F^- present in the groundwater may have affected the polarization behavior observed; in other CO_3^{-2}/HCO_3^{-2} environments i_{max} for the fast scan is typically greater than i_{max} for the slow scan.

3.1.1.3 Statistically Designed Experiments

The 32-test, 15-variable matrix of polarization curves which will determine main effect terms for the variables, free of two-factor interactions, has been completed. In addition to the species listed in Table 3.1 and solution pH, the following gas additions are being examined: O_2, H_2, and CO. The final analysis has not been completed. However, several of the 32 solution combinations exhibit behavior that is indicative of SCC environments, i.e., i_{max} of the fast scan is greater than 1×10^{-3} A/cm^2, and the fast scan exhibits at least one order of magnitude higher current than the slow scan.

3.1.2 Pitting-Kinetics Studies

Results of the potentiodynamic polarization experiments and autoclave exposures suggest that pit initiation in low-carbon steels is likely in basalt groundwater. The polarization curves exhibit considerable hysteresis on the reverse scans, and protection potentials are very near the corrosion potentials, even for deaerated solutions. In the autoclave exposures, pits actually were found on specimens exposed for approximately 1000 hours in a deaerated simulated basalt groundwater at 250 C. Accordingly, experiments were undertaken to characterize the pit-propagation behavior of carbon steel in simulated basalt-repository environments.

Two types of experiments were initiated: long-term exposures of "prepitted" specimens, and electrochemical pit-propagation experiments. In the former, simulated pits of various depths and aspect ratios (depth/diameter ratios) were mechanically drilled in specimens of hot-rolled 1018 carbon steel and are being exposed at 90 C in deaerated and

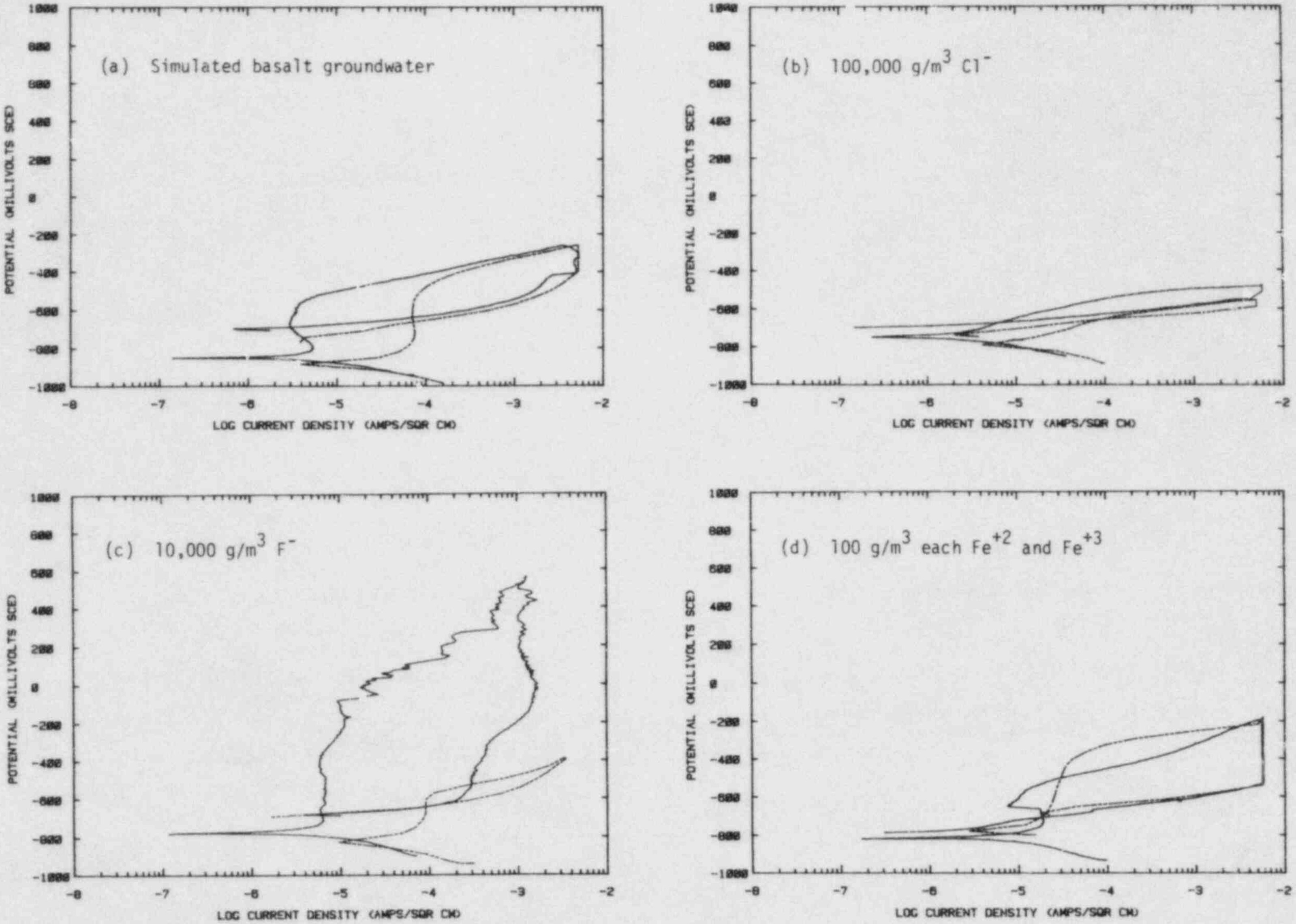

Figure 3.5. Fast- and slow-scan potentiodynamic polarization curves for 1020 steel in simulated basalt groundwater alone and with Cl^-, F^-, or Fe^{+2}/Fe^{+3} added.

The dotted curves were obtained at the slow scan rate.

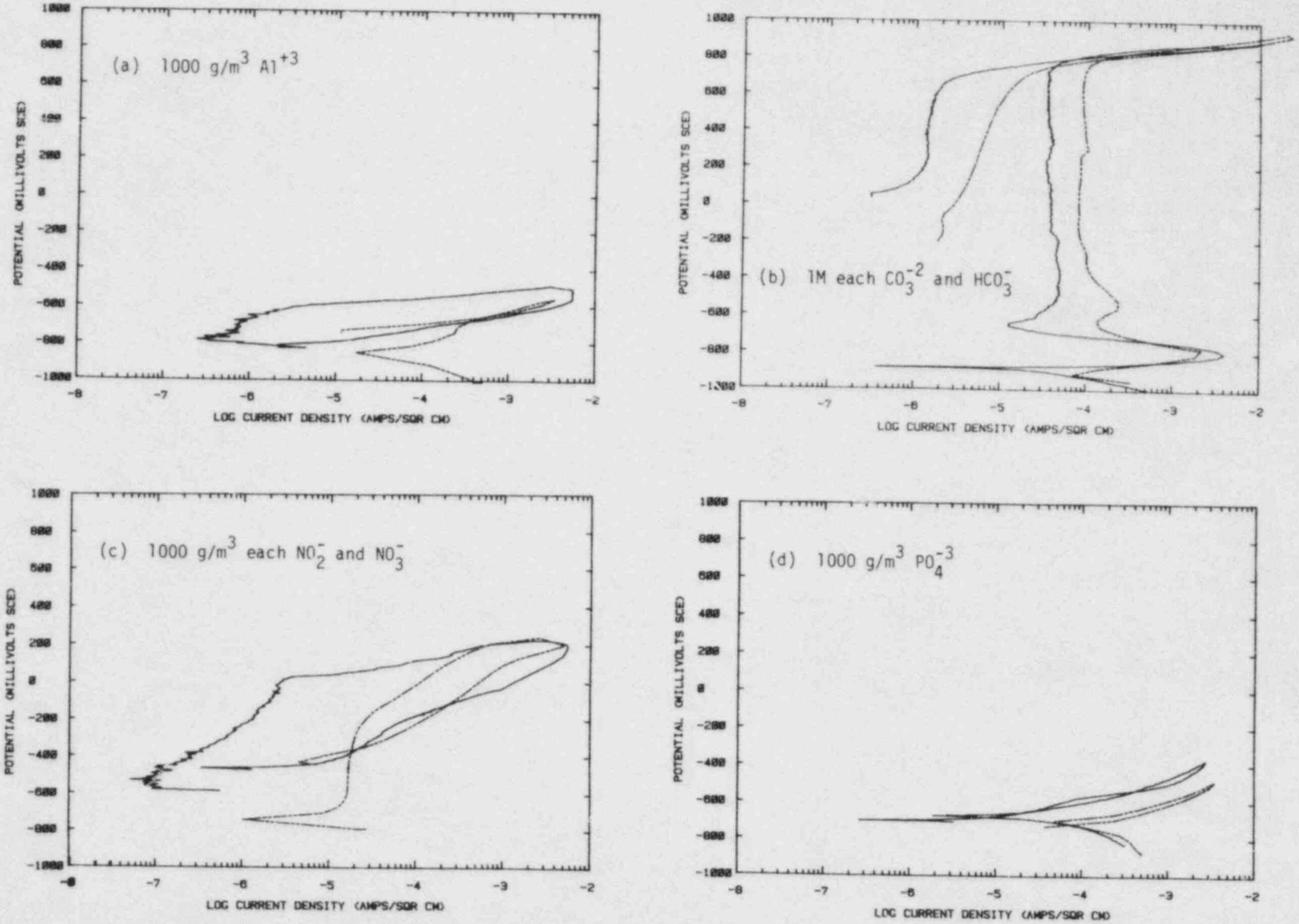

Figure 3.6. Fast- and slow-scan potentiodynamic polarization curves for 1020 steel in simulated basalt groundwater with Al^{+3}, CO_3^{-2}/HCO_3^-, NO_2^-/NO_3^-, or PO_4^{-3} added.

The dotted curves were obtained at the slow scan rate.

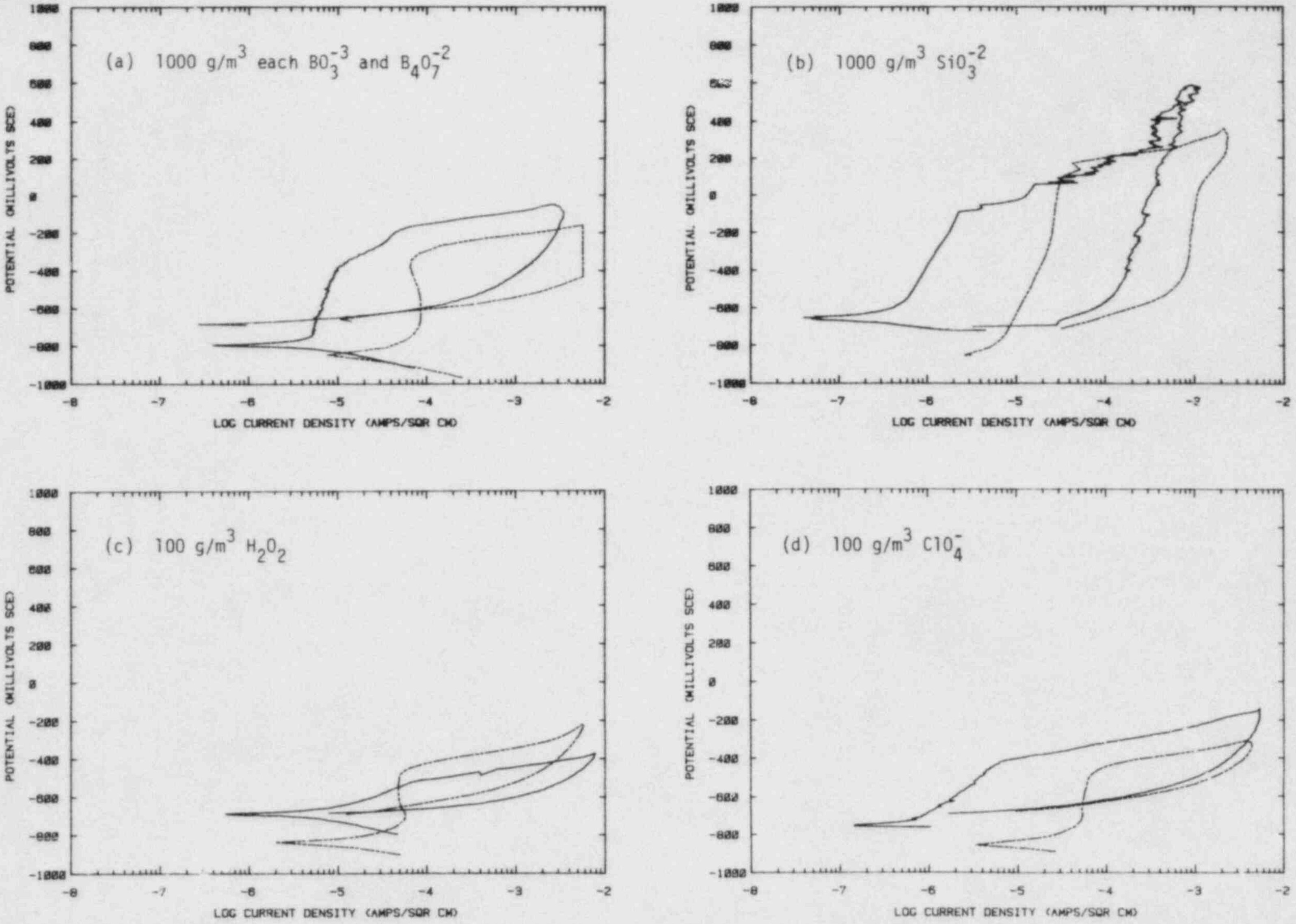

Figure 3.7. Fast- and slow-scan potentiodynamic polarization curves for 1020 steel in simulated basalt groundwater with $BO_3^{-3}/B_4O_7^{-2}$, SiO_3^{-2}, H_2O_2, or ClO_4^- added.

The dotted curves were obtained at the slow scan rate.

in oxygenated basalt groundwater. The steel used in this study was commercially obtained, and its composition is given in Table 3.1. Prior to exposure, the depths of the pits were measured with a micrometer having a thin needle point; after exposure, the specimens are being metallographically sectioned so that the morphology and depth of attack can be studied.

Four different pit diameters are being examined: 5.1 mm (0.2 inch), 2.54 mm (0.10 inch), 1.35 mm (0.05 inch), and 0.53 mm (0.021 inch). For each diameter, there are three aspect ratios: 2:1, 5:1, and 10:1. Thus, for a 5.1-mm-diameter pit, the initial pit depths were 10 mm, 25 mm, and 50 mm. The overall specimen dimensions are about 40 mm long x 20 mm wide x 75 mm thick (in the dimension of the pit) and the specimens were machined from 7.6 cm (3 inch) x 15.2 cm (6 inch) strip steel.

Prior to exposure, the specimens were cleaned with acetone, each of the pits was filled with the simulated basalt groundwater using a syringe, and the specimens were placed in high-density polyethylene vessels which contained 1 inch of crushed basalt rock. In each vessel, an electrical connection was attached to one specimen for subsequent potential measurements. The basalt-groundwater solution was added and the vessels were sealed. They were then placed in oil baths, Luggin probes were connected, and the flow of nitrogen or oxygen was started (for deaerated and aerated solutions, respectively).

During the experiments, the electrochemical potential of one specimen in each vessel is being monitored, and aliquots of solution are being taken periodically for pH analysis. Results of the potential measurements completed to date are given in Figure 3.8. These data show that the potentials of the specimens in the deaerated vessels varied between about -700 and -750 mV (SCE) over the first 2 months of exposure, whereas the potentials of the specimens in the aerated vessels exhibited a marked increase after about 1 month of exposure and stabilized at about -220 mV (SCE).

The results of the pH measurements are given in Table 3.3. The measurements were taken frequently over the first several weeks of exposure to establish the trends, but less frequently thereafter to conserve the solutions and minimize contamination of the deaerated solutions with oxygen. These data show some interesting trends. The pHs of all the solutions decreased over the first 24 hours from about 9.8 to about 7.5, and the pHs of the deaerated solutions have continued to decrease somewhat over the first 2 months of exposure. On the other hand, the pHs of the aerated solutions have increased over the 2-month period to values around 11.5. The mechanism for this pH increase is not fully understood but will be investigated in the next reporting period.

Altogether, eight prepitted specimens were removed from the vessels, following 4 months of exposure, and were optically examined. Specimens containing mechanical pits of each diameter were removed from both

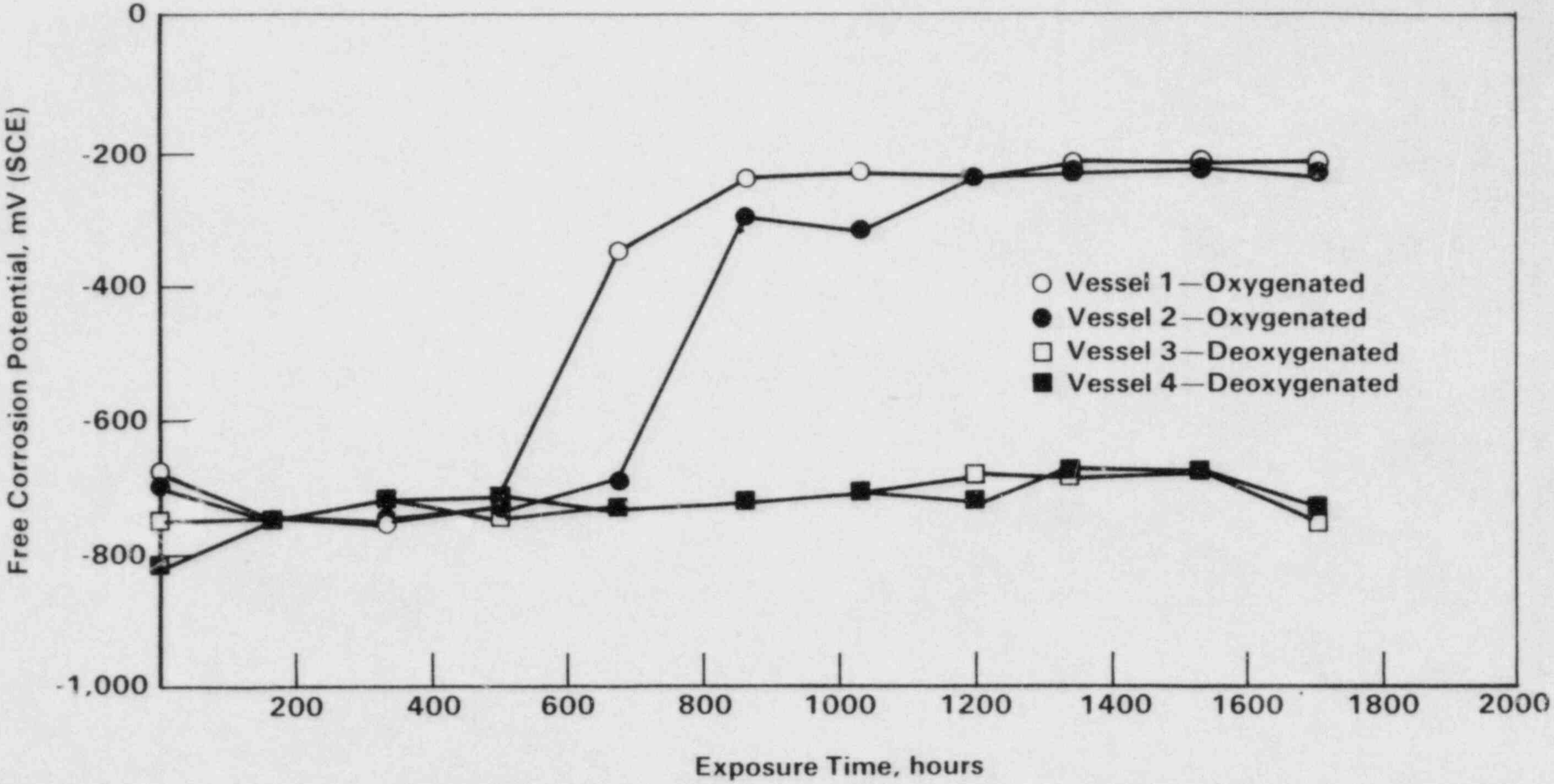

Figure 3.8. Electrochemical potential as a function of exposure time for mechanically prepitted 1018 carbon steel containing crushed basalt at 90 C.

Table 3.3. pH as a function of exposure time for simulated basalt groundwater solutions in contact with basalt rock and 1018 carbon steel specimens.

Exposure Time (hours)	pH			
	Oxygenated		Deaerated	
	Vessel 1	Vessel 2	Vessel 3	Vessel 4
0	9.8	9.8	9.8	9.8
24	8.0	7.6	7.0	7.4
72	7.4	7.4	7.2	7.8
168	7.5	7.5	7.5	7.5
336	7.8	7.9	7.5	7.5
1080	11.2	11.5	7.5	7.5
2208	11.2	11.5	6.5	6.6

oxygenated and deaerated vessels. All specimens from the oxygenated vessels were covered with thick, red rust deposits, and the pits were all capped with corrosion products. On the other hand, specimens taken from the deaerated vessels were covered with thin black deposits, and the pits were not capped. Figure 3.9 illustrates some of these features as they appeared in specimens with 2.54-mm-diameter pits.

Following optical examination, the specimens were metallographically sectioned, mounted, and polished, and the depths of the pits were measured with a microscope having a calibrated stage. No systematic trend in pit depth was evident from the data. The differences between the initial (preexposure) and final pit depths varied about ± 0.1 mm, which probably simply reflects the error in the measurement.

A close examination of the metallographic sections of the specimens exposed in the deaerated vessels did not indicate any evidence of appreciable attack. Similarly, the 5.1-mm, 2.45-mm, and 1.35-mm pits in the specimens exposed in the oxygenated vessels did not exhibit appreciable attack. Optical photographs of metallographic sections of the latter specimens are shown in Figures 3.10 to 3.12. On the other hand, the smallest-diameter pits exposed in the oxygenated vessels did show evidence of attack. The attack occurred over the entire pit for the lowest aspect ratio pit (2:1), whereas it occurred only near the mouth of the deeper pits. There is also evidence that the attack followed stringers in the midwall of the pits (see Figures 3.13 to 3.17).

Since attack was observed in the small-diameter pits in the oxygenated exposures, the absence of significant attack in the larger-diameter pits may simply indicate that long times are required to develop the acidic conditions necessary for pit propagation. The localization of the attack near the mouth of the deep, small-diameter pits is an interesting observation since it suggests that high-aspect-ratio pits are not stable in this system. Preliminary results of the electrochemical work are consistent with this suggestion. A possible explanation for this behavior is that the solution conductivity limits the distance of separation of the cathode (on the external surface) and the anode within the pits. Where solution conductivity is higher, such as with more concentrated solutions, this effect may be less pronounced.

Preliminary experiments were completed with the electrochemical pit-propagation monitor. The schematic of the monitor is shown in Figure 3.18. Experimentally, the monitor is oriented vertically in a test cell containing an electrolyte, and the current flow between the base of the simulated pit and the boldly exposed surface is monitored as a function of exposure time. Current measurements provide an estimation of the rate of pit propagation; the rate measured may be nonconservative since the reduction reactions occurring on the pit base will contribute to pit propagation but will not be detected. This current may be significant where a very-low-pH environment develops within the pit.

Oxygenated

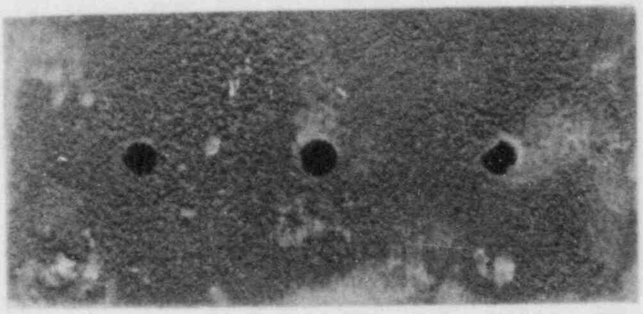

Deaerated

Figure 3.9. Low-power photograph of prepitted hot-rolled 1018 steel specimens following exposure in oxygenated and deaerated simulated basalt groundwater containing crushed basalt at 90 C.

Note that the pits on the specimen in the oxygenated solution are capped with corrosion products.

Figure 3.10. Low-power optical photograph of metallographic section of prepitted (5.1-mm-diameter) specimen of hot-rolled carbon steel following exposure in oxygenated simulated basalt groundwater containing crushed basalt.

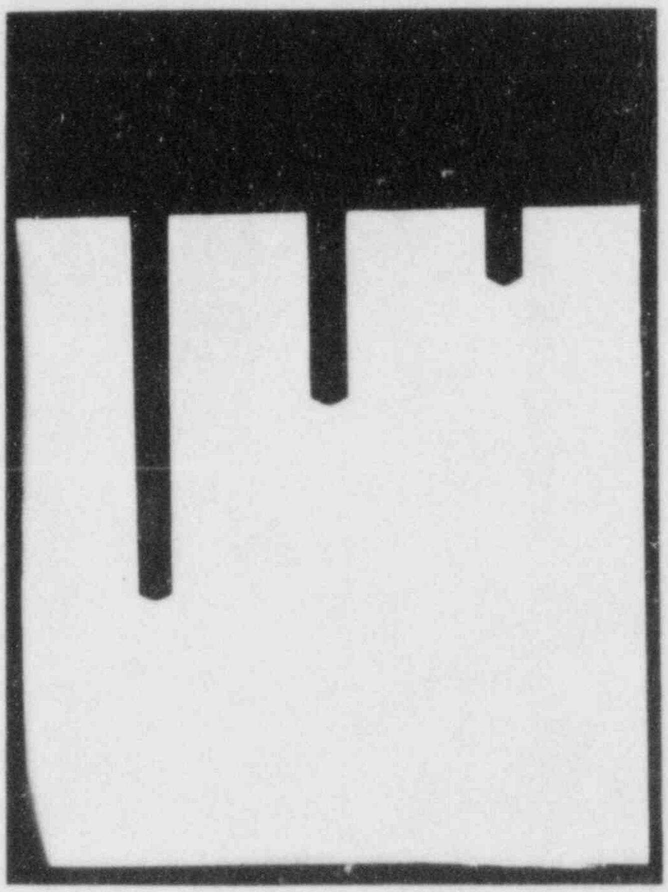

Figure 3.11. Low-power optical photograph of metallographic section of prepitted (2.54-mm-diameter) specimen of hot-rolled carbon steel following exposure in oxygenated simulated basalt groundwater containing crushed basalt.

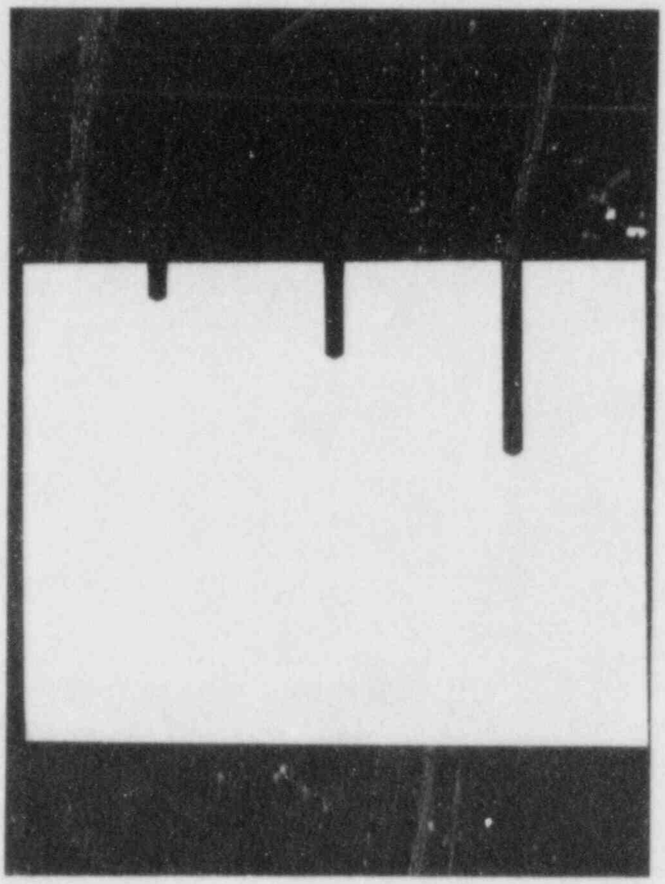

Figure 3.12. Low-power optical photograph of metallographic section of prepitted (1.35-mm-diameter) specimen of hot-rolled carbon steel following exposure in oxygenated simulated basalt groundwater containing crushed basalt.

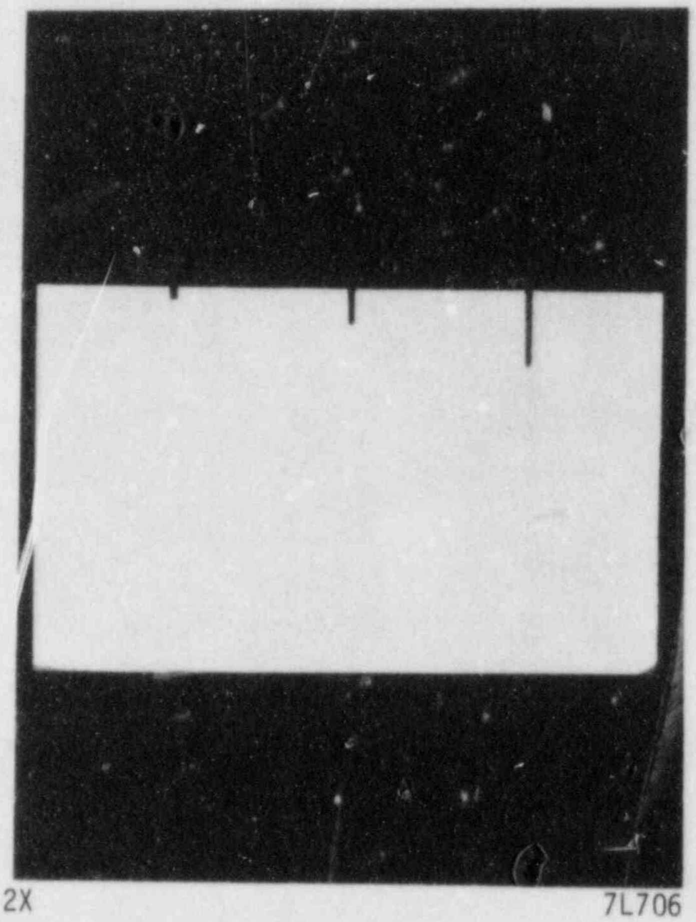

Figure 3.13. Low-power optical photograph of metallographic section of prepitted (0.53-mm-diameter) specimen of hot-rolled carbon steel following exposure in oxygenated simulated basalt groundwater containing crushed basalt.

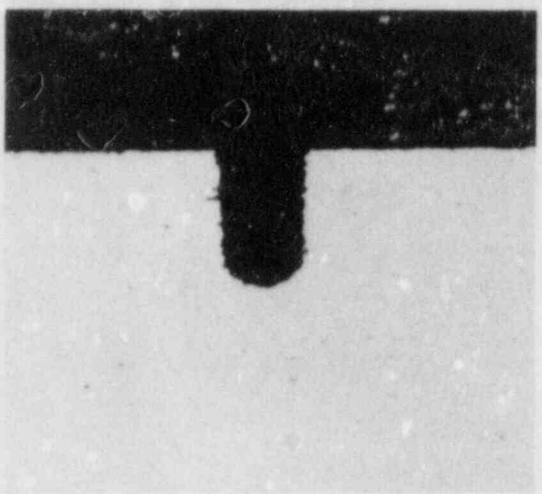

Figure 3.14. Optical photograph of 2:1 aspect-ratio pit shown in Figure 3.13.

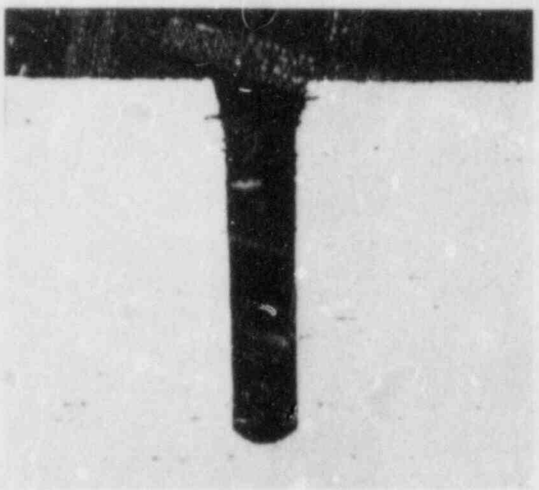

Figure 3.15. Optical photograph of 5:1 aspect-ratio pit shown in Figure 3.13.

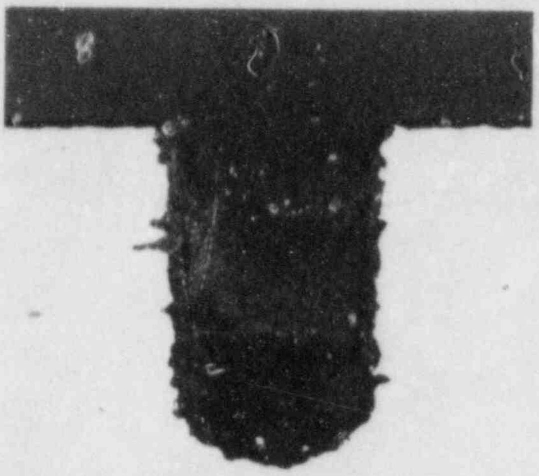

Figure 3.16. Higher-power optical photograph of pit shown in Figure 3.14.

Figure 3.17. Higher-power optical photograph of pit shown in Figure 3.15.

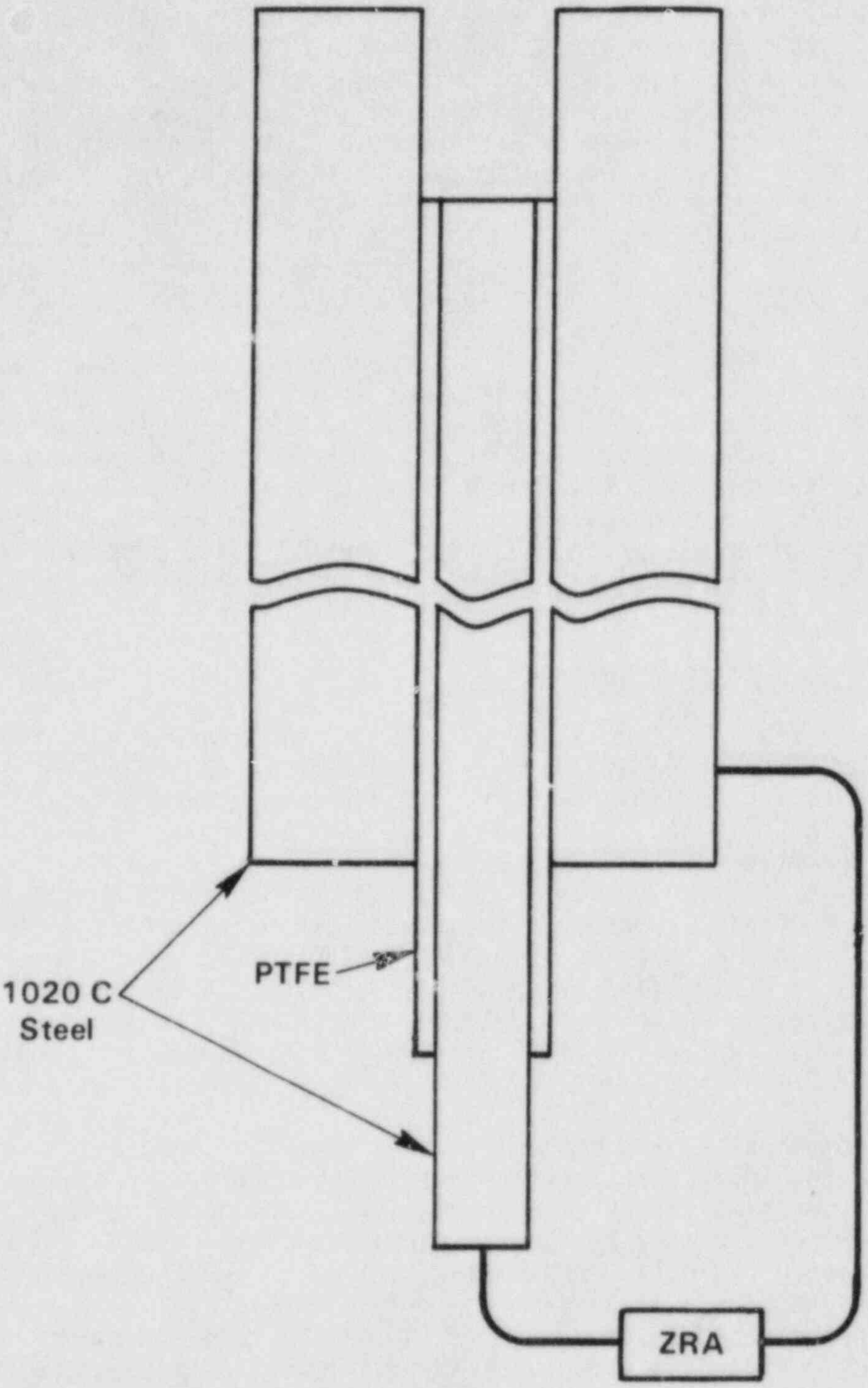

ZRA = Zero Resistance Ammeter

Figure 3.18. Schematic of pit-propagation monitor.

The preliminary experiments were performed in oxygenated basalt groundwater at 75 C and using two aspect ratios, 2:1 and 10:1. It was found that the pits did not initiate within about 1 week of exposure; currents were actually negative, indicating protection of the pit base. It is possible that this behavior was the result of the absence of a cap over the pits, which is necessary to prevent oxygen ingress into the pits and migration of protons out of the pits. Accordingly, the pits were stimulated for about 24 hours at 10 to 20 mA/cm^2 anodic current using a potentiostat and a platinum counter electrode. The boldly exposed portion of the pit monitor was allowed to corrode freely during this stimulation. Following stimulation, both pits initiated, and the 2:1-aspect-ratio pit stabilized at a current of about 50 μA/cm^2 over 7 days, corresponding to a rate of approximately 580 μm/y (23 mil/y). On the other hand, the 10:1-aspect-ratio pit did not stabilize, and eventually the current actually became cathodic. These results appear consistent with the results of the exposure tests in that the shallow pit propagated but the deep one did not. However, an optical examination of the electrochemical pit-propagation monitors following exposure indicated that the 10:1 aspect ratio pit had not fully occluded, which may account for the inability to stabilize pitting in this specimen.

3.1.3 Slow-Strain-Rate Studies

In the literature, several species which may be present in the repository were identified as potential stress-corrosion cracking agents. Of these, $FeCl_3$ or chloride + ferric oxides or hydroxides are potentially the most problematic, since chlorides are present in the groundwater and since corrosion of the overpack would generate ferrous ions which may be oxidized to ferric ions by radiolysis or oxygen ingress. Strauss and Bloom(3.3) first reported on the stress-corrosion cracking of low-carbon steels by ferric chloride solutions in 1961. Transgranular cracking was observed in pressurized capsule tests at 316 C at very low concentrations of ferric chloride, 0.001M, and in aqueous slurries of FeOOH or Fe_2O_3 and NaCl. On the other hand, NaCl + Fe_3O_4 did not produce cracking (see Table 3.4).

Although the stress-corrosion cracking observed by Strauss and Bloom may be relevant to overpack performance, it has not been established whether stress-corrosion cracking of carbon steel will occur at lower temperatures, which are more typical of waste repositories, or in more complicated aqueous solutions containing typical groundwater species. Moreover, it was not evident from the original reference whether the cracking occurred in the vapor or in the liquid phase within the capsules. Accordingly, an experimental investigation was undertaken to reproduce the stress-corrosion cracking observed in the original reference and to examine the influence of temperature and solution chemistry on stress-corrosion cracking of low-carbon steels in these ferric-chloride solutions.

During this reporting period, slow strain rate tests were performed on hot-rolled 1020 carbon steel in 0.001M ferric chloride at 315 C over a

Table 3.4. Effect of various solutions and slurries containing Fe (III) and/or chloride on cracking at 316 C.(3.3)

	Capsule Contents	Result of Treatment*
(1)	0.001 M $FeCl_3$	Capsules cracked and leaked within 6 to 15 hours.
(2)	0.0001 M $FeCl_3$	Very shallow cracks were produced within 1 week.
(3)	0.0005 M $Fe_2(SO_4)_3$	No cracking observed within 1 week.
(4)	0.001 M $Fe(NO_3)_3$	No cracking observed within 1 week.
(5)	0.003 M NaCl	No cracking observed within 1 week.
(6)	0.001 M NaCl	No cracking observed within 1 week.
(7)	0.1 M NaCl	Slight attack at weld junction during 1 week.
(8)	1 M NaCl	Localized corrosion in martensite penetrated welds within 20 hours.
(9)	Aqueous slurry of γ-FeOOH containing 0.6% Cl^-	Capsules cracked and leaked within 6 hours.
(10)	Aqueous slurry of γ-FeOOH generated by corrosion in 0.0005% Cl^-	Capsules cracked and leaked within [illegible] hours.
(11)	Aqueous slurry of γ-FeOOH generated by corrosion in high purity water	No cracking observed within 1 week.

*At least three and usually more capsules were given each treatment.

Table 3.4. Continued.

	Capsule Contents	Result of Treatment*
(12)	Slurry of γ-FeOOH in line 11 and 0.0001 M $FeCl_3$	Capsules cracked and leaked 16 to 18 hours.
(13)	Aqueous slurry of α-FeOOH containing 0.01% Cl	Shallow cracks were produced within 1 week.
(14)	Supernatant liquid γ-FeOOH slurry in line 9	No cracking observed within 1 week.
(15)	Slurry of α-FeOOH in line 13 and liquid in line 14	Capsules cracked and leaked within 3 to 4 hours.
(16)	Slurry of α-FeOOH containing 0.001% Cl^- and 0.003 M NaCl	Moderately deep cracks were produced within 1 week.
(17)	Slurry of γ-Fe_2O_3 containing 0.01% Cl^- and 0.003% M NaCl	Moderately deep cracks were produced within 1 week.
(18)	Slurry of α-Fe_2O_3 containing 0.02% Cl^- and 0.003 M NaCl	Very deep cracks were produced within 1 week. One capsule cracked and leaked within 4 days.
(19)	Slurry of Fe_3O_4 containing < 0.01% Cl^- and 0.003 M NaCl	No cracking observed within 1 week.

*At least three and usually more capsules were given each treatment.

range of strain rates to attempt to reproduce the stress-corrosion cracking data reported in the literature and to establish the optimum strain rate for future stress-corrosion testing. The composition of the steel used is given in Table 3.1. Stress-corrosion cracking was readily produced in the liquid phase. The cracking was transgranular, with some branching (see Figures 3.19 and 3.20), and was similar in morphology to that reported by Strauss and Bloom.

A summary of the results of slow strain rate tests which were performed at various strain rates is given in Table 3.5. These data show that susceptibility, based on the maximum depth of cracking, was highest at the lowest strain rate. This is unfortunate, experimentally, since a slow-strain rate test at 1×10^{-8}/sec may last several weeks or more.

Table 3.5. Results of slow strain rate tests performed on hot-rolled 1020 carbon steel in 0.001 M $FeCl_3$ at 315 C.

Strain Rate	Time to Failure (hours)	Maximum Depth of Cracking (mm)	Cracking Velocity (mm/s)
1×10^{-8}/s	393	0.30	2.10×10^{-7}
6×10^{-8}/s	146	0.11	2.09×10^{-7}
6×10^{-7}/s	59.2	0.20	9.53×10^{-7}

3.1.4 Future Work

Potentiodynamic polarization, pitting-kinetics, and slow strain rate studies will continue.

3.1.4.1 Potentiodynamic Polarization Studies

The statistical analysis of the 15-variable matrix of polarization curves will be completed. The main matrix of polarization experiments will be started.

3.1.4.2 Pitting-Kinetics Studies

The exposures of the prepitted specimens will continue. Based on the results of the 2-month exposure, the next specimen pull will be delayed until 8 months of total exposure time has elapsed. An understanding of the mechanism for the pH increase will be pursued and experimentally verified if possible. Procedures to consistently occlude the pits in

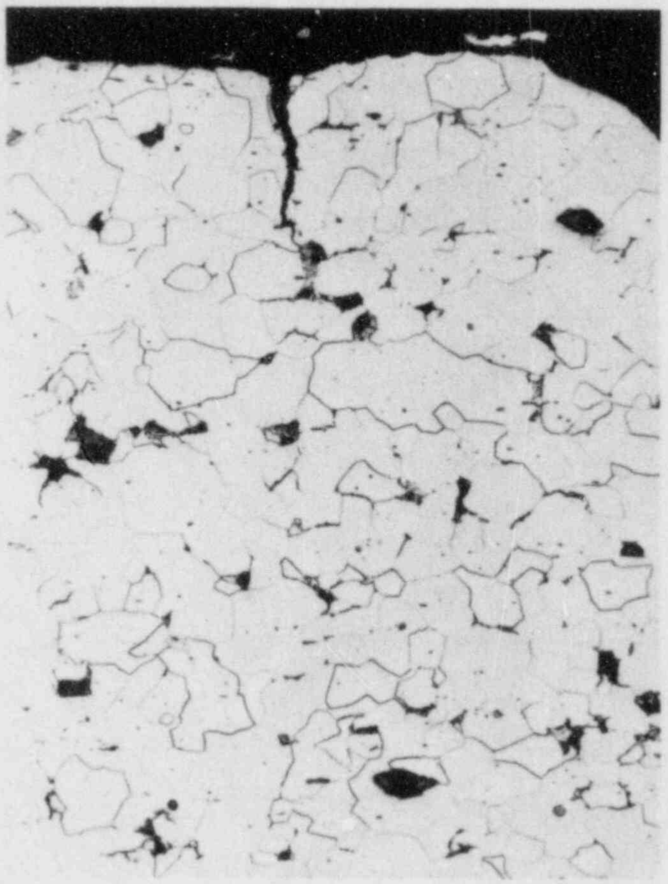

250X

7L544

Figure 3.19. Optical photograph of metallographic section of a slow strain rate specimen which was tested in 0.001 M $FeCl_3$ at 315 C and a strain rate of $6 \times 10^{-8}/s$.

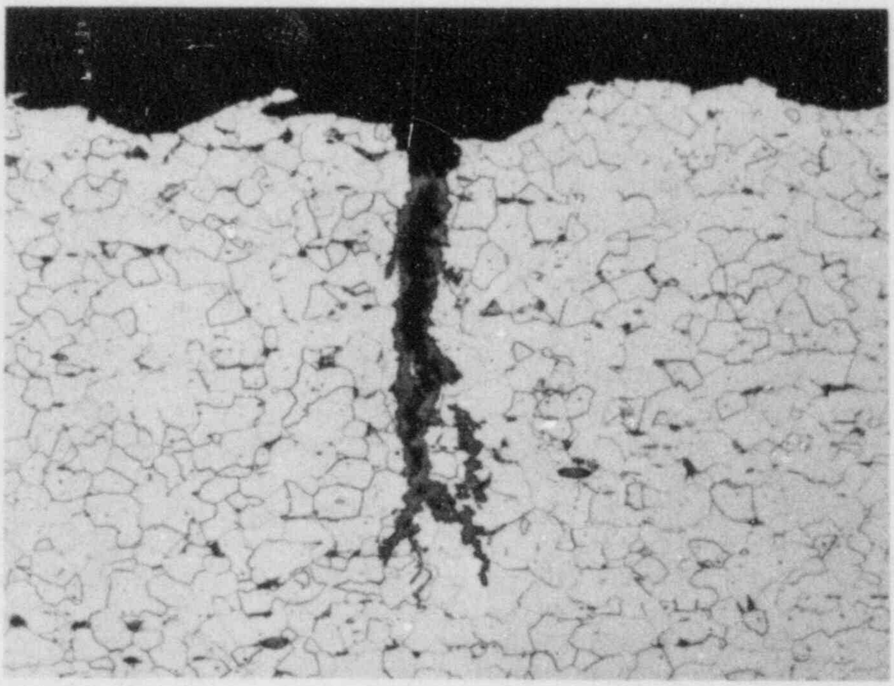

Figure 3.20. Optical photograph of metallographic section of a slow strain rate specimen which was tested in 0.001 M $FeCl_3$ at 315 C and a strain rate of 1×10^{-8}/s.

the electrochemical pit-propagation monitors will be studied. Two promising approaches are to pack the pits with an aqueous slurry of Fe_3O_4 prior to testing or to cap the pits with zirconia frits.

3.1.4.3 Slow Strain Rate Studies

The effect of temperature and $FeCl_3$ concentration on stress-corrosion cracking in simulated basalt groundwater will be studied over the temperature range of about 200 to 315 C.

3.2 Hydrogen Embrittlement

Hydrogen-embrittlement studies are being conducted to evaluate the potential for degradation by hydrogen of the container structural components. Hydrogen is expected to be present as a result of corrosion and/or radiolytic reactions. During the previous work, studies have been conducted with low-carbon cast steels having different impurity contents and with different thermal and thermomechanical treatments. In those studies, the steels exhibited substantial hydrogen-induced losses in resistance to crack initiation (J_{IC}, the fracture toughness) but little loss in resistance to crack growth (T, the tearing modulus) in the as-cast and the hot-rolled conditions. However, in the annealed condition the steels underwent significant reductions in both J_{IC} and T, irrespective of impurity content. This observation suggests that containers that were reasonably resistant to hydrogen embrittlement when cast may become susceptible to embrittlement with time at elevated temperature in a repository.

During the current year, the effect of repository temperatures on resistance to embrittlement will be studied in a cooperative effort with Manufacturing Sciences Corporation (MSC), another NRC contractor. MSC is planning to study the effect of repository temperatures on changes in the cast-steel microstructure and has agreed to provide samples for hydrogen-embrittlement studies at Battelle. Samples of cast steel were provided to Battelle recently by MSC, and additional samples should be received shortly. In addition, studies of the potential for embrittlement of a commercial high-purity iron provided by Armco, Incorporated, are being conducted in anticipation of the consideration of iron as a corrosion-allowance material that is more resistant to localized corrosion than is cast steel. Studies with the iron are under way, and results to date are reported below.

3.2.1 Evaluation of Iron Ingots Provided by Armco

Twelve small laboratory ingots approximately 7 inches long, 3 inches wide, and 1 inch thick (approximately 17.8 cm long, 7.6 cm wide, and 2.5 cm thick) of commercial high-purity iron were provided by Armco for use in studies of hydrogen embrittlement and corrosion at Battelle and for studies of weldability at MSC. The ingots were produced in the laboratory but had chemical compositions that could be achieved in large castings produced using present practice at Armco. The chemical composition of one ingot from which tensile specimens were prepared is presented in Table 3.6.

Table 3.6. Composition of iron ingot from which tensile specimens were prepared.

Element	Content, weight percent*
Carbon	0.000
Manganese	0.004
Phosphorus	0.003
Sulfur	0.004
Silicon	0.170
Aluminum	0.001
Copper	0.068
Nickel	0.020
Chromium	0.045
Molybdenum	0.044
Vanadium	0.001

*Average of two emission-spectrographic analyses.

Metallographic sections were prepared from each of the castings. Figure 3.21 presents a photomacrograph of a transverse section through the ingot from which tensile specimens were prepared. The figure illustrates the solidification pattern and the very coarse grain size that was apparent in all of the castings. This coarse grain size is further illustrated in Figure 3.22. The photomicrographs in Figure 3.23 show very fine particles, which were present in the grains, and somewhat coarser particles at the grain boundaries. These particles exhibited a lamellar structure (Figure 3.23b) and may have been fine pearlite precipitates, even though the bulk carbon content was below the detectable level in spectrographic analysis. No inclusions were observed. It is interesting to note that the photomicrograph in Figure 3.23a was taken at the same magnification as were earlier photomicrographs of the cast steels.(3.4) Comparison between those photomicrographs indicates that the grain size of the iron is approximately 5 times that of the steel studied previously in the as-cast condition.

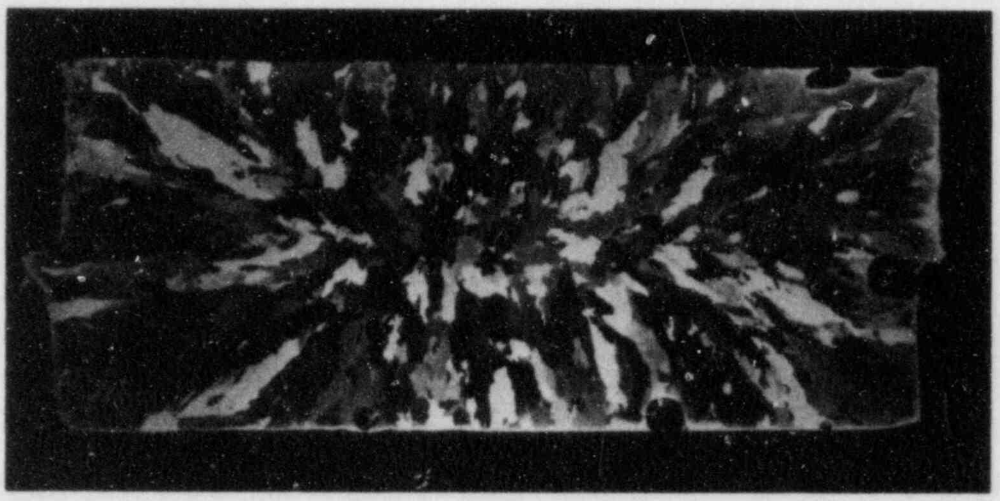

7L387

Figure 3.21. Transverse section through iron ingot from which tensile specimens were prepared.

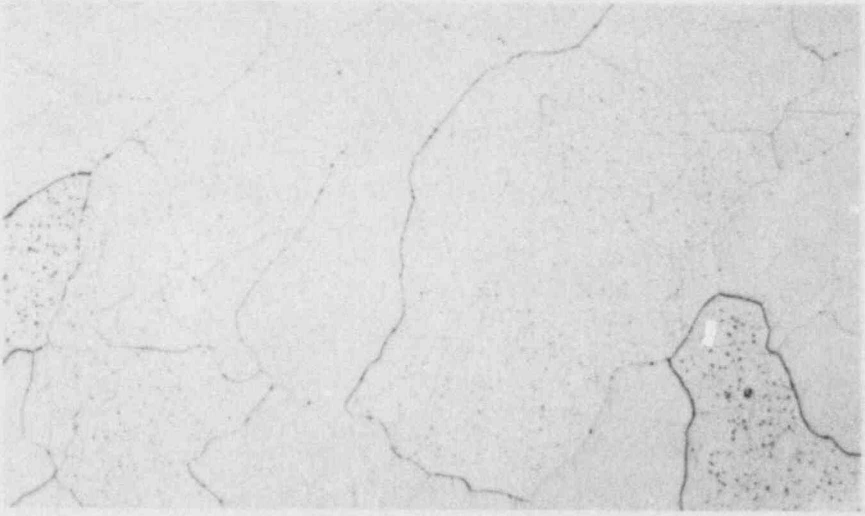

25X Nital Etch 7L382

Figure 3.22. Microstructure of iron ingot in Figure 3.21.

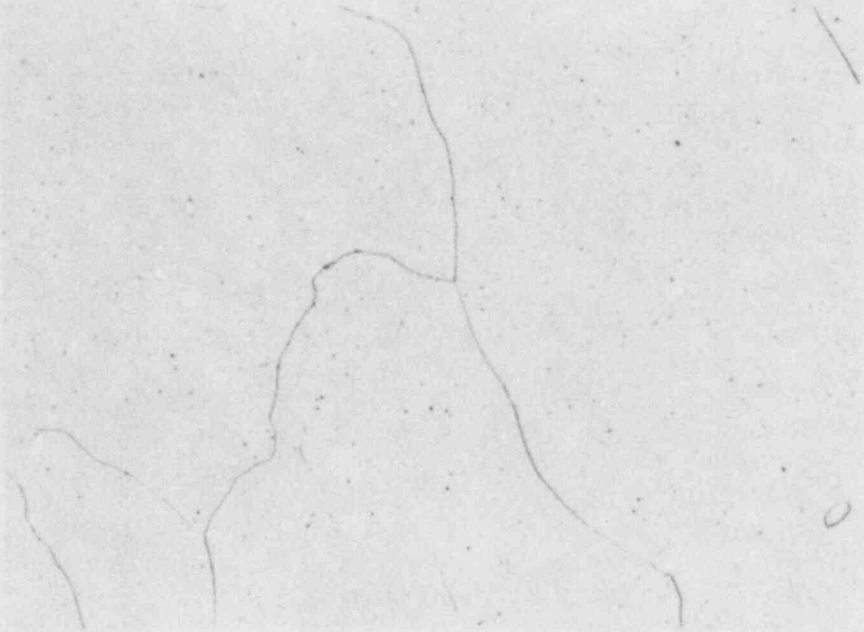

100X Nital Etch 7L368

a. Overall View

1000X Nital Etch 7L373

b. Grain-Boundary Precipitates

Figure 3.23. Photomicrographs of iron ingot showing fine precipitates at grain boundaries and in the matrix.

3.2.2 Tensile Properties of Iron

Tensile specimens oriented longitudinally (tensile axis parallel to the pouring direction or the length of the ingot) and transversely (tensile axis perpendicular to the pouring direction and parallel to the width of the ingot) were tested in hydrogen and nitrogen. The longitudinal specimens had an 0.50-inch-diameter (1.3-cm-diameter) gage section that was 2.0 inches (5.1 cm) long, whereas the transverse specimens had an 0.25-inch-diameter (0.63-cm-diameter) gage section that was 1.0 inch (2.5 cm) long. The tests were conducted at an engineering-strain rate of 10^{-4} sec^{-1}. The gas pressure was 1000 psig (6.9 MPa), and the tests were conducted at room temperature. An indication of the sensitivity of the material to embrittlement was obtained by comparing the tensile properties in those environments. Further information is expected from the fracture-toughness tests to be conducted during the next quarter.

The results of the tensile tests in the two environments are presented in Table 3.7. The results indicate that, as expected based on the previous studies and information in the literature, hydrogen had no effect on the strength properties. Hydrogen did reduce the ductility in both orientations, but to a greater extent in the transverse orientation. The reduction in area was decreased approximately 36 percent in the transverse specimens and approximately 17 percent in the longitudinal specimens. However, it should be noted that the absolute value of the reduction in area was greater for the transverse specimens in both environments. In neither case was the loss of reduction in area so great as to indicate severe hydrogen embrittlement.

3.2.3 Future Work

During the next quarter, J-integral fracture-toughness tests will be conducted with commercially pure iron in hydrogen and in nitrogen to determine the extent to which hydrogen may reduce resistance to cracking. In addition, cast-steel specimens that were shipped recently to Battelle by MSC should be received shortly and will undergo initial characterization and specimen preparation.

3.3 Corrosion Correlations

During this quarter, work continued on the general-corrosion and pitting-corrosion correlations. New boundary conditions accounting for film-growth kinetics were developed for the general-corrosion correlation, and steps were taken to include the effects of an electrically neutral reducing species reacting with the single oxidizing species (nominally O_2) assumed to be present. In the pitting-corrosion task, work continued on using the Weibull distribution to bring the mathematical description of pitting-induction times into accord with experimental data.

Table 3.7. Tensile properties of iron.

Specimen Orientation(a)	Test Environment	Ultimate Tensile Strength (ksi)	Yield Strength (ksi)	Percent Elongation(b)	Reduction in Area (percent)
Longitudinal	1000 psig N_2	30.9	10.8	25.1	21.1
	1000 psig H_2	31.8	10.5	24.9	17.6
Transverse	1000 psig N_2	27.2	9.4	31.3	55.2
	100 psig H_2	27.6	10.0	23.6	35.2

(a) Longitudinal orientation indicates that the specimen axis was oriented parallel to the pouring direction, or the length of the ingot. Transverse orientation indicates that the specimen axis was oriented transverse to the pouring direction, or parallel to the width of the ingot.

(b) Percent elongation was measured in a 2-inch-long gage section for the longitudinal specimens and a 1-inch-long gage section for the transverse specimens, because of differences in specimen length, in accordance with ASTM Standard E8-82, "Standard Methods of Tension Testing of Metallic Materials".

3.3.1 General Corrosion

Separate-effects analyses in the area of general corrosion of waste-package container materials were directed, during the past quarter, toward development of a more physically-realistic description of the mass-transport processes associated with corrosion. Specific tasks included the formulation of boundary conditions describing film growth on the metal surface and extension of the mass-transport model to include additional species.

In earlier reports(3.5,3.6), an elementary mass-transport model for general corrosion was developed in detail. Only one chemical species was considered in that model: a neutral oxidizing species, nominally O_2.

A major simplifying assumption incorporated into the model was that the rate of corrosion was limited by the rate at which the oxidizing species was supplied to the container/groundwater interface by chemical diffusion through the groundwater. This assumption was imposed by means of a boundary condition, namely, that the concentration of the species within the water at the interface is zero.

Relaxation of this assumption requires the imposition of new boundary conditions that account for the kinetics of film growth on the metal surface. These new boundary conditions can be expressed, for this same model, as

$$\frac{dL}{dt} = \frac{D}{nN}\frac{\partial c}{\partial r}(r_o, t) \tag{3.1}$$

and

$$\frac{dL}{dt} = \frac{A(B - 1)}{\exp(2KL) - 1} , \tag{3.2}$$

where L is the film thickness at time t, D is the chemical diffusivity of the oxidizing species in the water, and n and N are, respectively, the volumetric concentration of oxide molecules in the bulk oxide and the number of oxidizing species per oxide molecule. (For example, if the oxidizing species is O_2 and the oxide is FeO, then N = 0.5; or if the oxidizing species is O_2 and the oxide is Fe_3O_4, then N = 2.) In addition, c(r,t) is the concentration of the species in the water at radial position $r > r_o$ (radial cylindrical symmetry is assumed) at time t, with r_o being the container radius. A, B, and K are parameters associated with the film-growth model. Equation 3.1 results from applying Faraday's law to the oxidizing species at the container surface. Equation 3.2 is an expression of the film-growth model that is being assumed here, namely, the point-defect model of Chao, Lin, and Macdonald(3.7).

The parameters A and B in Equation 3.2 are related to the redox potential at the container/groundwater interface which, in turn, is related to $c(r_0,t)$. The parameter K is equal to FE/(RT) where F and R are the Faraday constant and gas constant, respectively, T is the absolute temperature, and E is the electric field within the film (a constant, about 10^6 V/cm).

A natural extension of this simplified model of general corrosion is to introduce a second chemical species, i.e., an electrically neutral reducing species with which the oxidizing species can react chemically. Again assuming radial cylindrical symmetry, the mass transport of the ith species (i = 1, 2 for the two species) can be described in terms of the following partial differential equation:

$$\frac{\partial c_i}{\partial t} = D_i \frac{1}{r} \frac{\partial}{\partial r} \left(r \frac{\partial c_i}{\partial r} \right) + g_i I - a c_1 c_2 - b_i c_i \quad , \tag{3.3}$$

where $c_i(r,t)$ is the concentration of species i in the water, i.e., for $r > r_0$.

The right-hand side of Equation 3.3 is simply a sum of terms that represent different mechanisms which can cause c_i to vary with time. The first term represents chemical diffusion, with D_i being the diffusion coefficient. The second term represents the rate of radiolytic production, with g_i being a "g-value" characteristic of species i, and $I(r,t)$ represents the gamma-field intensity, which is assumed to be given, for $r > r_0$, by

$$I(r,t) = I_0 \left(\frac{r_0}{r} \right) \exp[-\lambda t - \varepsilon (r - r_0)] \quad , \tag{3.4}$$

where I_0 is the intensity at $r = r_0$ and $t = 0$, λ is an average radioactive-decay constant for gamma production, and ε is the linear absorption coefficient. The r^{-1} factor in Equation 3.4 accounts for geometric spreading of the gamma field as r increases.

The third term on the right-hand side of Equation 3.3 represents loss of species i by chemical reaction with the other species, with a being the pertinent rate constant. As expressed in Equation 3.3, the reaction is assumed to be of second order, with species i and j being "lost" in equal amounts when the reaction occurs. Of course, it would be a simple matter to generalize this reaction-rate term to account for other types of reactions, in which case the rate constant, a, would accordingly differ for the two cases, i = 1 and 2, in order to maintain stoichiometry. The fourth term accounts for loss of species i as a result of a pseudo-first-order chemical reaction of that species with another, unspecified species that is assumed to exist in virtually infinite supply.

The boundary conditions which the solution of Equation 3.3 must satisfy are the following, taking species 1 to be the oxidizing species and 2 to be the reducing species:

- $c_1 = c_1^{(o)}$ and $c_2 = c_2^{(o)}$ at $t = 0$, $r > r_o$ (3.5)

  and at $t > 0$, $r \rightarrow \infty$.

- $$\frac{\partial c_2}{\partial r}(r_o,t) = 0 \quad \text{at } t > 0 \quad . \tag{3.6}$$

- $$\frac{dL}{dt} = \frac{D_1}{n_1 N_1} \frac{\partial c_1}{\partial r}(r_o,t) \quad \text{at} > 0 \quad . \tag{3.7}$$

- $$\frac{dL}{dt} = \frac{A(B - 1)}{\exp(2KL) - 1} \; . \tag{3.8}$$

- $$L = 0 \text{ at } t = 0 \quad . \tag{3.9}$$

Equation 3.6 is a statement of the fact that the reducing species does not undergo a chemical reaction at the metal surface. The subscript 1 on n and N in Equation 3.7 denotes that the values of these quantities are associated with species 1.

3.3.2 Pitting Corrosion

In the most recent quarterly report[3.8], the applicability of the Weibull distribution for describing pit-generation kinetics on a metal surface was discussed. Additional research in this area was carried out during the past quarter, and the results are summarized here.

In terms of the Weibull distribution, the pit-generation rate, G(t), at time t is described by the expression

$$G(t) = \frac{mN_\infty}{\tau^m} (t - t_o)^{m-1} \exp\left[-\left(\frac{t - t_o}{\tau}\right)^m\right] \quad , \tag{3.10}$$

which is applicable for $t > t_o$, with $G(t) = 0$ for $t \leq t_o$. Here, N_∞, m, τ, and t_o are certain characteristic parameters. In particular, the instantaneous total number of pits per unit area of metal surface, N(t), is given by

$$N(t) = \int_{t_o}^{t} G(t)dt = N_\infty \left\{ 1 - \exp \left[- \left(\frac{t - t_o}{\tau} \right)^m \right] \right\} \qquad (3.11)$$

so that N_∞ is the total pit concentration on the surface at asymptotically large times. It is noted that effects of overlap of growing pits, which have been discussed elsewhere$^{(3.9)}$, are not considered here.

Let $h(t, t_g)$ be the depth of a pit, at time t, which had been generated at time $t_g \leq t$. We assume here that h exhibits power-law dependence upon time, i.e.,

$$h = a(t - t_g)^b \quad , \qquad (3.12)$$

where a and b are positive parameters, independent of t, t_g, and h. Many types of pit growth have been found to satisfy a relationship of this general type, as has been discussed elsewhere$^{(3.10)}$. Moreover, it was shown$^{(3.11)}$, for this particular growth-rate expression, that the pit-depth distribution function, f(h,t), defined such that f(h,t)dh is the number of pits per unit area of surface, at time t, that have depth between h and h+dh is related to G(t) through the expression

$$f(h,t) = \frac{1}{ab} \; \frac{h}{a}^{\frac{1-b}{b}} G\left(t - \left(\frac{h}{a}\right)^{\frac{1}{b}} \right) \qquad (3.13)$$

for $h < a\,(t - t_o)^b$, assuming that pit generation begins at time t_o (taken as zero in Reference 3.11) and that f(h,t) = 0 for $h > a\,(t - t_o)^b$, where G(t) is an arbitrary pit-generation-rate function. It was assumed, in the derivation of Equation 3.13, that deactivation of growing pits did not occur.

Equations 3.10 and 3.13 can be combined to yield

$$f(h,t) = \frac{mN_\infty}{ab\tau^b} \left(\frac{h}{a\tau^b} \right)^{\frac{1-b}{b}} \left[\frac{t - t_o}{\tau} - \left(\frac{h}{a\tau^b} \right)^{\frac{1}{b}} \right]^{m-1} \qquad (3.14)$$

$$\cdot \exp \left\{ - \left[\frac{t - t_o}{\tau} - \left(\frac{h}{a\tau^b} \right)^{\frac{1}{b}} \right]^m \right\} ,$$

which is valid for $t > t_o$ and $h < a(t - t_o)^b$. Also, $f(h,t) = 0$ for $t < t_o$ and $h > a(t - t_o)^b$.

We now illustrate the application of this analysis to some specific examples. However, rather than choosing values for all the pertinent parameters, it is convenient to first reduce all quantities that appear in the various expressions to dimensionless form. Examination of Equations 3.10, 3.11, and 3.14 shows that natural choices for such quantities are

$$g \equiv \frac{\tau}{mN_\infty} G$$

$$n \equiv \frac{N}{N_\infty}$$

$$T \equiv \frac{t - t_o}{\tau}$$

$$H \equiv \frac{h}{a\tau^b}$$

$$F \equiv \frac{ab\tau^b}{mN_\infty} f$$

in which case Equations 3.10, 3.11, and 3.14, respectively, are reduced to

$$g = T^{m-1} \exp(-T^m) \tag{3.15}$$

$$n = 1 - \exp(-T^m) \tag{3.16}$$

$$F = H^{\frac{1-b}{b}} \left(T - H^{\frac{1}{b}}\right)^{m-1} \exp\left[-\left(T - H^{\frac{1}{b}}\right)^m\right] \tag{3.17}$$

with Equation 3.17 being valid within the range $T > 0$ and $H < T^b$, and with $F = 0$ for $T < 0$ and $H > T^b$. The only input parameters that are now needed, in Equations 3.15 to 3.17, are m and b.

Some specific numerical examples were selected which serve to illustrate these results. First, the value $b = 0.5$ was selected for all the examples, since this corresponds closely to the vaue of 0.49 reported by Marsh(3.12) for carbon-steel nuclear-waste containers. Using this value of b, Equations 3.15 and 3.16 are plotted in Figures 3.24a and 3.24b, respectively, for m = 2, 3, and 4. Moreover, the pit-depth distribution at selected times is plotted, for these three examples, in Figures 3.25 to 3.27 using Equation 3.17.

The effect of increasing the value of m is seen, in Figure 3.24a, to reduce the pit-generation rate at short and long times; that is, to essentially shorten the duration over which most of the pits are generated. This behavior is also reflected in Figure 3.24b, which shows that the total pit concentration approaches its saturation level more quickly as m is increased.

The "spreading" of the pit-depth distribution with increasing time is illustrated for these cases in Figures 3.25 to 3.27. Although some differences in properties of the distribution function, at the same given value of T, are seen to exist for the different values of m, gross features of the general shape are similar in all three cases.

3.3.3 Future Work

During the next quarter, the new boundary conditions, Equations 3.1 and 3.2, will be incorporated into the simplified general-corrosion model developed earlier. Of particular interest will be an assessment of the effects of radiolysis on the instantaneous film thickness, L(t).

Solution of the above problem will also be undertaken during the next quarter. Toward this end, as much normalization of the variables as possible will be carried out in order to minimize the amount of data required as input.

The mass-transport problems solved earlier, as well as those outlined above, are all based on the assumption of an isothermal medium. It would also be possible to generalize these problems to cases in which the temperature varies with both r and t. Equation 3.3 would require appropriate modification, and the temperature dependence of the various input parameters would have to be incorporated into the formulation. Heat conduction can be regarded as simply another type of transport process; indeed, initial computations of time-dependent temperature profiles have already been carried out.(3.5)

In continuing studies of pitting corrosion, attention will be redirected to the pit-growth model developed earlier(3.10). Possible generalizations of this model will be considered and correlations with pit-growth data obtained at Battelle will be made.

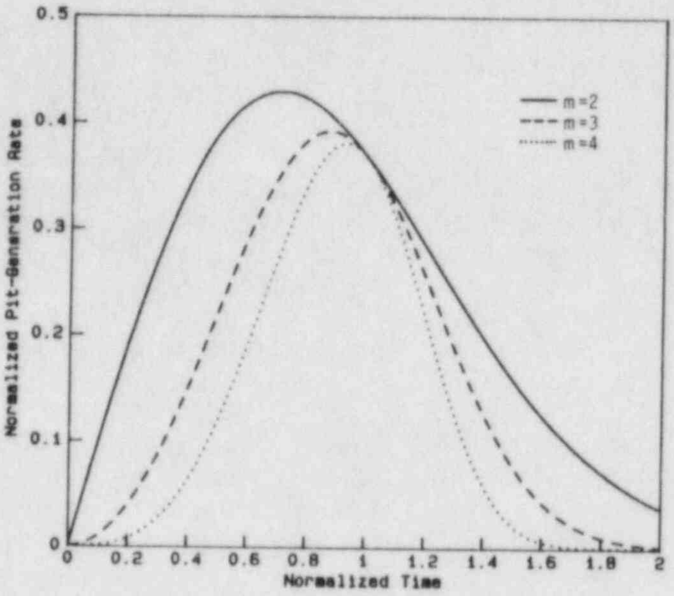

(a) g vs. T, after Equation 3.15

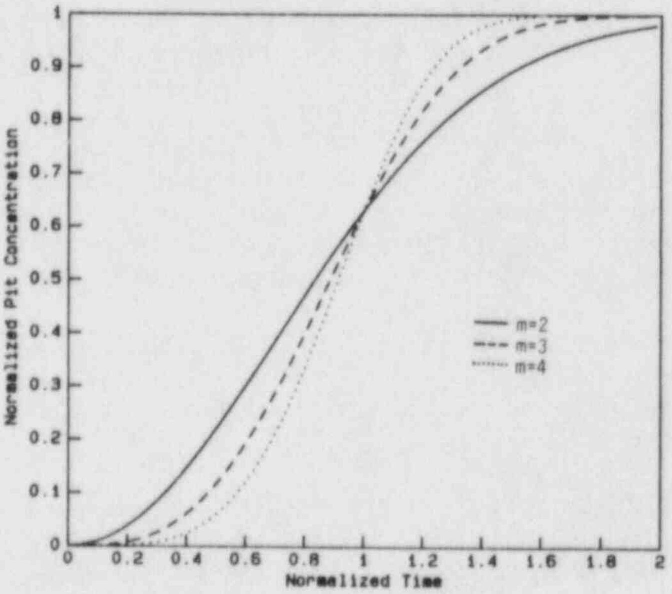

(b) n vs. T, after Equation 3.16

Figure 3.24. Variation of pit-generation rate and pit concentration with time, as calculated by the pitting-corrosion model.

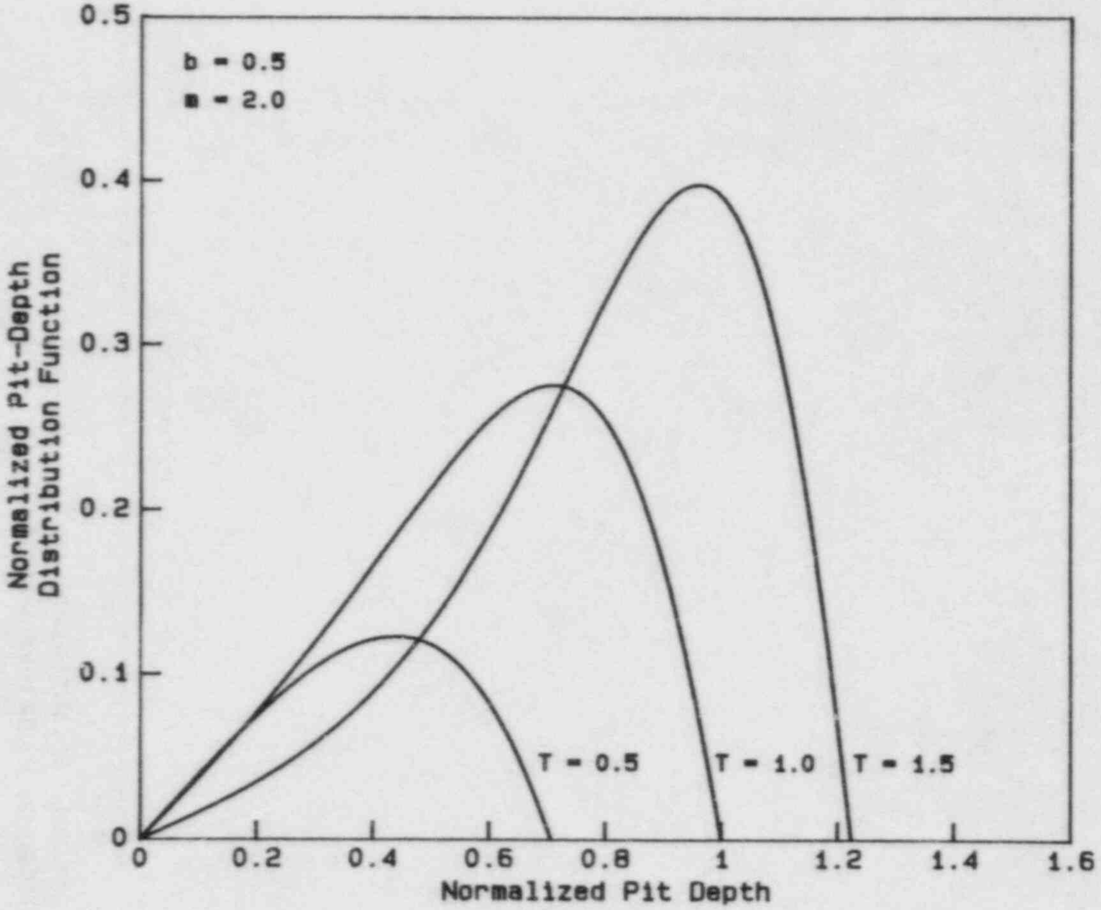

Figure 3.25. Calculated pit-depth distributions (F vs. H, after Equation 3.17) for m = 2 and selected values of T.

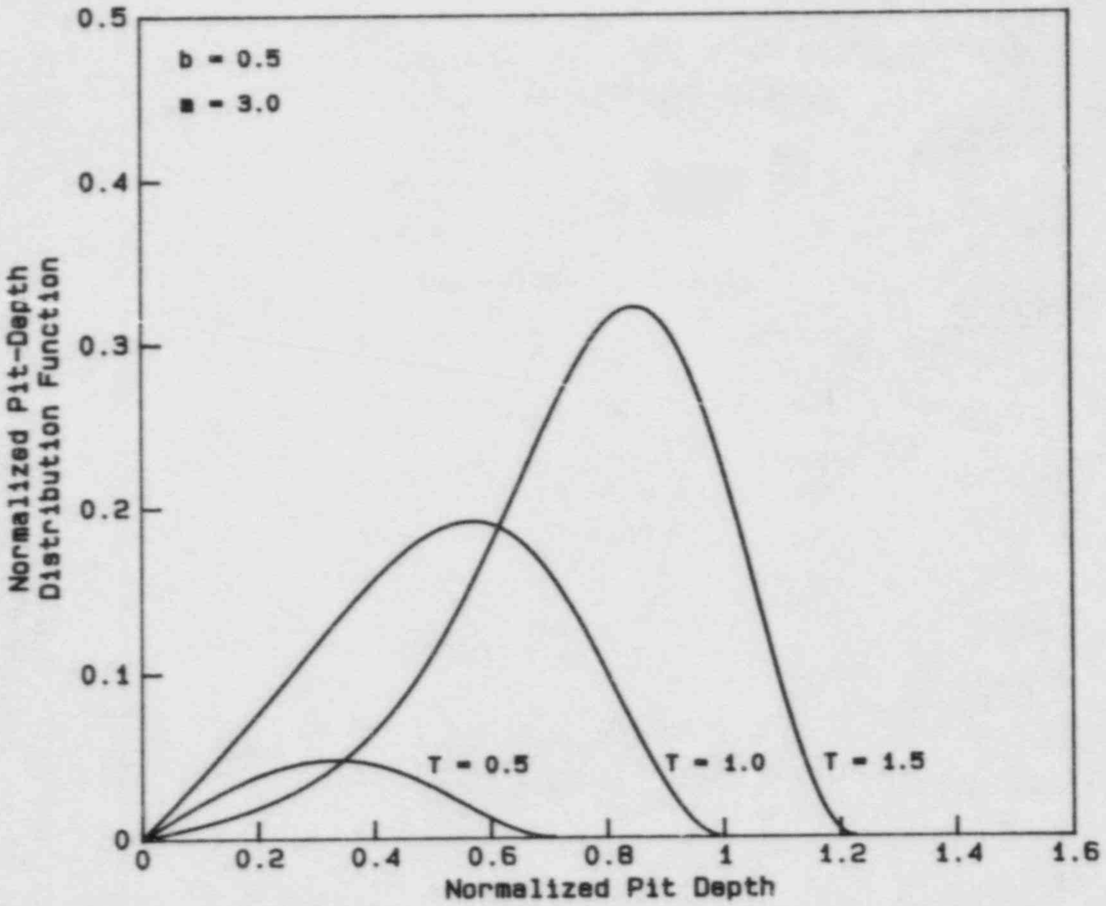

Figure 3.26. Calculated pit-depth distributions (F vs. H, after Equation 3.17) for m = 3 and selected values of T.

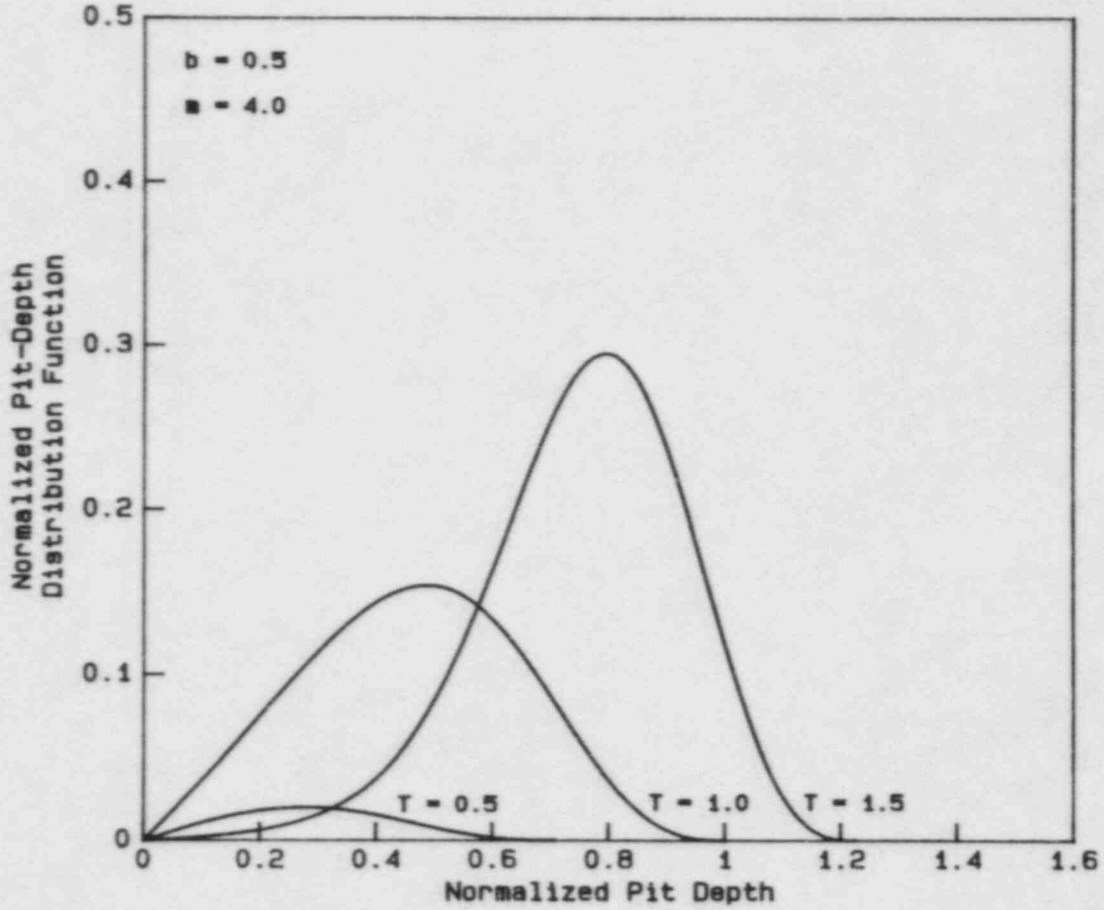

Figure 3.27. Calculated pit-depth distributions (F vs. H, after Equation 3.17) for m = 4 and selected values of T.

3.4 References for Section 3

(3.1) T. E. Jones, "Reference Material Chemistry--Synthetic Groundwater Formulation", RHO-BW-ST-37P (1982).

(3.2) "Long-Term Performance of Materials Used for High-Level Waste Packaging", D. Stahl and N. E. Miller (Compilers), NUREG/CR-3427, Vol. 4, BMI-2113 (June 1984), p. 3-67.

(3.3) M. B. Strauss and M. C. Bloom, "Cracking of Low Carbon Steel by Ferric Chloride Solutions", Corrosion, 16 (11), 553t.

(3.4) "Long-Term Performance of Materials Used for High-Level Waste Packaging", D. Stahl and N. E. Miller (Compilers), NUREG/CR-3427, Vol. 4, BMI-2113 (June 1984), pp. 3-87 and 3-88.

(3.5) "Long-Term Performance of Materials Used for High-Level Waste Packaging", D. Stahl and N. E. Miller (Compilers), NUREG/CR-3427, Vol. 4, BMI-2113 (June 1984), pp. 3-106 ff.

(3.6) "Long-Term Performance of Materials Used for High-Level Waste Packaging", D. Stahl and N. E. Miller (Compilers), NUREG/CR-3900, Vol. 1 (September 1984), pp. 3-30 ff.

(3.7) C. Y. Chao, L. F. Lin, and D. D. Macdonald, J. Electrochem Soc. 128 (1981) 1187.

(3.8) "Long-Term Performance of Materials Used for High-Level Waste Packaging", D. Stahl and N. E. Miller (Compilers), NUREG/CR-3900, Vol. 1 (September 1984), pp. 3-34 ff.

(3.9) "Long-Term Performance of Materials Used for High-Level Waste Packaging", D. Stahl and N. E. Miller (Compilers), NUREG/CR-3405, Vol. 1, BMI-2105 (July 1983), pp. 6-18 ff.

(3.10) "Long-Term Performance of Materials Used for High-Level Waste Packaging", D. Stahl and N. E. Miller (Compilers), NUREG/CR-3427, Vol. 4, BMI-2113 (June 1984), pp. 3-124 ff.

(3.11) "Long-Term Performance of Materials Used for High-Level Waste Packaging", D. Stahl and N. E. Miller (Compilers), NUREG/CR-3427, Vol. 4, BMI-2113 (June 1983), pp 3-132 ff.

(3.12) G. P. Marsh, Trans. Am. Nucl. Soc., 45 (1983) 292.

4. INTEGRATED SYSTEM PERFORMANCE

One purpose of the system-performance task is to obtain a better understanding of the phenomena which affect the long-term performance of waste packages at the system level. Knowledge gained in these studies will aid in assessing the adequacy of system-performance models for nuclear waste packages.

During this past quarter, emphasis has been placed on water-chemistry studies, groundwater-radiolysis studies, and integral experiments.

The water-chemistry studies will improve our understanding of the local water chemistry in the vicinity of the waste package by providing information on how the corrosion of the metallic barriers and leaching or dissolution of the waste form alter the local water chemistry, and how these phenomena are, in turn, affected by the local water chemistry. The water-chemistry studies will also provide information on the chemical speciation of radionuclides released from the waste form. This information will be useful in assessing the transport rate of these radionuclides through the waste package.

The groundwater-radiolysis studies will provide information on the concentrations of the radiolytic species in the vicinity of the waste package. These species can affect the corrosion of the metallic barriers as well as the chemical speciation of the radionuclides released from the waste form, thus affecting both the containment time of the waste package and the release rate of radionuclides from the waste package to the repository.

The integral experiments are being assembled to provide information on combined-effects processes which are important in determining the long-term performance of nuclear waste packages. To the extent possible, these experiments will simulate the environment which a waste package and its components will see during their lifetime. These experiments will also provide some information on the rates of releases and cumulative releases of radionuclides from high-level-waste glass and spent-fuel waste forms for a variety of simulated waste-package failures.

4.1 Water Chemistry

The study of water chemistry is an important part of any theoretical treatment of waste-package performance. It is generally considered that water is the only credible medium for transport of radionuclides away from the repository. In addition, the composition of groundwater and its presence or absence are major factors in determining the modes and rates of degradation for all components of the waste package. Since water is both a transport medium and a participant in many degradation mechanisms, it plays an important role in coupling many processes. It is therefore desirable to build a model of water chemistry that can interface easily with descriptions of a variety of other phenomena. Our work has been directed at producing such a model. It has not been our intention to produce a highly detailed water-chemistry code, but rather to investigate the interactions between various phenomena by using a small water-chemistry code as a tool.

Our work to date has used two water-chemistry programs: a Battelle-developed water-chemistry code(4.1), which handles a small number of species, and WATEQ(4.2), which handles a significantly larger set of species. WATEQ was intended for analyzing field data rather than for modeling, and it was not feasible to adapt WATEQ for modeling. On the other hand, when we used our water-chemistry code we were concerned that neglecting so many species would impair the accuracy of our work. Therefore, our usual procedure has been to use the small model for most of our calculations and, where possible, to check selected results against output from WATEQ. As noted in a previous report(4.3), values of pH calculated by our code and by WATEQ were in excellent agreement with each other and with experimental data.

At the beginning of this quarter, we wanted to enlarge the set of species used in our water-chemistry program by including aluminum, potassium, and fluorine and by strengthening our treatment of iron. This has been accomplished by making appropriate modifications to the program and incorporating thermodynamic data from the WATEQ data base. A total of 34 species is now treated. In addition, treatment of the carbonate-bicarbonate system has been improved.

The new version has been coded, and testing is nearly complete. The new version has not been heavily used yet; however, preliminary comparisons of results from the two versions indicate that the old version underestimated the buffering effect of the carbonate-bicarbonate reaction. This may reduce the pH calculated for a repository environment. While the magnitude of the error has not been determined, the inaccuracies of the previous version are conservative--that is, the higher pH predicted by the earlier version would be expected to correspond to rates of waste-form dissolution that are too high. This subject will be addressed in the coming quarter.

During testing of the new version of the water-chemistry code, checking of some unexpected results revealed an error in our copy of WATEQ. The problem is relatively severe: the total concentration of carbonate species is not constant. Besides creating an obvious conflict with the law of conservation of mass, the error can cause a very large difference between the pH calculated by WATEQ and that calculated by our water-chemistry programs. Some modifications had been made to WATEQ on this project when the program was moved from one computer to another. However, these modifications were not at fault since the older version of WATEQ was found to show similar behavior. The exact cause of the error has not been determined.

In light of the known error in this version of WATEQ, it is inappropriate to use this program for checking the results of other programs.

Since we would like to have a large water-chemistry program available, there appear to be two alternatives. First, we could attempt to modify our version of WATEQ. Although some effort has been made in this direction, the version of WATEQ that we now have is difficult to modify, and there is always the possibility of introducing new errors while correcting old ones. Second, we could obtain a newer version of WATEQ, since the error is so severe that it is likely to have been discovered and corrected in later versions. The second alternative appears to be more promising, so we do not plan to attempt further changes in our copy of WATEQ unless newer versions also prove to be in error.

Further expansion of our water-chemistry code is not planned for the near future. Testing of this program will be completed and the new version of the program will be integrated into our model for glass dissolution.

4.2 Groundwater Radiolysis

Radiolysis of groundwater in the vicinity of the waste package can alter the local water chemistry, thus affecting the long-term performance of waste packages. Effects on the local water chemistry can include changes in pH and oxygen potential, as well as the production of species which may have a deleterious effect on the waste-package materials. As reported previously, other investigators have observed that gamma radiation may have adverse effects on the time-to-failure performance measure for metal components which are exposed to water.(4.4)

One objective of these studies is to develop a generalized model for analyzing the radiolysis of groundwater alone and of groundwater whose composition has been altered by the presence of other materials such as packing and corrosion products. This model will provide information on the expected concentrations of radiolysis products in the vicinity of the metallic components of the waste package. This information is required by the canister-materials task of the program. The model will also provide a means of assessing the abbreviated groundwater-radiolysis model which is part of the general-corrosion model described in Section 3.3.1. The model will also provide a vehicle for determining effective rate constants for reactions included in the water-radiolysis component of the corrosion model.

The first step in these studies has been to describe the radiolysis of pure water that might contain hydrogen and/or oxygen. This description accounts for anions and cations which may be present in significant amounts in groundwaters of interest. As the description of groundwater radiolysis is developed, it is being benchmarked against experimental data available in the literature. As part of this effort, gamma-energy deposition calculations were performed to determine energy-deposition rates to the groundwater and the materials surrounding spent-fuel and commercial high-level waste packages. Results of these energy-deposition calculations have been reported previously.(4.4) Several mechanisms for the radiolysis of water were evaluated for their ability to predict the behavior of water-radiolysis experiments described in the literature. Of these, the mechanism presented by Rosinger and Dixon(4.5) was chosen as the basis for our generalized description of groundwater radiolysis.

Work during this quarter has addressed the precipitation of ferric species in groundwaters which contain iron. As part of this effort, comparisons have been made of predicted and measured concentrations of hydronium ions and ferric ions as a function of time for an aqueous iron sulfate system exposed to gamma radiation. Simulations were also performed for pure water of pH 7 and pH 4.5, with and without the presence of dissolved hydrogen and oxygen, and for aqueous systems containing varying amounts of ferrous and ferric ions with and without the presence of dissolved hydrogen and oxygen. These preliminary calculations show that many factors can influence observed radiolytic yields.

4.2.1 Radiolysis of Groundwaters Containing Iron

A mechanism for the radiolysis of groundwaters containing iron has been developed as an extension of the Rosinger and Dixon mechanism(4.5) for the radiolysis of water. Reasons for choosing this mechanism as the basis for our generalized water radiolysis model are described in a previous annual report.(4.4)

In Section 4.2.1.1, the development of a mechanism for the radiolysis of groundwaters containing iron is described, and benchmark calculations are compared with experimental data. In Section 4.2.1.2, results of preliminary calculations for various aqueous systems are shown using a dose rate associated with the dose rate to water at the surface of the waste-package overpack at about 100 years after placement. Calculations of gamma-energy deposition rates to materials in and near waste packages were described previously(4.4,4.6,4.7) for spent-fuel and commercial high-level waste packages.

4.2.1.1 Model Development

Last quarter, a preliminary mechanism for the radiolysis of water containing ferrous and ferric ion was developed. This mechanism,(4.8) benchmarked against data of Mathews,(4.9) was found to give qualitatively good results for the time-dependence of the hydronium-ion and ferric-species concentrations. Although the predicted pH was within one unit of the experimental value, predictions of the long-term trend for the hydrogen-ion concentration needed improvement. This quarter, the long-term prediction of the hydrogen-ion concentration has been improved with the inclusion of an approximate mechanism for the precipitation of hydrolyzed ferric species. Other improvements were made to reflect kinetic information in the literature.

The mechanism developed last quarter(4.8) included, among other reactions, several reactions for the oxidation and reduction of ferrous and ferric ions in aqueous solution. Of these reactions, the reaction for the oxidation of ferrous ions by hydroxyl radicals is not consistent with experimental investigations. Stuglik and Zagorski(4.10) were unable to fit their data with the charge-transfer reaction

$$Fe^{2+} + OH \rightarrow Fe^{3+} + OH^- \quad ,$$

which is also used by other investigators in their radiolysis mechanisms.(4.11) Instead, Stuglik and Zagorski explain their data with a hydrogen abstraction mechanism

$$Fe^{2+} + OH \xrightarrow{Fe^{2+} + OH(H_2O)_5} FeOH^{2+} \qquad k = 3.2 \times 10^{8} \text{ liter-mol}^{-1}\text{-s}^{-1}$$

$$FeOH^{2+} + H^{+} \longrightarrow Fe^{3+} + H_2O \qquad k = 1.5 \times 10^{9} \text{ liter-mol}^{-1}\text{-s}^{-1}$$

for the reaction of ferrous ion with hydroxyl radicals. In our mechanism, the single-step charge-transfer reaction for the oxidation of ferrous ions by hydronium radicals has been replaced by the hydrogen abstraction reactions described above. Comparable adjustments to the mechanism for the oxidation of aqueous Fe^+ species by hydroxyl radicals has also been made. The rate constants for these reactions

$$Fe^{+} + OH \xrightarrow{Fe^{+} + OH(H_2O)_5} FeOH^{+} \qquad k = 2.8 \times 10^{8} \text{ liter-mol}^{-1}\text{-s}^{-1}$$

$$FeOH^{+} + H^{+} \longrightarrow Fe^{2+} + H_2O \qquad k = 1.3 \times 10^{9} \text{ liter-mol}^{-1}\text{-s}^{-1}$$

have been estimated by the procedure described in the last quarterly report,(4.8) where the rate constants are assumed to vary inversely with radii. These changes did not have a large effect on the model predictions of the simulation of Mathews' experiment.

This quarter, the radiolysis model was extended by the addition of a reaction which accounts for the precipitation of hydrolyzed ferric ions. The precipitation of ferric species proceeds through several steps which are not completely understood.(4.12-4.18) It is believed that large complexes form first, then colloids form, and finally amorphous and crystalline materials precipitate. This process is also often associated with a change in pH; however, the relation between precipitation and pH is complex.(4.12-4.17) Since the kinetics for this process is not well understood, the process has been approximated with the reaction

$$Fe(OH)_2^{+} + Fe(OH)_2^{+} \longrightarrow FeOOH + FeOH^{2+} + H_2O \quad ,$$

where FeOOH is precipitated from solution. In this model, FeOCH actually represents a range of ferric species. The effective rate constant for this reaction has been estimated by varying the rate constant, as shown in Figure 4.1, and choosing a value which gives reasonable agreement with the data. As can be seen in Figure 4.1, a value of 500 liter/m/sec gives reasonable agreement for the time-dependence of the hydrogen-ion concentration.

As discussed in the last quarterly report,(4.8) the ferric-ion concentrations predicted by the radiolysis model cannot be directly related to the ferric-ion concentrations reported by Mathews(4.9) because he used an "effective" extinction coefficient to determine concentrations and because extinction coefficients are not known for all of the species described by the model. Some information can be gained, however, by examining available data, such as those shown in Figure 4.2. This figure shows the solution absorbance, backcalculated from Mathews' data as described in the previous quarterly report,(4.8) assuming a 1-cm cell. Also shown is the calculated absorbance for the mechanism reported last quarter, using 120 and 1900 for the extinction coefficients of Fe^{3+} and $FeOH^{2+}$,(4.19) respectively. Extinction coefficients were not available for other species modeled. Figure 4.2 shows that for the model which does not include precipitation, the concentrations of absorbing species rise too rapidly at early times but level out to reasonably close values at longer times. The calculated absorbance may be higher if the other species modeled have significant extinction coefficients. Since the calculated absorbance at longer times is not higher than that backcalculated from the data, qualitative agreement with the data is possible. Figure 4.2 also shows calculated absorbances for the model with precipitation added for several values assigned to the rate constant of the precipitation reaction. The rate of increase of solution absorbance is between that of the experimental data and the model reported last quarter. At longer times, the calculated absorbance drops to low values, below those calculated from the data. Low absorbance does not necessarily indicate a failure to predict the data, because not all of the species-extinction coefficients are known and because the FeOOH species actually represents a range of species, some with a significant extinction coefficient, such as $(FeOH)_2^{4+}$(4.13).

4.2.1.2 Simulations of the Radiolysis of Aqueous Systems

A preliminary version of the radiolysis model has been used to simulate the radiolysis of a variety of aqueous systems. The gamma-radiation field used in these calculations was 10^{15} eV/liter/sec, which is equivalent to about 60 R/hr. This value of the energy-deposition rate was chosen because it is representative of the dose rate to groundwater at the surface of the waste-package overpack after about 100 years. Calculations of these dose rates have been reported previously.(4.4,4.6,4.7)

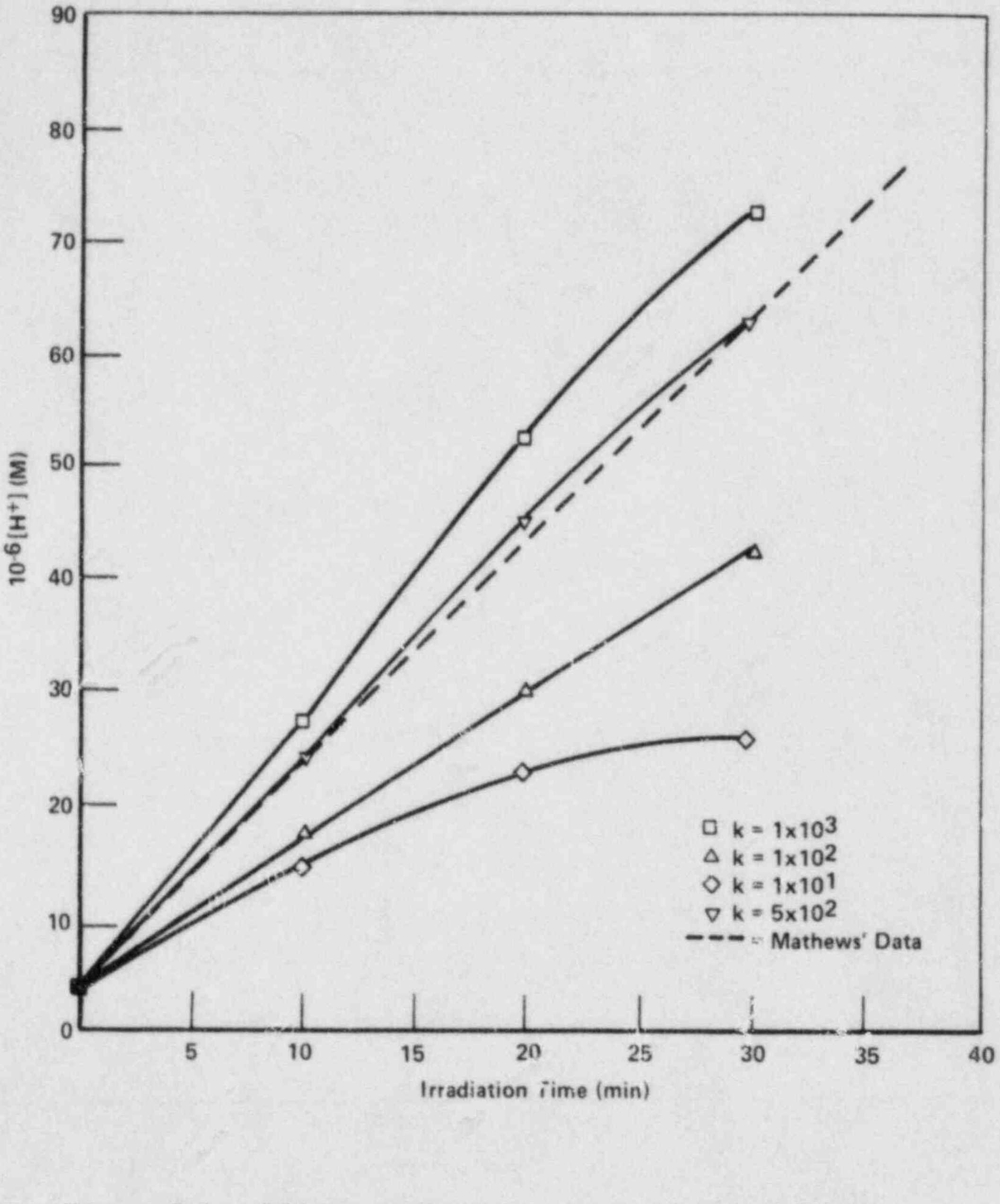

Figure 4.1. Effect of the rate constant of the ferric precipitation reaction on the calculated time-dependence of the hydronium-ion concentration compared with Mathews' data.(4.9)

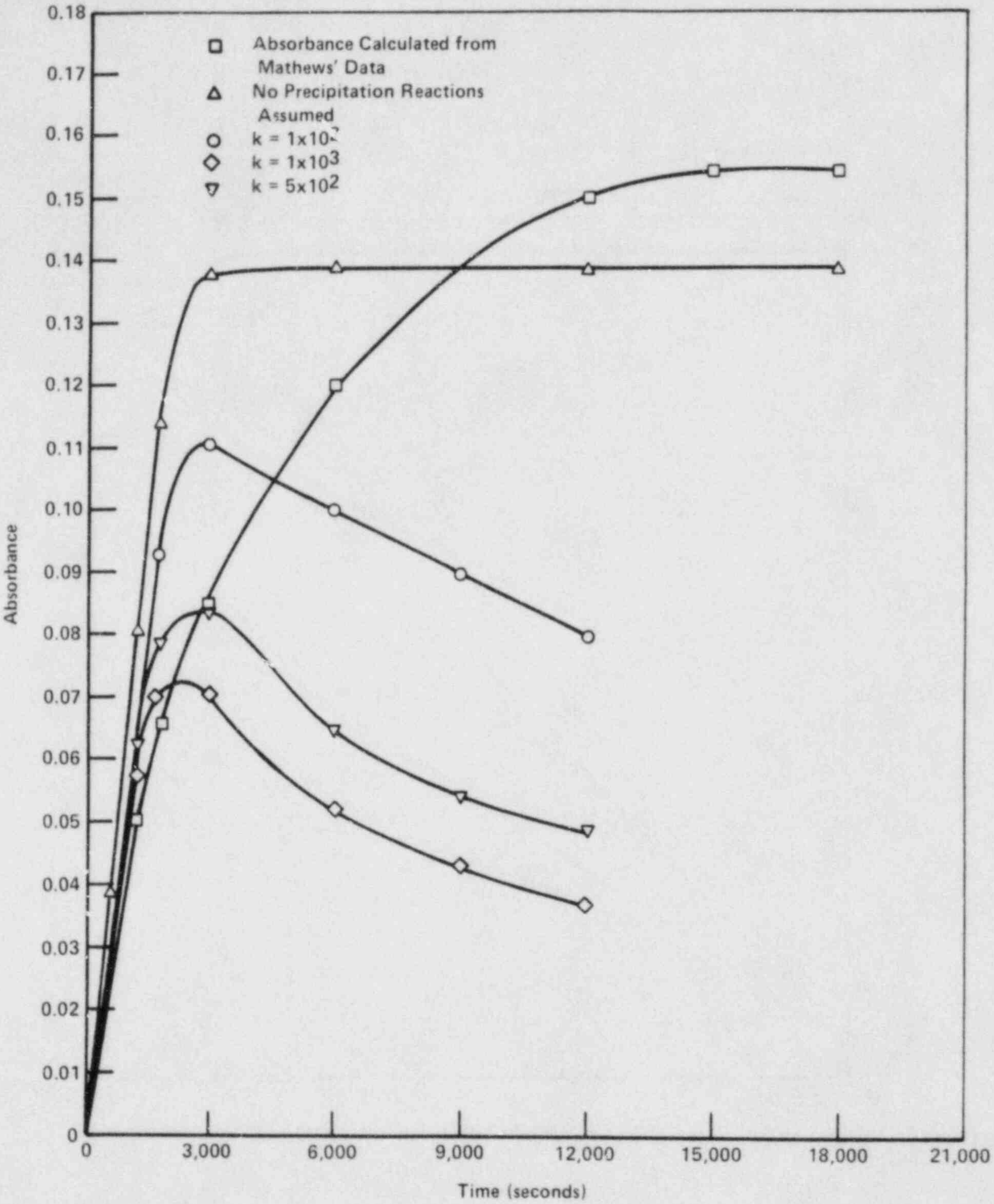

Figure 4.2. Comparison of the absorbance calculated using two species with the absorbance backcalculated from Mathews' data.(4.9)

Radiolysis simulations have been performed for aqueous systems with and without the presence of dissolved gases. For aqueous systems initially free of dissolved gases, simulations were performed for pure water of pH 7.0 and pH 4.5 and for solutions of pH 4.5 containing varying amounts of ferrous and ferric ions. The concentrations for the aqueous systems are expressed as initial concentrations except for one case, where the concentration of ferrous ion was held constant. For aqueous systems containing dissolved gases, simulations were performed for solutions containing varying amounts of hydrogen, oxygen, ferrous ions, and ferric ions. All calculations for solutions containing dissolved gases were performed for an initial pH of 4.5, and all the stated concentrations are initial concentrations.

Figure 4.3 shows a comparison of the calculated dissolved-hydrogen concentration for several solutions which are initially free of dissolved gases. As can be seen in this figure, the existing model shows that iron-free solutions of pH 7 and pH 4.5 behave similarly with respect to the dissolved-hydrogen concentrations. As can be seen in Table 4.1, the time-dependence of the dissolved oxygen concentrations is also similar for these two solutions at early times. Figure 4.3 also shows that when the solution contains an initial concentration of 10^{-5} mole/liter ferrous ion at a pH of 4.5, the calculated hydrogen concentration as a function of time is about 10-100 times higher for the period shown. Data in Table 4.1 also show that for this time period, most of the ferrous ion initially present is converted to other species (mostly ferric ion). Figure 4.3 also shows that when the ferrous concentration is held constant, the calculated long-term hydrogen concentrations are about 100 times higher than for iron-free water. Such an effect may be relevant to aqueous systems in the vicinity of waste packages because the surrounding materials may replenish species removed from the aqueous system as a result of reactions associated with radiolysis or corrosion.

Figure 4.4 shows some effects of ferrous- and ferric-ion concentrations on the calculated time-dependence of the hydrogen concentration. It can be seen in this figure that as the initial concentration of the ferrous ion is increased from 10^{-7} mole/liter to 10^{-4} mole/liter, there is a significant change in the rate of increase of hydrogen concentration. When the concentration of ferrous ion is increased still further, however, from 10^{-4} mole/liter to 10^{-2} mole/liter, there is a decrease in the concentration of dissolved hydrogen with time for the period shown. The figure also shows that when equal amounts of ferrous and ferric ions are initially present at a concentration of 10^{-4} mole/liter, the calculated hydrogen concentrations are somewhat less than when the solution contains only ferrous ion at this concentration. Data indicate(4.20,4.21) that iron concentrations from 10^{-4} mole/liter to 10^{-2} mole/liter might be expected in a basalt repository.

Simulations were also performed for aqueous systems containing dissolved hydrogen and oxygen. For these calculations, a dissolved-oxygen concentration of 6×10^{-5} mole/liter chosen as a midrange value for

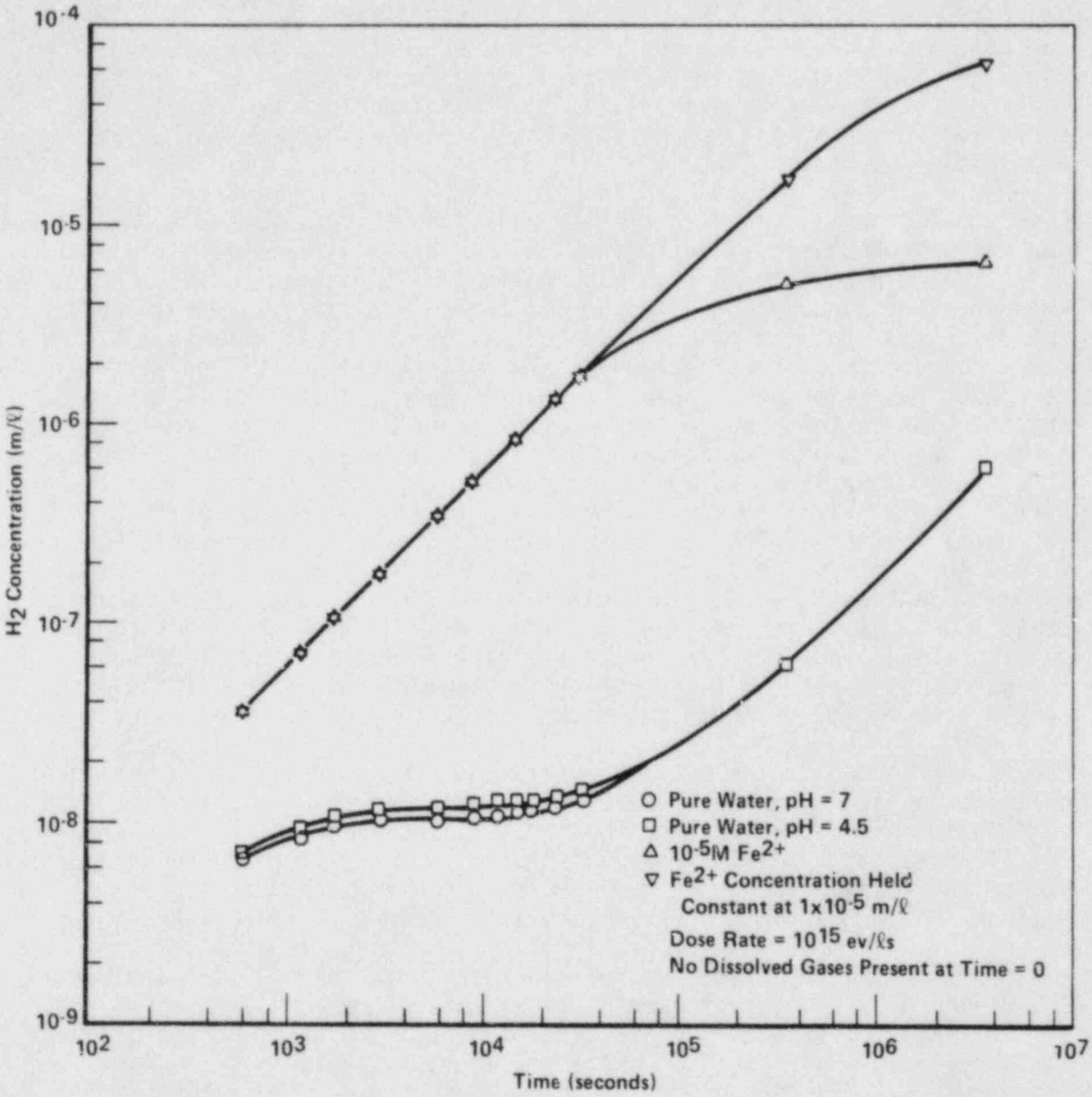

Figure 4.3. H_2 concentration as a function of time for solutions which are initially free of dissolved gases.

Table 4.1. Calculated concentrations of dissolved hydrogen and oxygen species in water solutions with and without iron.

Time (sec)	O_2 mol/l	H_2O_2 mol/l	H^+ mol/l	Fe^{2+} mol/l	Solution
3.0E3	2.1E-11	9.5E-9	1.0E-7	NA*	Water, pH 7, no dissolved gases at time = 0
1.8E4	1.4E-11	8.5E-9	1.0E-7	NA	
3.6E5	3.0E-13	3.0E-9	1.0E-7	NA	
3.0E3	2.1E-11	1.1E-8	3.2E-5	NA	Water, pH 4.5, no dissolved gases at time = 0
1.8E4	1.5E-11	9.9E-9	3.2E-5	NA	
3.6E5	9.7E-15	2.5E-9	3.2E-5	NA	
3.0E3	7.9E-16	1.3E-8	3.2E-5	9.7E-6	10^{-5} m/l Fe^{2+} at time = 0, pH 4.5, no dissolved gases at time = 0
1.8E4	4.5E-15	1.5E-8	3.3E-5	8.0E-6	
3.6E5	9.6E-15	3.3E-9	5.0E-5	1.4E-7	
3.0E3	7.9E-16	1.3E-8	3.2E-5	1.0E-5	Fe^{2+} concentration held constant at 10^{-5} mol/l, pH 4.5, no dissolved gases at time = 0
1.8E4	4.4E-15	1.4E-8	3.3E-5	1.0E-5	
3.6E5	4.9E-14	1.5E-8	8.8E-5	1.0E-5	

Gamma Dose Rate = 10^{15} eV/liter·sec (~ 60 R/hr).

*NA = not applicable.

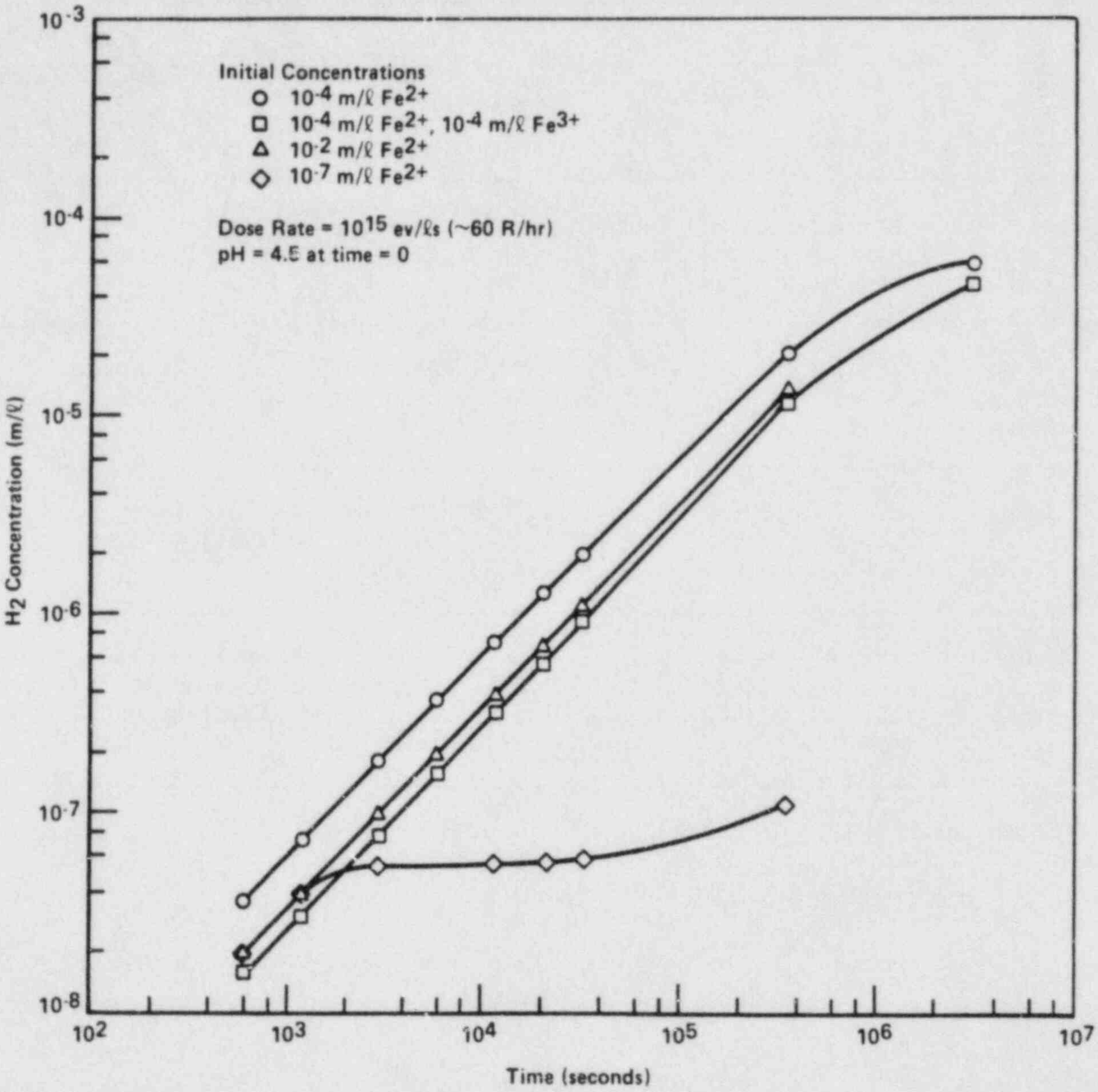

Figure 4.4. Effect of iron concentration on the time-dependence of the dissolved-hydrogen concentration.

measurements of the oxygen concentration for a simulation of a waste-package environment(4.21). An initial ferrous-ion concentration of 10^{-5} mole/liter was chosen for comparison with Figure 4.3 and Table 4.1. Two values of the initial dissolved-hydrogen concentration were chosen. The lower value was based on an expected amount in equilibrium with air at one atmosphere at 25 C. This value of 4×10^{-10} mole/liter was calculated using a Bunsen absorption coefficient of 0.0175 for hydrogen in water(4.22) and a hydrogen partial pressure of 5×10^{-7} atm calculated assuming a standard dry atmosphere.(4.23) The upper value of 2×10^{-5} mole/liter was chosen based on LWR experience as the concentration which suppresses hydrogen generation by water radiolysis for non-boiling systems at 25 C.(4.24) The initial ferrous-ion concentration was set at 10^{-5} mole/liter. The calculated time-dependence of the hydrogen concentration for these two sets of reactions is shown in Figure 4.5. In this figure, it can be seen that the hydrogen concentration increases with time when the initial hydrogen concentration is low and decreases with time when the initial hydrogen concentration is high. Other results of these calculations, which are tabulated in Table 4.2, show that some dissolved oxygen is consumed in both cases. This table also shows that in both cases, ferrous ion is effectively converted to other forms (mostly ferric species). Radiolysis can thus affect the water chemistry in the vicinity of waste packages.

4.2.2 Conclusions

A preliminary mechanism for the radiolysis of groundwaters containing dissolved hydrogen, oxygen, ferrous ions, and ferric ions has been developed. This mechanism has undergone some benchmark tests against experimental data reported in the literature. This mechanism has been used to perform some simulations of the gamma radiolysis of several aqueous systems exposed to a gamma dose rate equivalent to that at the surface of a spent-fuel or high-level waste-package overpack about 100 years after placement. These calculations show that the generation of radiolytic hydrogen is sensitive to the ferrous-ion concentration in a nonlinear manner. These calculations also show that dissolved oxygen can be radiolytically generated or consumed, depending on the composition and conditions of the system. In all of these simulations, ferrous ion, when present, was effectively oxidized to ferric species. This may have implications for the characterization of the local water chemistry when evaluating the performance of waste-package materials.

4.2.3 Future Work

In the near term, additional species will be added to the radiolysis mechanism. Priority will be given to those species which are generic to several groundwaters and which are associated with corrosion products and packing material for waste packages. Additional groundwater simulations will be performed to examine effects of other variables on the radiolysis process.

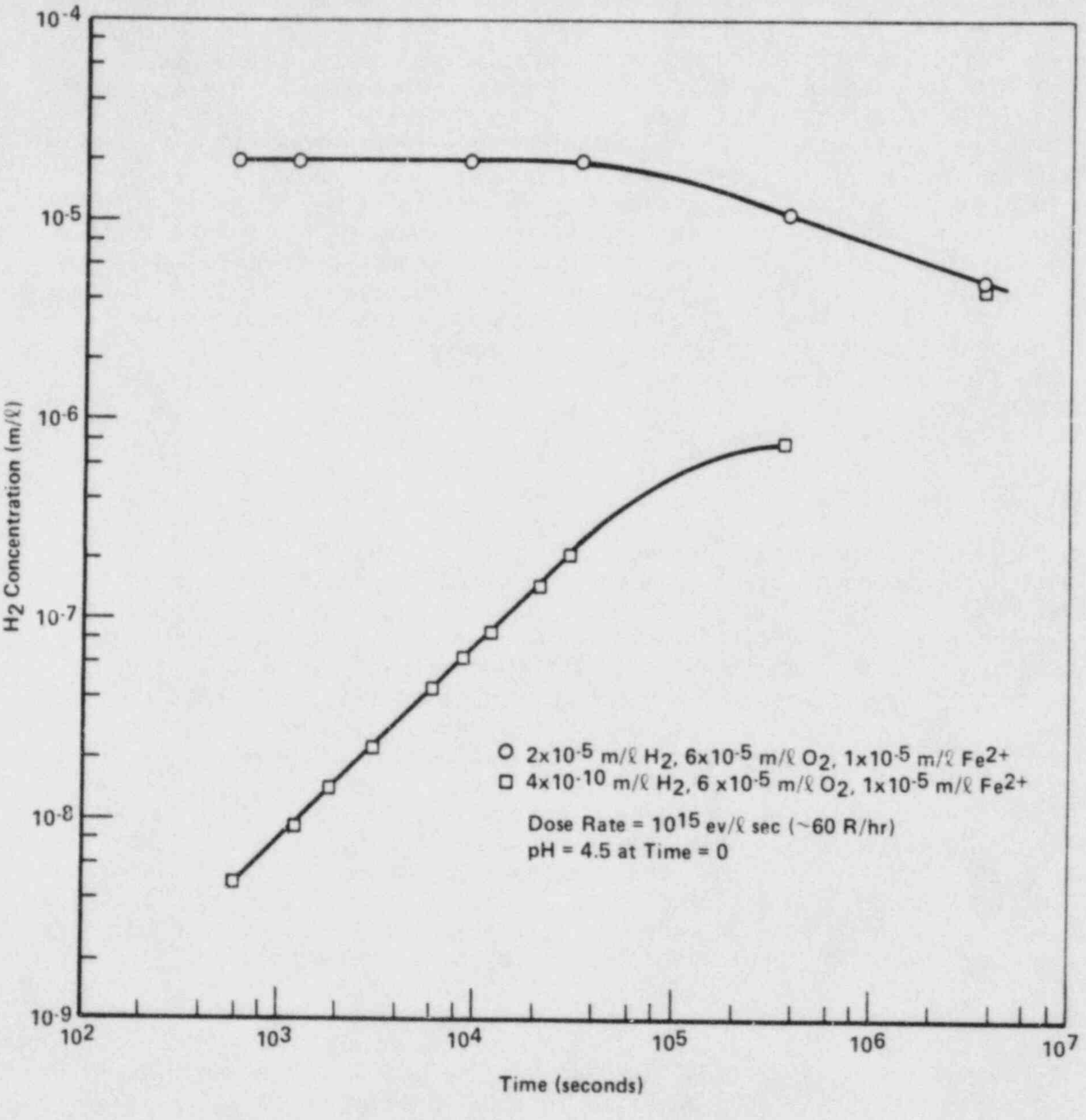

Figure 4.5. Effect of initial hydrogen concentration on the time-dependence of the dissolved-hydrogen concentration.

Table 4.2. Calculated concentrations of dissolved O_2, H_2O, H^+, and Fe^{2+} over time.

Time (sec)	O_2 mol/l	H_2O_2 mol/l	H^+ mol/l	Fe^{2+} mol/l	Initial Conditions of Solution
3.0E3	6.0E-5	1.2E-7	3.2E-5	9.4E-6	2 x 10^{-5} mole/liter H_2, 6 x 10^{-5} mole/liter O_2, 1 x 10^{-5} mole/liter Fe^{2+}, pH = 4.5
1.8E4	5.9E-5	2.7E-7	3.5E-5	5.4E-6	
3.6E5	4.6E-5	1.4E-5	5.1E-5	2.9E-9	
3.0E3	6.0E-5	9.4E-8	3.2E-5	9.5E-6	4 x 10^{-10} mole/liter H_2 6 x 10^{-5} mole/liter O_2 1 x 10^{-5} mole/liter Fe^{2+} pH = 4.5
1.8E4	5.9E-5	1.7E-7	3.4E-5	6.2E-6	
3.6E5	5.4E-5	6.5E-6	5.1E-5	3.0E-9	

Gamma Dose Rate = 10^{15} eV/l·sec (~ 60 R/hr).

4.3 Integral Experiments

The selection of combined effects to be targeted for detailed study is often based upon engineering judgment. When applying the knowledge from such studies to the formulation of a system description or to the assessment of licensing applications, there must be some basis for determining that important combined-effects processes have not been omitted. Thus there is a need to perform tests to provide investigators with a reasonably realistic view of the processes that may contribute to the degradation of waste packages. Such tests may help to confirm the importance of some processes which were believed to be important and may serve to identify others which were not considered previously. Results of these tests will aid in establishing a technical basis for identifying the level of detail necessary in a system model as well as in a licensing application.

The primary purpose of the integral experiments is to provide scoping information that will help to identify potentially important combined effects. Secondary purposes of these experiments are to provide qualitative information on corrosion phenomena, release rates, and water chemistry for spent-fuel and commercial high-level waste packages.

4.3.1 Design Features of the Experimental System

In a previous progress report$^{(4.25)}$ a basic diagram of the experimental system was outlined. This report describes in more detail several specifics of the system as well as some of the operating conditions. The items to be described are:

- Production and treatment of simulated groundwater
- Fluid transport and piping system
- Argon purge system for oxygen control
- Radiation field production
- Bentonite flow characteristics.

The central components of the experimental apparatus will be thirty Type 304 stainless steel test chambers inside an oven within a hot cell. The test cells are 3-inch (7.5-cm) outside-diameter, 3-inch-long (7.5-cm-long) sections of pipe with a stainless steel plate welded at one end. At the center of the welded plate is a 0.5-inch-long (1.3-cm-long) pipe fitting with 0.25-inch (0.6-cm) NPT heads, for connection to the solution input line. The 30 test cells will be welded to a support plate which, in addition to providing support, will be used to hold down the test-cell covers. The covers will consist of 0.38-inch-thick (1-cm-thick) stainless steel disks 4 inches (10 cm) in diameter. Several 0.25-inch (0.6-cm) bolts attached to the support plate will provide for holddown. The covers have grooves machined on one side which, together with a Type 321 stainless steel "O" ring, will provide for a leaktight seal. At the center of the cover plate is a second 0.5-inch-long (1.3-cm-long) pipe fitting for connection, via 0.25-inch (0.6-cm) NPT threads, to the solution exit line. The test cells will be oriented in the oven with the cylindrical symmetry axis directed vertically.

To prevent material in the test chambers (e.g., bentonite and corrosion products) from settling out the bottom of the cell, porous sintered stainless-steel disks will be placed near the cell bottom. The disks will prevent particles larger than ~ 3 μm from escaping through the bottom and will provide even flow of the simulated groundwater through the test cells.

In the hot cell, connections to and from the test cells will be made using 0.25-inch (0.6-cm) outer diameter, Type 316 stainless-steel tubing. Outside the hot cell, connections will be made with stainless-steel or plastic tubing.

The simulated groundwater will be made by adding appropriate amounts of dissolved solids to distilled water contained in 55-gallon, Type 304 stainless-steel reservoirs. The solutions will be thoroughly mixed and analyzed to ensure homogeneity and to verify composition. The simulated groundwater will be further conditioned by passing through a cartridge containing non-weathered basalt before reaching the test cells. Although we do not expect equilibrium to be established between the simulated groundwater and the basalt, some pickup of chemical species should occur, resulting in a more realistic groundwater solution. This is considered acceptable since the actual groundwater composition may vary with position in the repository.

The solutions will be pumped to the test cells using a 26-channel proportioning pump to control flow rate precisely. All piping to the pump will be stainless-steel tubing. At the pump, connections will be made to plastic tubing necessary for operation of the peristaltic pump. The only other plastic tubing in the system will be at the solution collection end after exit from the hot cell. The pump tubes, positioned under the pump rollers, will require replacement every 10 to 14 days.

To control the ingress of air to the system, the experimental apparatus will incorporate an argon-purge system to reduce the dissolved-oxygen level of the simulated groundwater. Oxygen present in the solution reservoirs will be removed by purging the prepared solutions with argon and then maintaining an argon blanket over the solution. A continuous slow flow of argon will be used for the duration of the experiment. The argon exiting the solution reservoirs will provide a cover over the plastic tubing of the proportioning pump and will prevent diffusion of air through the thin-walled pump tubing. Without the argon cover, the oxygen level could rise to a level above that found in the solutions contained in the reservoirs. Initially, the dissolved oxygen in the solutions will be monitored closely at several points along the system.

The radiation field of the test specimens will simulate the radiation field expected in the repository at the overpack surface. Once the irradiated fuel samples and actual waste-glass samples are prepared, they will be arranged in the test cells in a fashion which generates the most uniform field. Additional radiation sources are available if required to smooth out the field or to increase it.

As indicated in Section 4.3.2, eight of the test cells will contain Na-Montmorillonite (bentonite). One major concern in planning the integral experiments was that the bentonite in the test cells might form an impermeable plug, preventing solution flow. The plugging would, of course, limit the amount of useful information which could be gained from the test cells.

To investigate this possibility, a simple laboratory test was performed. A 1-inch-diameter (2.5-cm-diameter) glass column with a filter plug at the bottom was filled to a height of 4 inches (10 cm) with bentonite slurry. When the material had fully settled, an attempt was made to establish a flow though the bentonite bed. However, the bentonite bed moved up the glass column as a plug, and no flow was observed through the bed.

Because of the observed plugging, the experiment was modified by adding glass beads to the bentonite slurry to simulate packing material, then filling the glass column. In an actual test cell, basalt chips would be substituted for the glass beads. When the modified column was used for flow tests, the solution moved freely through the bed because the solution opened up channels around the beads. Therefore, in the actual integral experiments, the test cells containing bentonite will also contain basalt fragments to permit the flow of simulated groundwater.

4.3.2 Matrix of Experiments

The matrix of planned experiments is shown in Table 4.3. These experiments can be grouped into four categories: those involving high-level waste glass, those involving simulated high-level waste glass, those involving spent fuel, and corrosion tests. Each experiment shown in the matrix is performed in a separate test chamber. Experiments numbered 1 through 27 in the matrix will be performed in a basalt-type groundwater system. Because of the modular nature of the apparatus, these tests can readily be extended to include other experiments and other groundwater systems. The current design will allow for expansion to thirty individual test chambers in the oven. If necessary, additional test chambers, in other orientations or geometries, can be added.

Experiments 1 through 5 in the test matrix involve spent-fuel waste forms. Tests 1 through 4 involve spent fuel in failed cladding, and Test 5 involves pellet fragments. All spent-fuel samples will come from adjacent sections of a single characterized fuel rod. Specimens used in Tests 1, 3, and 4 will have a machined hole, and the specimen used in Test 2 will have a machined slit-failure opening. The failed spent-fuel specimens of Tests 1 and 2 will be surrounded by simulated corrosion products and packing material. Test 4 addresses the effect of flow rate on Test 3. Basalt chips will line the base of each chamber.

Table 4.3. Matrix of integral experiments.

	Container Material		Waste Form			State of Canister				Canister Environment				
Test Number	Stainless Steel	Cast Steel	HLW Glass	Simulated Glass	Spent Fuel	Perforated Container	Cracked Container	Failed Closure Weld	Uniformly Corroded Container	Steel Corrosion Products	Backfill	Basalt	Simulated Groundwater Flow Rate*	Notes
1					X					X	X	X	1	Slit
2					X					X	X	X	1	Perforation
3					X								1	Perforation
4					X								2	Perforation
5					X								1	Pellet Fragments
6			X			Intact Canister							1	
7			X			X							1	
8			X			X							2	
9			X				X						1	
10			X					X					1	
11			X						X				1	
12			X			X				X	X	X	1	
13			X										1	
14			X										2	
15				X		Intact Canister				X	X	X	1	
16				X		X				X	X	X	1	
17				X		X				X	X	X	2	
18				X			X			X	X	X	1	
19				X				X		X	X	X	1	
20				X					X	X	X	X	1	
21				X		X					X	X	1	
22				X		X							1	
23				Blank (Empty Test Chamber)									1	
24		X												"Prepitted Sample"
25		X												SCC U Bend
26	X													SCC U Bend
27	X	X (welded)												Galvanic Corrosion
28														Tests to be determined
29														
30														

*Flow rate 1 = 5 cm^3/hr; Flow rate 2 = 50 cm^3/hr.

Tests 6 through 14 use high-level waste glass. Test 6 is a "blank", in which the waste form is enclosed in a simulated intact canister. Tests 7 through 11 address effects of canister-breach openings on the release of radionuclides. The breach openings will include perforations, cracks, and fluid volume such as may result from failure of a closure weld, and corrosion products remaining from uniform corrosion of the canister. To encourage the release of radionuclides from the test chamber, samples in Tests 6 through 11 will not be surrounded by packing, basalt, or simulated corrosion products. Test 12 addresses the effect of these materials on a simulated perforation failure. Tests 13 and 14 each use bare high-level waste glass in the test chambers. The fluid-flow rate in Test 14 is ten times that of Test 13.

Tests 15 through 22 use simulated high-level waste glass. Results of these tests will be applied to the combined-effects and water-chemistry studies. These tests are similar to Tests 6 through 14, except that most samples are surrounded by other materials such as packing.

Test 23 is an empty test chamber which will be used as a "blank". Simulated basalt-type groundwater will flow through this test chamber, and some analyses, such as measurements of pH and oxygen concentration, will be performed.

Test chambers 24 through 27 will include corrosion-test specimens which will complement the out-of-cell corrosion experiments. Test 24 will examine pit propagation in cast steel in a radiation field under simulated repository-type conditions. Tests 25 and 26 examine stress-corrosion cracking of cast and stainless steels, respectively, in a radiation field under simulated repository-type conditions, and Test 27 addresses galvanic corrosion under these conditions.

4.3.3 Procurement and Assembly of the Apparatus

All major components of the experimental system have been ordered. Table 4.4 lists the ordered components and their delivery status. The test cells are being fabricated. Several secondary items have been ordered and received, including such items as plastic tubing, sample receivers, and solution-storage containers.

4.3.4 Future Work

In the near term, the apparatus for the integral experiments will be constructed. Concurrently, we will assemble the materials to be placed in the apparatus, including the basalt, packing, waste forms, and corrosion specimens. The spent-fuel samples will be sectioned, capped, and "prefailed" during this time period.

Table 4.4. Procurement status of components needed for the integral experiments.

Apparatus	Manufacturer	Status
Autoanalyzer Proportioning Pump	Technicon	Ordered (overdue)
Oven for Test Cells	Lab-Line Instruments	Ordered (overdue)
Stainless Steel Tubing	Kilsby-Roberts	Delivered
Stainless Steel Reservoirs	Hoffman Container	Delivered
Tubing Connectors and Fittings	Swagelok	Ordered
Porous Stainless Steel Disks	Pall	Ordered
Dissolved Oxygen Meter	YSI	Ordered
PNL Waste Glass	PNL	Delivered
Spent Fuel	--	On Hand
Test Cells	--	Under Construction
Na-Montmorillonite	University of Missouri-Columbia	Delivered
Metal "O" Rings	Fluorocarbon	Ordered

4.4 References for Section 4

(4.1) "Long-Term Performance of Materials Used for High-Level Waste Packaging", D. Stahl and N. E. Miller (Compilers), NUREG/CR-3405, Vol. 1 (July 1983).

(4.2) A. H. Truesdell and B. F. Jones, "WATEQ, A Computer Program for Calculating Chemical Equilibria of Natural Waters", U.S. Geol. Surv. J. Res 2, 223, 1974.

(4.3) "Long Term Performance of Materials Used for High-Level Waste Packaging", D. Stahl and N. E. Miller (Compilers), NUREG/CR-3427, Vol. 1 (August 1983).

(4.4) "Long-Term Performance of Materials Used for High-Level Waste Packaging," D. Stahl and N. E. Miller (Compilers), NUREG/CR-3427, Vol. 4 (June 1984), Section 4.

(4.5) E.L.J. Rosinger and R. S. Dixon, "Mathematical Modeling of Water Radiolysis: A Discussion of Various Methods", AECL-5958 (1977).

(4.6) "Long-Term Performance of Materials Used for High-Level Waste Packaging", D. Stahl and N. E. Miller (Compilers), NUREG/CR-3427, Vol 2 (December 1983).

(4.7) "Long-Term Performance of Materials Used for High-Level Waste Packaging", D. Stahl and N. E. Miller (Compilers), NUREG/CR-3427, Vol. 3 (March 1984).

(4.8) "Long-Term Performance of Materials Used for High-Level Waste Packaging," D. Stahl and N. E. Miller (Compilers), NUREG/CR-3900, Vol 1 (September 1984).

(4.9) R. W. Mathews, "The Radiation Chemistry of Aqueous Ferrous Sulfate Solutions at Natural pH," Aust. J. Chem 36 1305-17 (1983).

(4.10) Z. Stuglik and Z. P. Zagorski, "Pulse Radiolysis of Neutral Iron (II) Solutions: Oxidation of Ferrous Ions by OH Radicals," Radiat. Phys. Chem. 17 (4) 229-33 (1981).

(4.11) H. Christensen and E. Bjergbakke, "Radiolysis of Groundwater from HLW Stored in Copper Canisters", SKBF-KBS-TR-82-02 (1982).

(4.12) R. N. Sylva, "The Hydrolysis of Iron III", Rev. Pure and Appl. Chem. 22 115-32 (1972).

(4.13) J. Dousma and P. L. de Bruyn, "Hydrolysis Precipitation Studies of Iron Solutions I. Model for Hydrolysis and Precipitation from Fe(III) Nitrate Solutions," J. Colloid and Interface Science 56 (3) 527-39 (1976).

(4.14) J. Dousma and P. L. de Bruyn, "Hydrolysis-Precipitation Studies of Iron Solutions II. Aging Studies and the Model for Precipitation from Fe(III) Nitrate Solutions," J. Colloid and Interface Science 64 (1) 154-70 (1978).

(4.15) R. J. Knight and R. N. Sylva, "Precipitation in Hydrolyzed Iron (III) Solutions," J. Inorg. Nucl. Chem. 36 591-7 (1974).

(4.16) J.H.A. Van Der Woude and P. L. De Bruyn, "Formation of Colloidal Dispersions from Supersaturated Iron (III) Solutions. I. Precipitation of Amorphous Iron Hydroxide," Colloids and Surfaces 855-78 (1983).

(4.17) J.H.A. Van Der Woude, P. Verhees, and P. L. De Bruyn, "Formation of Colloidal Dispersions from Supersaturated Iron (III) Nitrate Solutions. II. Kinetics of Growth at Elevated Temperatures," Colloids and Surfaces, 8 79-92 (1983).

(4.18) G. Biedermann and P. Schindler, "On the Solubility Product of Precipitated Iron (III) Hydroxide," Acta Chem. Scand. 11 731-40 (1957).

(4.19) A. R. Olson and T. R. Simonson, "The Hydrolysis of Ferric Ion," J. Chem. Phys. 17 (1949) 1322-25.

(4.20) M. J. Smith et al., "Engineered Barrier Development for a Nuclear Waste Repository Located in Basalt: An Integration of Current Knowledge," RHO-BWI-ST-7 (May 1980).

(4.21) "Review of Waste Package Verification Tests," P. Soo (ed.), NUREG/CR-3091 Vol. 3 (February 1984).

(4.22) N. A. Lange and G. M. Forker, Langes Handbook of Chemistry, McGraw-Hill Book Co. (1967).

(4.23) R. C. Weast, Handbook of Chemistry and Physics, Chemical Rubber Publishing Co. (1974).

(4.24) Nuclear Safety Analysis Center, "Analysis of Three Mile Island-Unit 2 Accident," NSAC-80-1 (Revised March 1980).

(4.25) "Long-Term Performance of Materials Used for High-Level Waste Packaging", D. Stahl and N. E. Miller (Compilers), NUREG/CR-3900, Vol. 1 (September 1984), pp. 4-25 ff.

5. QUALITY ASSURANCE

Quality assurance surveillance of the various program activities continues. No procedures were prepared or revised during this quarter. As of this date there are 34 approved QA procedures and two approved work instructions for the program.

A summary of the procedures which are being used to conduct the experimental program is given in Table 5.1. Included is the procedure number, the current revision number, the title, and the status.

Quality assurance surveillance activities will continue. Procedures will be revised and new ones prepared as necessary to meet program requirements.

Table 5.1. Status of NRC waste packaging program QA procedures.

Procedure No.	Title	Status
WF-PP-1 Revision 0	Procedures for Record Keeping and Documentation for NRC Waste Form System Model Development	Approved
WF-PP-5 Revision 0	Procedures for Record Keeping and Documentation for Separate Effects Model Development	Approved
WF-PP-10 Revision 0	Laboratory Procedure for Preparation of Glasses for NRC Waste Form Project	Approved
WF-PP-11 Revision 1	Laboratory Procedures for Preparation of Teflon-Leach Containers	Approved
WF-PP-14 Revision 1	Laboratory Procedure for Leaching Glass Samples	Approved
WF-PP-16 Revision 0	Laboratory Procedure for Operating the Orton Dilatometer	Approved
WF-PP-20 Revision 0	Procedure for Determining the Corrosion Rates of Alloys at High Temperatures	Approved
WF-PP-25 Revision 0	Procedure for Preparation of Carbon-Steel Casting	Approved
WF-PP-26 Revision 0	Procedure for Preparation of Steel Hydrogen-Embrittlement Test Specimens	Approved
WF-PP-26.1 Revision 0	Procedure for Preparation of Hydrogen-Embrittlement Test Specimens from Steel or Iron Samples	Approved

Table 5.1. Continued.

Procedure No.	Title	Status
WF-PP-27 Revision 4	Procedure for J-Testing Compact Tension Specimens	Approved
WF-PP-28 Revision 1	Procedure for Performing Tension Tests of Steel Specimens	Approved
WF-PP-29 Revision 0	Procedure for Conducting Hydrogen-Absorption Experiments	Approved
WF-PP-30 Revision 0	Laboratory Procedure for Preparation, Cleaning, and Evaluation of Titanium Grade-12 Specimens for Corrosion Studies of the Overpack Performance for the NRC Waste Packaging Program	Approved
WF-PP-31 Revision 0	Laboratory Procedure for Preparation, Cleaning, and Evaluation of Cast and Wrought Carbon Steel Specimens for Corrosion Studies of the Overpack Performance for the NRC Waste Packaging Program	Approved
WF-PP-32 Revision 0	Procedure for Preparation of Brine A for Corrosion Testing Under Simulated Repository Conditions	Approved
WF-PP-33 Revision 0	Procedure for Preparation of Simulated Basalt Groundwater Solution	Approved
WF-PP-33.1 Revision 0	Procedure for Preparation of Basalt Rock for Use in Corrosion Studies for the NRC Waste Packaging Program	Approved
WF-PP-34 Revision 0	Procedure for Preparation of Simulated Tuff Groundwater Solutions	To be Written

Table 5.1. Continued.

Procedure No.	Title	Status
WF-PP-35 Revision 1	Procedure for Performing Autoclave Exposures for Corrosion Tests in Simulated Brines	Approved
WF-PP-35.1 Revision 0	Procedure for Performing Autoclave Exposures for Corrosion Tests in Simulated Brines Using Sealed Internal Canister	Approved
WF-PP-36 Revision 0	Procedure for Performing Stagnant Autoclave Exposures for Corrosion Tests in Simulated Basalt or Tuff Groundwaters	Approved
WF-PP-37 Revision 0	Laboratory Procedure for Preparing Polarization Resistance Specimens, Performing Polarization Resistance Measurements and Evaluating Polarization Resistance Data	Approved
WF-PP-37.1 Revision 0	Laboratory Procedure for Performing Eh and Corrosion Potential Measurements in Autoclave Exposures in Simulated Basalt and Tuff Groundwater	Approved
WF-PP-37.2 Revision 0	Laboratory Procedure for Determination of the Polarization Behavior of Metal Specimens at Ambient Pressure	Approved
WF-PP-38 Revision 0	Procedure for Preparing and Evaluation of U-Bend Specimens for Stress Corrosion Studies of Overpack Materials for the NRC Waste Packaging Project	Approved
WF-PP-38.1 Revision 0	Procedure for Performing and Evaluating 3 Point Bend Beam Specimens for Stress Corrosion Studies of Overpack Materials for NRC Waste Package Program	Approved

Table 5.1. Continued.

Procedure No.	Title	Status
WF-PP-39 Revision 0	Procedure for Preparing, Testing and Evaluating Crevice Corrosion Specimens of Titanium Grade-12 and Cast Steel	Approved
WF-PP-40 Revision 0	Laboratory Procedures for Preparation, Cleaning, and Evaluation of Thermogalvanic and Heat-Transfer Specimens	Approved
WF-PP-41 Revision 0	Laboratory Procedures for Determination of Corrosion Rates Under Heat-Transfer Conditions	Approved
WF-PP-42 Revision 0	Laboratory Procedure for Determination of Thermogalvanic Corrosion Rates	Approved
WF-PP-43 Revision 0	Procedure for Welding Titanium Grade-12 Plate for Use in Corrosion Studies of Overpack Materials for NRC Waste Isolation Project	Approved
WF-PP-44 Revision 0	Procedure for Welding Cast and Wrought Steel Specimens	To be Written
WF-PP-45 Revision 0	Laboratory Procedure for Preparing and Evaluating Slow Strain-Rate Specimens and for Performing Slow Strain-Rate Tests	Approved
WF-PP-45.1 Revision 0	Laboratory Procedures for Performing Slow Strain-Rate Tests Under Potentiostated Conditions	Approved
WF-PP-46 Revision 0	Procedure for Preparation of Titanium Grade-12 Corrosion Specimens with Metallic Iron Embedded in the Surface	Approved

DISTRIBUTION LIST

Office of Regulatory Research
Division of Radiation Programs and Earth Sciences
Mail Stop 1130 SS
U.S. Nuclear Regulatory Commission, Washington, D.C. 20555

Attn: Division Director/Deputy Director
E. F. Conti, Chief, Waste Management Branch
F. A. Costanzi
J. R. Randall
M. B. McNeil
K. S. Kim, Project Manager (15)

Division of Waste Management, NMSS
Mail Stop 623 SS
U.S. Nuclear Regulatory Commission, Washington, D.C. 20555

Attn: Division Director/Deupty Director
Chief, Engineering Branch
E. A. Wick
M. Tokar
K. C. Chang
Document Control Center

Advisory Committee on Reactor Safeguards
Mail Stop H-1016
U.S. Nuclear Regulatory Commission, Washington, D.C. 20555

Attn: Waste Management Subcommittee
R. C. Tang

Battelle's Columbus Laboratories
505 King Avenue
Columbus, Ohio 43201-2693

Attn: D. Stahl, Program Manager (50)

DISTRIBUTION LIST (Continued)

Martin A. Molecke
Sandia National Lab.
Albuquerque, NM 87185

Neville Pugh
National Bureau of Standards
Washington, D.C. 20234

Nicholas Grant
Department of Metallurgy
Massachusetts Institute
of Technology
Cambridge, MA 02139

Jerome Kruger
Corrosion Section
National Bureau of Standards
Washington, D.C. 20234

Tae-Moon Ann
Brookhaven National Lab.
Upton, NY 11973

Don J. Bradley
Waste Package Programs
Battelle Pacific Northwest Labs
Richland, WA 99352

Allen G. Goff
Oak Ridge National Laboratory
P.O. Box X
Oak Ridge, TN 37830

Lynn Hobbs
Department of Materials Science
Massachusetts Institute of
Technology
77 Massachusetts Avenue
Cambridge, MA 02139

Richard E. Westerman
Pacific Northwest Lab.
P.O. Box 999
Richland, WA 99352

Thomas D. Chikalla
Pacific Northwest Lab.
P.O. Box 999
Richland, WA 99352

John Crandall
Savannah River Lab.
Aiken, SC 29808

Edward J. Hennelly
Savannah River Lab.
Aiken, SC 29808

Arthur A. Bauer
Office of Nuclear Waste Isolation
Battelle Memorial Institute
505 King Avenue
Columbus, OH 43201

Michael Smith
Basalt Waste Isolation Projects
Rockwell Hanford Operation
Richland, WA 99352

Kenneth Russell
Department of Materials Science
and Engineering
Massachusetts Institute of
Technology
Cambridge, MA 02139

Robert H. Doremus
Materials Engineering Department
Rensselaer Polytechnic Institute
Troy, NY 12181

David C. Kocher
Oak Ridge National Lab.
P.O. Box X
Oak Ridge, TN 37830

Stanley Wolf
DOE/BES
Washington, D.C. 20585

Neville Moody
Sandia Livermore Lab.
Livermore, CA 94550

Donald E. Clark
ONWI
Battelle Memorial Institute
505 King Avenue
Columbus, OH 43201

DISTRIBUTION LIST (Continued)

Martin Seitz
Argonne National Lab.
Argonne, IL 60439

Martin J. Steindler
Argonne National Lab.
Argonne, IL 60439

Donald G. Schweitzer
Brookhaven National Lab.
Upton, NY 11973

Peter Soo
Brookhaven National Lab.
Upton, NY 11973

David Martin
Iowa State University
Ames, IA 50011

Harold Wollenberg
Lawrence Berkeley Lab.
Berkeley, CA 94720

Nestor Ortiz
Sandia National Lab.
Albuquerque, NM 87185

Pedro B. Macedo
Catholic University of America
Washington, D.C. 20064

Robert Williams
Electric Power Research Institute
P.O. Box 10412
Palo Alto, CA 94301

William P. Reed
U.S. Department of Commerce
National Bureau of Standards
Washington, D.C. 20234

Ray Walton
U.S. Department of Energy
Washington, D.C. 20545

John E. Mendel
Materials Characterization Center
Pacific Northwest Lab.
Richland, WA 99352

Larry Hench
University of Florida
Gainesville, FL 32611

Davis E. Clark
University of Florida
Gainesville, FL 32611

Joseph Mascara
MS 5650 NL
U.S. Nuclear Reg. Comm.
Washington, DC 20555

Ken W. Stephens
The Aerospace Corp., Suite 400
955 L'Enfant Plaza, S.W.
Washington, DC 20024

Robert S. Dyer
Office of Radiation Programs (ANR-461)
U.S. Environmental Protection Agency
401 M Street, S.W.
Washington, DC 20460

Lorenzo Ricks
Office of Energy Research
U.S. Department of Energy
Washington, D.C. 20545

Larry Evans
Armco Research Center
703 Curtis Avenue
Middletown, OH 45043

Woody Swope
Armco Stainless Steel Division
P.O. Box 1697
Baltimore, MD 21203

M. John Plodinec
Savannah River Laboratory
Aiken, SC 29808

Dennis R. Floyd
Manufacturing Sciences Corp.
711 Walnut Street
Boulder, CO 80302

NRC FORM 335
(11-81)

U.S. NUCLEAR REGULATORY COMMISSION

BIBLIOGRAPHIC DATA SHEET

1. REPORT NUMBER *(Assigned by DDC)*
NUREG/CR-3900, Vol. 2

4. TITLE AND SUBTITLE *(Add Volume No., if appropriate)*
Long-Term Performance of Materials Used for High-Level Waste Packaging: Quarterly Report, July-September 1984

2. *(Leave blank)*

3. RECIPIENT'S ACCESSION NO.

7. AUTHOR(S)
Compiled by D. Stahl and N. E. Miller

5. DATE REPORT COMPLETED
MONTH: November
YEAR: 1984

9. PERFORMING ORGANIZATION NAME AND MAILING ADDRESS *(Include Zip Code)*
Battelle's Columbus Laboratories
505 King Avenue
Columbus, Ohio 43201-2693

DATE REPORT ISSUED
MONTH: January
YEAR: 1985

6. *(Leave blank)*

8. *(Leave blank)*

12. SPONSORING ORGANIZATION NAME AND MAILING ADDRESS *(Include Zip Code)*
Division of Radiation Programs and Earth Sciences
Office of Nuclear Regulatory Research
U.S. Nuclear Regulatory Commission
Washington, D.C. 20555

10. PROJECT/TASK/WORK UNIT NO.

11. FIN NO.
B6764

13. TYPE OF REPORT
Quarterly

PERIOD COVERED *(Inclusive dates)*
July-September 1984

15. SUPPLEMENTARY NOTES

14. *(Leave blank)*

16. ABSTRACT *(200 words or less)*

During this reporting period, it was found that glass-water contact during the non-isothermal periods of leach testing may influence the test results. Modeling of waste-form degradation focused on dissolution/reprecipitation kinetics. An experiment is planned to verify this model. A procedure was developed to disperse RuO_2 in MCC 76-68 glass. Potentiodynamic polarization tests were performed to determine the effects of single chemical species in groundwater on the cracking and pitting susceptibility of carbon steel. Slow strain rate tests show that carbon steel is especially susceptible to stress-corrosion cracking in aqueous $FeCl_3$ at low strain rates. The strength of commercial high-purity iron was found not to be affected by hydrogen; however, ductility was somewhat reduced. The description of groundwater radiolysis was further refined during this quarter. Integral experiments are being prepared to provide information on combined-effects processes that may influence the long-term performance of the waste package.

17. KEY WORDS AND DOCUMENT ANALYSIS
High-level waste
Waste package
Waste form/container/overpack

17a. DESCRIPTORS

17b. IDENTIFIERS/OPEN-ENDED TERMS

18. AVAILABILITY STATEMENT
Unlimited

19. SECURITY CLASS *(This report)*
Unclassified

20. SECURITY CLASS *(This page)*
Unclassified

21. NO. OF PAGES

22. PRICE
$

UNITED STATES
NUCLEAR REGULATORY COMMISSION
WASHINGTON, D.C. 20555

OFFICIAL BUSINESS
PENALTY FOR PRIVATE USE, $300

FOURTH CLASS MAIL
POSTAGE & FEES PAID
USNRC
WASH. D.C.
PERMIT No. G-67

120555078877 1 IAN1CH
US NRC
ADM-DIV OF TIDC
POLICY & PUB MGT BR-PDR NUREG
W-501
WASHINGTON DC 20555